

Research

A Strain-based Clad Failure Criterion for Reactivity Initiated Accidents in Light Water Reactors

Lars Olof Jernkvist
Ali R. Massih
Peter Rudling

August 2004

SKI Perspective

Background and purpose of the project

Over the last 10 years the behaviour of nuclear fuel during reactivity initiated accidents has been studied to investigate the failure threshold as a function of burnup. Experimental programmes performed in the CABRI test reactor (France) and in the Nuclear Safety Research Reactor (Japan) have indicated that cladding failure and fuel dispersion of high burnup fuel may occur at enthalpy values lower than previously estimated.

At the beginning of 1995 SKI issued fuel and cladding failure limits based on available test data. It was envisaged at that time that the failure limits should be re-evaluated when more information was available. Since then SKI has joined the OECD-IRSN CABRI water loop project at the end of 2000. The purpose was to gain information on the failure threshold for nuclear fuel cladding as a function of burnup, especially for modern cladding materials and during prototypical conditions.

In 2003 SKI initiated a study, in cooperation with the Swedish nuclear utilities, to recommend more relevant fuel failure limits for reactivity initiated accidents.

The work presented in this report is the first part of the study. In the report a strain-based failure criterion is formulated based on mechanical tests and compared with experimental tests and other failure criterion. The second part, which consists of failure thresholds calculated by use of best-estimate computational methods, is reported in SKI report 2004:33. The third part is a sensitivity study which is reported in SKI report 2004:34.

Results

This project has contributed to the research goal of giving a basis for SKI's supervision by means of evaluating and modelling the nuclear fuel cladding failure threshold during a design base accident. The project has also contributed to the research goal to develop the competence about licensing of fuel at high burnup, which is an important safety issue.

Project information

Responsible for the project at SKI has been Jan in de Betou.
SKI Reference: 14.06-011070/02149

Research

A Strain-based Clad Failure Criterion for Reactivity Initiated Accidents in Light Water Reactors

Lars Olof Jernkvist¹

Ali R. Massih¹

Peter Rudling²

¹Quantum Technologies AB

Uppsala Science Park

SE-751 83 Uppsala

Sweden

²ANT International

Ekbacken 33

SE-735 35 Surahammar

Sweden

Augusti 2004

This report concerns a study which has been conducted for the Swedish Nuclear Power Inspectorate (SKI). The conclusions and viewpoints presented in the report are those of the author/authors and do not necessarily coincide with those of the SKI.

List of contents

Summary	III
Sammanfattning	IV
1 Introduction	1
2 Reactivity initiated accidents	3
2.1 Postulated scenarios	3
2.1.1 Control rod ejection accidents	3
2.1.2 Control rod drop accidents	3
2.2 Consequences	4
2.3 Acceptance criteria	5
3 PCMI-induced fuel rod failure under RIA	7
3.1 Failure mechanism	7
3.1.1 Radial crack propagation	7
3.1.2 Axial crack propagation	8
3.2 Influence of fuel rod design on failure propensity	9
3.2.1 Clad tube design	9
3.2.2 Fuel pellet design	9
3.2.3 Pellet-clad gap	11
3.3 Influence of operating conditions on failure propensity	12
3.3.1 Steady-state and transient coolant conditions	12
3.3.2 Steady-state and transient fuel rod power	13
3.4 Influence of clad tube conditions on failure propensity	15
3.4.1 Irradiation damage	15
3.4.2 Direct effects of clad oxide layer	16
3.4.3 Effects of oxygen	17
3.4.4 Effects of hydrogen	17
3.5 Influence of fuel pellet conditions on failure propensity	23
3.5.1 Radial distribution of power	23
3.5.2 Rim zone microstructure	25
3.5.3 Transient fission gas release	28
3.5.4 Pellet-clad contact and bonding	29
4 Experimental database	31
4.1 Pulse reactor tests	31
4.1.1 Overview of pulse reactor tests	31
4.1.2 Typicality of test reactor conditions	33
4.1.3 SPERT-CDC tests	34
4.1.4 PBF tests	35
4.1.5 NSRR tests	35
4.1.6 CABRI REP-Na tests	37
4.2 Mechanical property tests	38
4.2.1 Introduction	38
4.2.2 Zircaloy-2 material	40
4.2.3 Zircaloy-4 material	41

5	Clad failure criterion	43
5.1	Bases for the clad failure criterion	43
5.2	Evaluation of mechanical property tests	44
5.2.1	Adaptation of ductility test data	44
5.2.2	Exploration and interpretation of test data	49
5.3	Proposed clad failure criterion	53
5.3.1	Effect of elevated strain rate	55
5.3.2	Effect of hydrogen	55
5.3.3	Effect of irradiation	57
5.4	Uncertainties of the clad failure criterion	60
5.4.1	Direct comparison with mechanical property tests	60
5.4.2	Sensitivity study	65
6	Discussion	69
6.1	Application of the failure criterion to CABRI tests	69
6.2	Comparison with SED-based failure criteria	71
6.3	Effect of spalled oxide layer	76
6.4	Range of application and limitations	80
7	Conclusions	83
8	Nomenclature	85
9	References	87
	Appendix A: Pulse reactor test data	97
A.1	SPERT-CDC tests	97
A.2	PBF tests	98
A.3	NSRR tests	99
A.3.1	Tests on PWR fuel rods	99
A.3.2	Tests on BWR fuel rods	102
A.3.3	Tests on JMTR fuel rods	104
A.4	CABRI REP-Na tests	106
	Appendix B: Mechanical property test data	109
B.1	Zircaloy-2 clad material	109
B.1.1	NFD tests	109
B.1.2	Dataset A	109
B.1.3	Studsvik tests	109
B.2	Zircaloy-4 clad material	111
B.2.1	Dataset B	111
B.2.2	JAERI tests	111
B.2.3	Tests on Fort Calhoun (FC) clad tubes	112
B.2.4	Tests on ANO-2 and CC-1 clad tubes	114
	Appendix C: Clad failure criteria based on strain energy density	117
C.1	Converting CSED to hoop failure strain	118
C.2	CSED correlations	120
C.2.1	CSED correlation by EPRI/ANATECH	120
C.2.2	CSED correlation by CSN/CIEMAT	121
C.3	MATPRO constitutive relation	121

Summary

This report deals with failure of high-burnup fuel rods under reactivity initiated accidents (RIAs) in light water reactors. In particular, a strain-based criterion for clad tube failure under such accidents is formulated. The criterion is intended for prediction of clad tube failures caused by pellet-clad mechanical interaction during the early heat-up phase of RIAs, and it is applicable to RIA scenarios in both boiling- and pressurized water reactors.

We first delineate the mechanisms responsible for fuel rod failure under RIAs, based on an evaluation of RIA simulation tests performed to date on pre-irradiated fuel rods in pulse reactors. We also discuss how these mechanisms are affected by fuel rod design, operating conditions and burnup-related changes in the state of both cladding and fuel pellets, such as e.g. hydride-induced clad embrittlement and pellet rim zone restructuring.

The ability of the clad tube to expand radially by plastic deformation is found to be crucial for fuel rod survival under RIAs, and consequently, we propose a failure criterion based on clad critical hoop plastic strain. From an experimental database of more than 200 out-of-pile mechanical property tests, comprising cladding from fuel rods irradiated up to $68 \text{ MWd}(\text{kgU})^{-1}$ as well as un-irradiated hydrogen-charged samples, we formulate a correlation for clad hoop plastic strain at failure with respect to clad temperature, irradiation damage, strain rate and hydrogen content. Clad tube failure is assumed to take place when the clad hoop plastic strain exceeds the ductility limit defined by this correlation.

The proposed failure criterion is assessed in several ways. Firstly, calculated failure strains from the correlation are directly compared with clad ductility data from mechanical property tests, thereby allowing uncertainties of the failure criterion to be identified and quantified. Secondly, the proposed failure criterion is compared with two other criteria, reported in literature, which are based on critical strain energy density. The comparison shows that the considered criteria differ significantly, presumably as a result of differences in the supporting databases. Finally, the proposed failure criterion is applied in simulations of five pulse reactor tests within the CABRI REP-Na program. The simulations are made with the SCANAIR computer code, into which the failure criterion is implemented. Reasonable clad failure strains are calculated for all simulated tests, although failure/no-failure is properly predicted for only two of the five tests.

Based on the performed assessments, we conclude that the proposed failure criterion is suitable for prediction of clad tube failure for a wide spectrum of reactivity initiated accidents with a fair level of accuracy. In particular, the range of application covers reactivity initiated accidents at both cold zero power conditions in boiling water reactors and hot zero power conditions in pressurized water reactors.

Sammanfattning

Denna rapport behandlar skador hos högutbrända kärnbränslestavar under reaktivitetsolyckor (RIA) i lättvattenreaktorer. Särskilt avseende fästs vid formuleringen av ett töjningsbaserat kriterium för prediktering av kapslingsrörsskador under dessa olyckor. Kriteriet är avsett för prediktering av kapslingsrörsskador orsakade av mekanisk växelverkan mellan bränslekuts och kapsling vid uppvärmningsförloppet under reaktivitetsolyckans tidiga fas, och det är tillämpligt för reaktivitetsolyckor i såväl kok- som tryckvattenreaktorer.

Med utgångspunkt från en utvärdering av hittills genomförda pulsreaktorförsök på bestrålade bränslestavar, inleder vi rapporten med att beskriva de mekanismer som leder till bränsleskador under reaktivitetsolyckor. Vi diskuterar även hur dessa mekanismer påverkas av bränslestavens konstruktion, driftförhållanden samt olika utbränningsrelaterade förändringar hos kapslingsrör och bränslekutsar, såsom till exempel väteförsprödning av kapslingen och mikrostrukturförändringar av kutsens rand (rim zone).

Kapslingsrörets förmåga att utvidgas radiellt genom plastisk deformation är central för undvikande av bränsleskador under reaktivitetsolyckor, och vi föreslår därför ett skadekriterium baserat på kritisk plastisk ringtöjning för kapslingsröret. Från en experimentell databas med mer än 200 laboratoriebestämningar av mekaniska egenskaper, omfattande kapslingsmaterial från bränslestavar med utbränning upp till $68 \text{ MWd}(\text{kgU})^{-1}$ såväl som obestrålat laborariehydrerat material, utarbetar vi en korrelation mellan kapslingens plastiska brottöjning och materialets temperatur, neutrondos, töjningshastighet och vätehalt. Kapslingsrörsskador antas uppstå då kapslingens plastiska ringtöjning överstiger den kritiska töjningsgräns som definieras av den härledda korrelationen.

Det föreslagna skadekriteriet analyseras på flera sätt. Inledningsvis jämförs brottöjningar, beräknade med den härledda korrelationen, med motsvarande data från mekanisk provning. Därigenom kan osäkerheter hos skadekriteriet identifieras och kvantifieras. Därefter jämförs det föreslagna skadekriteriet med två i litteraturen beskrivna kriterier, vilka är baserade på kritisk töjningsenergitäthet. Jämförelsen påvisar avsevärda skillnader mellan de tre kriterierna, vilket troligen beror på att de är baserade på skilda experimentella data. Slutligen används det föreslagna skadekriteriet vid simulering av fem pulsreaktorförsök, utförda inom programmet CABRI REP-Na. Simuleringarna görs med datorprogrammet SCANAIR, i vilket skadekriteriet införts. Rimliga brottöjningar beräknas för kapslingsrören i samtliga simulerade experiment, men kapslingsskada predikteras korrekt i endast två av de fem fallen.

Med stöd av de genomförda analyserna drar vi slutsatsen att det föreslagna skadekriteriet är lämpat för att med rimlig noggrannhet prediktera kapslingsrörsskador under reaktivitetsolyckor av vitt skilda slag. Särskilt bör här påpekas att kriteriet är tillämpligt för analys av reaktivitetsolyckor vid effekt nära noll, såväl för kokvattenreaktorer i kallt tillstånd som för tryckvattenreaktorer i varmt tillstånd.

1 Introduction

Reactivity initiated accidents (RIAs) are important design basis events in light water reactors (LWRs). The rapid change in local fuel power under RIA may result in fuel rod failure. In its mildest form, fuel failure merely entails loss of clad tube integrity and escape of radioactive fission products to the primary coolant, but in more severe cases, the rapid energy deposition may cause fragmentation of both fuel and cladding, loss of coolable geometry of fuel assemblies, and subsequent core damage.

During the last decade, RIA simulation tests performed in pulse reactors have shown that failure is more likely to occur in high-burnup fuel rods than in fresh fuel, mainly because of the combined effects of pellet-clad mechanical interaction and clad embrittlement. This finding raises concern about the adequacy of current acceptance criteria and fuel operating limits for RIA. These criteria were established in the late seventies and early eighties, based on early pulse reactor tests made on fuel rods with zero or low burnup, and therefore, they do not consider the increased susceptibility to fuel rod failure at high burnup.

From a regulatory viewpoint, failure of high-burnup fuel under RIAs is therefore currently a matter of concern, and new burnup-dependent operating limits are being proposed worldwide. Most of the proposed limits are based on direct rendition of experimental failure/no-failure data from pulse reactor tests on high-burnup fuel rods. However, these tests are performed at conditions that are far from prototypical of light water reactors, and analytical tools are therefore generally needed in order to correctly transform the results from pulse reactor tests to LWR conditions.

The work presented in this report is the first step in a project, which is aimed at establishing a fuel failure threshold for RIAs in high-burnup light water reactor fuel. A clad failure criterion for irradiated, oxidized and hydrided clad tubes is formulated, based on evaluations of out-of-pile mechanical property tests. In the following step of the project, this failure criterion is applied in simulations of realistic reactivity insertion events, postulated to occur in light water reactors, using analytical tools in the form of a comprehensive computer code package (In de Betou et al., 2004).

The organization of the report is as follows:

Section 2 provides a short background to reactivity initiated accidents in light water reactors. The most critical postulated scenarios for RIAs in boiling- and pressurized water reactors, as well as their possible consequences to fuel rod integrity, are briefly described, and the background to currently applied acceptance criteria and fuel operating limits is reviewed.

Section 3 deals with the mechanisms responsible for clad tube failure under RIA in high-burnup fuel, and we discuss in detail how these mechanisms are affected by fuel rod design, operating conditions and the burnup-dependent changes in the state of both cladding and fuel pellets. The discussion is based on results and findings from pulse reactor tests on high-burnup fuel rods and out-of-pile mechanical property tests on highly irradiated and hydrided clad tubes. These experiments are summarized in section 4, and results from relevant pulse reactor tests and clad mechanical property tests are compiled in appendix A and B of the report, respectively.

The clad tube failure criterion is derived in section 5. The criterion is based on more than 200 out-of pile mechanical property tests, performed on highly irradiated cladding and un-irradiated hydrogen-charged samples. By exploring this database, we derive a correlation for clad hoop plastic strain at failure with respect to temperature, irradiation damage, strain rate and clad hydrogen content. The derived correlation forms the basis for a strain-based failure criterion. To this end, by comparing calculated failure strains from the correlation with experimental data, we also identify and quantify uncertainties in the proposed failure criterion.

In section 6, the failure criterion is applied in analyses of five RIA simulation tests in the CABRI pulse reactor. The purpose is to demonstrate the applicability of the criterion to in-reactor transients, and also to test the criterion in combination with the SCANAIR computer code, which will be extensively used in the second step of the project. Moreover, the proposed strain-based failure criterion is compared with two failure criteria based on critical strain energy density, which are taken from open literature. The differences between the criteria are evaluated and discussed. Finally, section 6 concludes with a discussion on the range of application and main limitations of the proposed failure criterion.

2 Reactivity initiated accidents

The reactivity initiated accident belongs to the group of design basis accidents in light water reactors. Hence, it is a postulated event of very low probability, which would have serious consequences if it were not inherently accounted for in the design of the reactor and related safety systems.

The reactivity initiated accident involves inadvertent removal of a control element from an operating reactor, thereby causing a rapid power excursion in the nearby fuel elements. If the reactivity worth of the ejected element is high, the rapid energy deposition in adjacent fuel elements may be sufficient to cause fuel rod failure. However, the ejection of a control element results in most cases only in a moderate increase in reactivity. The postulated scenarios for reactivity initiated accidents are therefore focused on a few events, which result in exceptionally large reactivity excursions, and therefore are critical to fuel integrity. These scenarios are briefly described in section 2.1 below.

In section 2.2, we shortly summarize the consequences of RIA with respect to fuel rod integrity and thermo-mechanical behaviour. Acceptance criteria with respect to fuel integrity under RIA are discussed in section 2.3.

2.1 Postulated scenarios

2.1.1 Control rod ejection accidents

In a pressurized water reactor (PWR), the RIA scenario of primary concern is the control rod ejection accident (REA). The REA is caused by mechanical failure of a control rod mechanism housing, such that the coolant pressure ejects a control rod assembly completely out of the core (Glasstone & Sesonske, 1991). The ejection and corresponding addition of reactivity to the core occurs within about 0.1 s in the worst possible scenario. The actual time depends on reactor coolant pressure and the severity of the mechanical failure.

With respect to reactivity addition, the most severe REA would occur at hot zero power (HZIP) conditions, i.e. at normal coolant temperature and pressure, but with nearly zero reactor power (Agee et al., 1995) and (Nakajima et al., 2002).

2.1.2 Control rod drop accidents

In a boiling water reactor (BWR), the most severe RIA scenario is the control rod drop accident (CRDA). The initiating event for the CRDA is the separation of a control rod blade from its drive mechanism (Glasstone & Sesonske, 1991). The separation takes place when the blade is fully inserted in the core, and the detached blade remains stuck in this position until it suddenly becomes loose and drops out of the core in a free fall.

Hence, the control rod is removed from the core due to gravity, and in contrast to the REA in PWRs, coolant pressure does not influence the rod ejection rate.

With respect to reactivity addition, the most severe CRDA would occur at cold zero power (CZP) conditions, i.e. at a state with the coolant close to room temperature and atmospheric pressure, and the reactor at nearly zero power (Agee et al., 1995) and (Nakajima et al., 2002). The degree of reactivity addition during CRDA is strongly affected by the coolant subcooling, since vapour generation effectively limits the power transient.

2.2 Consequences

If the reactivity addition under a REA or CRDA is sufficient, the reactor becomes prompt critical and power will rise rapidly until the negative fuel temperature feedback (Doppler effect) terminates the power rise within a few hundredths of a second. Under a CRDA, additional negative feedback is obtained from void generation in the coolant. After the power surge is terminated, the power is finally reduced to zero by insertion of fault-free control rods due to reactor trip.

In the considered RIA scenarios, the fuel assemblies near to the ejected control element are thus subjected to a fast and short power pulse. The shape and duration of the power pulse depend on the assumed scenario, core and fuel design, and the burnup dependent state of the fuel. Analyses of postulated RIA scenarios with state-of-the-art three-dimensional neutron kinetics codes indicate that the width of the power pulse is in the range from 30 to 75 ms in fuel with burnup exceeding $40 \text{ MWdkg}^{-1}\text{U}^{-1}$, (Meyer et al., 1997) and (In de Betou et al., 2004). The pulse width is related to the pulse amplitude, and it has been shown to vary inversely with the increase in fuel enthalpy under the transient (Diamond et al., 2002).

The rapid increase in power leads to nearly adiabatic heating of the fuel pellets, which expand thermally and may cause fast straining of the surrounding clad tube through pellet-clad mechanical interaction (PCMI). At this early heat-up stage of the RIA, the clad tube material is still at a fairly low temperature ($<650 \text{ K}$), and the fast straining imposed by the expanding fuel pellets may therefore cause a rapid and partially brittle mode of clad failure (Chung & Kassner, 1998).

At a later stage of the transient, heat transferred from the pellets may bring the clad outer surface to such a high temperature that dry-out or departure from nucleate boiling (DNB) occurs. If so, the clad material could remain at a temperature above 1000-1200 K for up to 10 s, until rewetting takes place (Fuketa et al., 2001). This fairly long period at elevated temperature may lead to clad creep rupture, in cases where significant pressure differences exist across the clad wall. The clad rupture could either be in the form of outward ballooning or inward collapse, depending on whether the rod internal gas pressure exceeds the coolant pressure or *vice versa* (Ishijima & Nakamura, 1996).

In addition, a third mode of failure may occur during re-wetting of the overheated clad tube, since the abrupt quenching may cause brittle fracture and disruption of the clad material. This failure mode is imminent if the clad tube is severely oxidized.

Of the three different failure modes described above, PCMI-induced clad failures during the early heat-up stage of an RIA are presumably the most restricting for high-burnup fuel rods, whereas the high-temperature post-DNB or post-dryout failures are limiting for fresh and low-burnup fuel. In this report, we restrict our attention to PCMI-induced clad failures under the early heat-up stage of the transient.

Provided that the clad tube fails, fragmented fuel may disperse into the coolant. This expulsion of hot fuel material into water has potential to cause rapid steam generation and pressure pulses, which could damage nearby fuel assemblies and possibly also the reactor pressure vessel and internal components. Hence, the potential consequences of fuel dispersal are of primary concern with respect to core and plant safety.

2.3 Acceptance criteria

Acceptance criteria for fuel behaviour under RIA were established by the United States Nuclear Regulatory Commission (US NRC) in the late seventies, based on results from early RIA simulation tests in pulse reactors (MacDonald, et al., 1980). These criteria, the details of which are given in (RG-1.77, 1974) and (NUREG-0800, 1981), have been used worldwide in their original or slightly modified forms, and they are therefore summarized here.

Firstly, a core coolability limit is defined, stating that the radial average fuel enthalpy may not exceed 280 cal/gUO₂ (1172 J/gUO₂) at any axial location in any fuel rod. This limit is intended to ensure core coolability and reactor pressure vessel integrity by precluding violent expulsion of fuel particles into the coolant.

Secondly, a fuel rod failure threshold is defined, stating that clad failure should be assumed in rods that experience radially averaged fuel enthalpies above 170 cal/gUO₂ (712 J/gUO₂). This failure threshold is used in evaluations of radiological consequences of escaped fission products from failed rods, and it is not a definite operating limit. Hence, fuel enthalpies above this threshold are allowed in some of the fuel rods. The failure threshold is applicable to RIA events initiated from zero or low power, i.e. in practice to BWR RIA at CZP conditions. For rated power conditions, fuel rods that experience dry-out (BWR) or departure from nucleate boiling (PWR) should be assumed to fail.

The above defined enthalpy limits are actually erroneous: As noted by MacDonald et al. (1980), the US NRC mistakenly expressed the limits in terms of radial average peak fuel enthalpy, whereas the supporting experimental data were reported in terms of radial average total energy deposition. The radial average peak fuel enthalpy is less than the associated radial average total energy deposition, due to fuel-to-coolant heat transfer under the power transient, and also since a large fraction of the total energy is due to delayed fission. If this mistake is corrected, the core coolability limit is reduced to 230 cal/gUO₂ (963 J/gUO₂) and the fuel rod failure threshold is 140 cal/gUO₂ (586 J/gUO₂).

These acceptance criteria are based on early pulse reactor tests on fuel rods with zero or very low burnup, and the fuel enthalpy limits are therefore burnup-independent. As will be shown in section 4.1, more recent pulse reactor tests on high-burnup fuel rods have resulted in fuel dispersal and clad failure at enthalpies well below 230 and 140 cal/gUO₂, respectively. Acceptance criteria for RIA in high-burnup fuel are therefore currently a matter of concern, and new burnup-dependent operating limits are being proposed worldwide. Recently, Yang et al. (2003) proposed operating limits based on an evaluation methodology that combined experimental data with analytical calculations, but other proposed limits are usually based on direct rendition of experimental data from pulse reactor tests, see e.g. the work by Waeckel et al. (2000), Nam et al. (2001) and Vitanza (2002).

The currently applied operating limits for RIA in Sweden also belong to this empirical class, and the burnup-dependent core coolability limit and clad failure threshold, established by the Swedish Nuclear Power Inspectorate in 1995, are shown in figure 2.1 (SKI, 1995). At fuel burnups up to 33 MWd/kgUO₂, these limits coincide with the corrected burnup-independent limits defined by US NRC, i.e. 963 J/gUO₂ and 586 J/gUO₂, respectively.

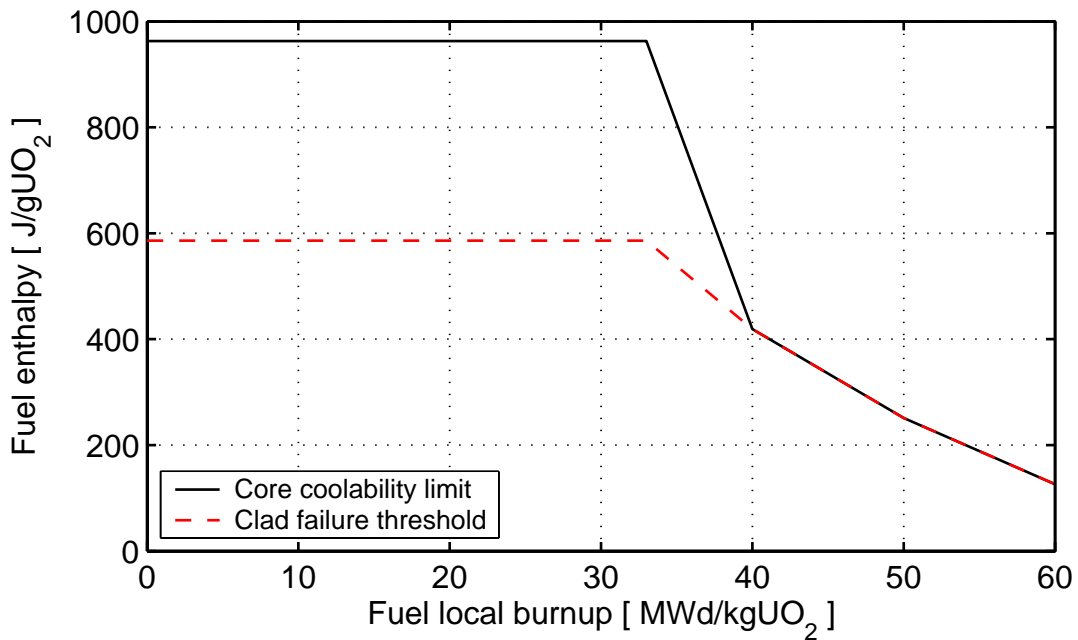


Figure 2.1: Currently applied operating limits for RIA in Sweden. The fuel enthalpy limits are defined as axial peak, radial average values.

3 PCMI-induced fuel rod failure under RIA

This section deals with the mechanisms behind PCMI-induced clad tube failure under RIA in high-burnup fuel. Moreover, we discuss how the clad failure mechanisms are affected by fuel rod design, operating conditions and burnup-dependent changes to the state of both cladding and fuel pellets.

3.1 Failure mechanism

As discussed in section 2.2, there are three possible modes of clad tube failure under reactivity initiated accidents in light water reactors. Henceforth, we restrict our attention to failures under the early heat-up phase of an RIA, which is believed to be the limiting failure mode for high-burnup fuel rods. These failures are generally assumed to take place through a two-stage process, where the first stage involves propagation of clad external flaws into through-wall defects with limited axial extension. In the second stage, these through-wall defects grow into long axial cracks (Chung & Kassner, 1998).

3.1.1 Radial crack propagation

Under pulse reactor tests on high-burnup fuel rods with corroded cladding, it is generally observed that numerous radial cracks nucleate in the clad outer oxide layer. Under the hoop tensile stresses induced by PCMI, these radial cracks form easily in the brittle oxide, presumably immediately upon plastic deformation of the underlying clad material. Some of these incipient oxide cracks also propagate through the oxygen- and hydrogen-rich material just beneath the oxide. This subjacent material is also brittle, at least at low temperature, and the radial crack path through the oxide layer and the outer part of the clad wall therefore appears characteristically brittle in fractographic examinations of high-burnup fuel rods, which have failed in RIA simulation tests, see e.g. the work by Fuketa et al. (2000) or Nakamura et al. (2002a).

However, the radial crack path through the innermost part of the clad wall generally indicates ductile failure, with the fracture surface typically inclined 45° to the main loading (hoop) direction. The ductile feature of the last part of the crack path is usually seen also in highly corroded and embrittled cladding, and it is believed that this inner ductile part of the clad wall offers significantly higher resistance to the radial crack propagation than the brittle outer part. A typical crack path, observed in the clad tube after a pulse reactor RIA test of a high-burnup PWR fuel rod, is shown in figure 3.1.

The transition from brittle fracture in the outer part to ductile failure in the inner part of the clad wall is governed by the radial gradient in both hydrogen concentration and temperature across the clad wall; see section 3.4.4 for further details on this matter. It seems that the gradient in hydrogen concentration is more important than that in temperature, since the same characteristic brittle/ductile fracture paths are observed in material property tests on hydrided cladding at isothermal conditions as in pulse reactor tests with sharp temperature gradients (Yagnik et al. 2004).

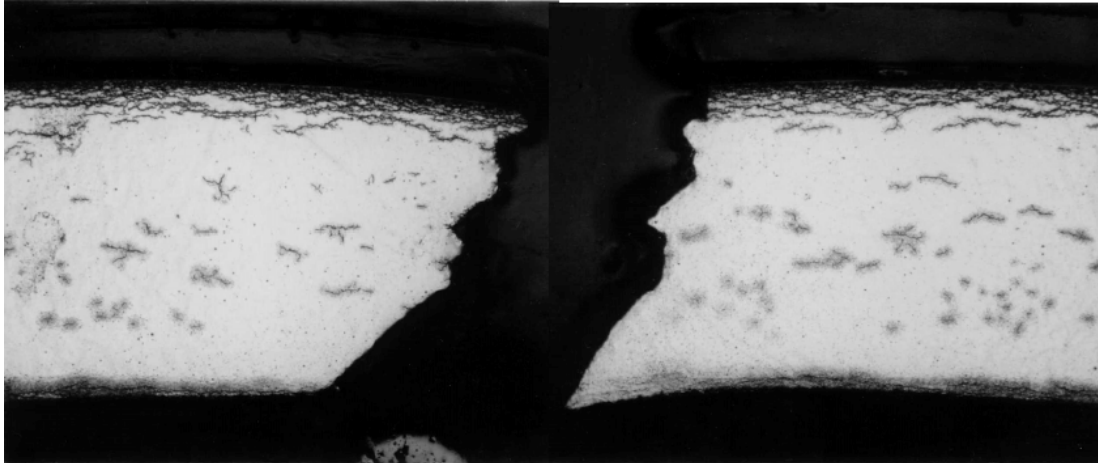


Figure 3.1: Typical radial crack path in oxidized and hydrided cladding, subjected to RIA simulation test in the Nuclear Safety Research Reactor (NSRR), Japan. The crack path is brittle through the outer part of the clad wall, but ductile through the inner part. Photograph of rod TK-7 from Fuketa et al. (2000).

3.1.2 Axial crack propagation

Of the numerous incipient radial cracks usually observed in the clad outer oxide layer, only a few develop into through-wall defects. These primary clad defects are believed to have limited axial extension, although it is difficult to draw definite conclusions on this matter for full-length LWR fuel rods. As described in section 4.1, our understanding of RIA fuel rod failures is based on pulse reactor tests on short-length rodlets, whose failure behaviour may be different from that of full-length rods. However, axial propagation of the short primary defects into longer axial cracks is usually considered to be a separate, second stage in the clad failure mechanism (Chung & Kassner, 1998).

There is some dispute whether the primary defects grow axially through a fast and unstable propagation mechanism (Chung, 2000), or if the propagation takes place during cool-down of the clad, *after* the actual transient. The latter hypothesis is supported by a delay in fission gas expulsion from failed rods, which has been observed in RIA simulation tests in the CABRI facility (Waeckel et al., 2000). Further tests on specially instrumented fuel rods are probably needed in order to resolve this issue.

The mechanism responsible for long axial cladding cracks under RIA is of primary importance with regard to fuel safety concerns about fuel dispersal into the coolant. However, in the work presented here, we actually consider only the first stage of the clad failure mechanism i.e. the radial growth of the primary defect, and ignore the details of axial crack growth. See section 5.1 for further motivation to this restriction.

3.2 Influence of fuel rod design on failure propensity

The fuel rod behaviour under RIA is influenced by the rod design, operating conditions and also by burnup-related changes in the state of both fuel pellets and cladding. For fuel rods exceeding $30\text{-}35 \text{ MWdkg}^{-1}\text{U}^{-1}$ in burnup, it is difficult to distinguish the effects of differences in design parameters from effects caused by high burnup. Consequently, pulse reactor tests aimed at studying the influence of various fuel rod design parameters on failure propensity and thermo-mechanical behaviour under RIA have predominantly been performed on fresh fuel. The most comprehensive work of this kind is by Ishikawa and Shiozawa (1980), who made a systematic study on the influence of various design parameters on the failure threshold of fresh PWR fuel rods, subjected to RIA simulation tests in the NSRR.

Significant differences in the response to pulse reactor tests are generally observed between BWR and PWR fuel rods, (Fuketa et al., 2000) and (Nakamura et al., 2002b). These differences result to some extent from differences in design between BWR and PWR fuel, but mainly from disparate operating conditions. This is further discussed in section 3.3.

3.2.1 Clad tube design

The clad wall thickness, alloy composition and heat treatment under manufacturing are design parameters of importance to the clad tube behaviour under RIA. The clad alloy composition and heat treatment have significance mainly to the corrosion rate and hydrogen pickup of the material, and consequently, to the clad embrittlement and strength reduction with increasing burnup. These effects are discussed in section 3.4.

Recent post-irradiation examinations of high-burnup zirconium liner BWR cladding, which had undergone RIA simulation tests in NSRR, indicate that the liner may affect the clad failure behaviour (Nakamura et al, 2002a). Hydrides were observed not only at the clad outside surface, but also within the liner material at the clad inner surface. Moreover, the crack path through the liner appeared to be caused by brittle fracture. Hence, it seems that the liner barrier is more sensitive to hydride-induced embrittlement than the Zircaloy-2 base material. If so, liner cladding of high-burnup fuel rods may suffer from double-sided hydride-induced embrittlement.

3.2.2 Fuel pellet design

The enrichment of ^{235}U affects the fuel reactivity, which determines the transient power pulse experienced by the fuel under an RIA. A high enrichment of ^{235}U increases the energy deposition in the fuel pellets. Moreover, the enrichment also affects the radial distribution of power and thereby the radial temperature profile in the fuel pellets. The temperature profile, in turn, affects the pellet deformation behaviour and fission gas release. The enrichment of ^{235}U in commercial LWR fuel is typically in the range 2.5 – 5.0 %, and the fuel rod behaviour under RIA is not significantly affected by variations in fuel enrichment within this narrow range.

However, as shown in section 4.1, many RIA simulation tests have been performed on fuel enriched to 10 and even 20 %, and one should not expect the behaviour of this fuel to be representative of commercial LWR fuel with significantly lower enrichment. This is particularly true for high-burnup fuel, in which the shape of the radial power profile is strongly affected by the initial ^{235}U enrichment. This is illustrated in figure 3.2, which shows the radial power profiles at a pellet radial average burnup of $60 \text{ MWdkg}^{-1}\text{U}^{-1}$ for two fuel pellets with different initial enrichments. The profiles are calculated with the TUBRNP model by Lassmann et al. (1994). As shown in section 3.5.1, the radial temperature profile in the pellet agrees very closely to the power profile during the initial heat-up phase of an RIA.

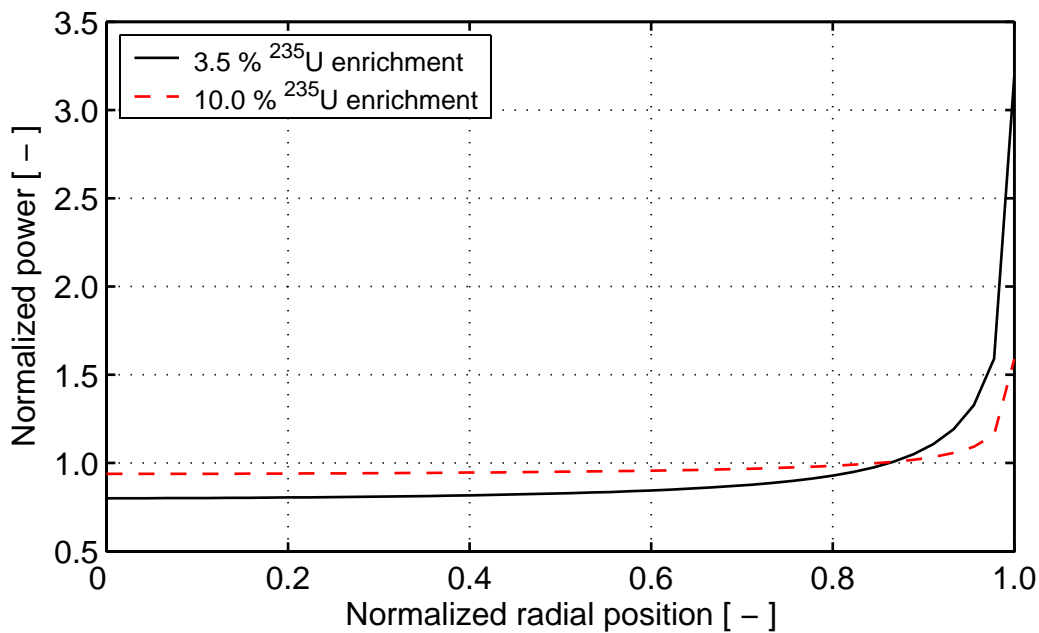


Figure 3.2: Influence of initial ^{235}U enrichment on radial power distribution in high-burnup fuel pellets. The fuel pellet radius is 4.5 mm and the radial average burnup is $60 \text{ MWdkg}^{-1}\text{U}^{-1}$ in both cases shown.

From ramp tests on fuel rods with various fuel pellet geometries, it is known that the ratio between pellet length and diameter has impact on pellet-clad mechanical interaction (Cox, 1990). Under normal operating conditions, the non-uniform thermal expansion leads an hourglass shape to the originally cylindrical pellets, which causes cladding stress concentrations at pellet-pellet interfaces. These stress concentrations are mitigated by chamfering the pellets and reducing their length to diameter ratio.

As shown in section 3.5.1, the radial temperature profile in high-burnup fuel under the initial phase of an RIA is strongly peaked to the pellet periphery, i.e. opposite to the profile under normal operation, and the deformed shape of a fuel pellet, expected from thermal expansion alone, is that of a barrel. However, the gas-induced fuel swelling from growth of pressurized pores and fission product gas bubbles may add to the thermal expansion under RIA, and modify this barrel shape in an unknown manner.

Pulse reactor tests on high-burnup 17×17 PWR fuel rods with two different pellet geometries have been conducted within the TK and HBO test series at the NSSR facility (Fuketa et al., 2001). Differences in terms of pellet deformation mode and fission gas release between the two fuel designs were observed, but these differences could not be attributed to the disparate pellet geometries alone, since also the pellet fabrication process was different for the two fuel designs.

Fuel additives in the form of Al₂O₃ and SiO₂, which are known to improve pellet ductility and thereby reduce PCMI-induced clad stresses under normal fuel operation, have proven ineffective under RIA (Yanagisawa et al., 1990). This is hardly surprising, since the beneficial effect of these additives is due to enhanced UO₂ fuel creep rate, whereas the time scale of a typical RIA is much too short for creep relaxation to take place in the material.

Finally, a comment should be made on the differences in RIA behaviour between UO₂ and mixed oxide (MOX) fuel. The fissile material in MOX fuel is mostly plutonium, and the fuel pellets are usually produced by mixing plutonium oxide powder into natural (non-enriched) uranium oxide powder, followed by pelletizing and sintering. The standard process used creates a heterogeneous material, with plutonium oxide (PuO₂) agglomerates embedded in a matrix of natural UO₂. Since fissions occur predominantly in the agglomerates, they reach very high local burnup, although the volume average burnup is moderate. At high burnup, the heterogeneous distributions of power and burnup in MOX fuel lead to significantly higher fission gas release and fission gas induced swelling than for UO₂ fuel under comparable RIA transients (Fuketa et al., 2000) and Sasajima et al. (2000). For this reason, high-burnup MOX fuel rods are more susceptible to failure under RIA than UO₂ fuel rods. For fresh fuel, on the other hand, the aforementioned differences between MOX and UO₂ fuel are insignificant with respect to RIA, and a series of RIA simulation tests on fresh PWR fuel rods with MOX fuel pellets, reported by Abe et al. (1992), did not reveal any difference between fresh MOX and UO₂ fuel in regard to fuel rod failure threshold enthalpy.

3.2.3 Pellet-clad gap

The pellet-clad contact state at onset of an RIA is important, since it determines how much of the fuel pellet transient expansion can be accommodated in the gap, and how much must be accommodated by cladding outward deformation. The impact of initial gap state on clad deformation is clearly seen in comparisons between BWR and PWR fuel rods, which have been subjected to RIA simulation tests in the NSRR (Fuketa et al., 2000). For identical burnup levels and RIA conditions, the PWR fuel rods show much larger clad plastic deformations than the BWR rods. The difference is due to fast creep-down of the PWR cladding, which results in early gap closure and significant pellet-clad contact prior to the RIA. This is further discussed in section 3.3.1.

Consequently, the initial pellet-clad gap size and the rod initial fill gas pressure are fuel rod design parameters with impact on pellet-clad mechanical interaction, since they affect the time to gap closure.

3.3 Influence of operating conditions on failure propensity

As already touched upon in the preceding section, the propensity for clad tube failure is influenced by the fuel operating conditions. Coolant conditions and fuel power, under the RIA transient as well as under the pre-transient steady-state operation, affect the fuel rod behaviour under RIA.

3.3.1 Steady-state and transient coolant conditions

The coolant pressure and temperature under normal steady-state operation are much different in PWRs and BWRs. The high coolant pressure and temperature in PWRs lead to fast creep-down of the cladding, and closure of the pellet-clad gap therefore occurs much earlier in life for PWR- than for BWR fuel. As a result, the PWR fuel experiences stronger pellet-clad mechanical interaction under RIA, in comparison with BWR fuel at similar burnup. In addition, the high coolant temperature aggravates clad corrosion, which means that also the potential for degradation of clad strength and ductility by oxidation and hydrogen pickup is larger in PWRs than in BWRs. However, this is compensated for by using more corrosion resistant clad materials in PWRs. In contrast to BWRs, the coolant temperature in PWRs is not uniform, but rises with axial elevation in the core. The loss of clad strength and ductility due to clad corrosion is therefore more pronounced in the upper part of PWR fuel rods (Fuketa et al., 1997).

From the aforementioned differences in steady-state coolant conditions between boiling- and pressurized water reactors, one might suspect that for identical burnup levels, PWR fuel would be more susceptible to failure under RIA than BWR fuel. However, to make a relevant comparison, one must consider the differences in coolant conditions not only under steady-state operation, but also under the RIA.

In the most limiting RIA scenario for BWRs, i.e. a CRDA at CZP, the transient initiates from room temperature. As shown in section 5.2.2.4, oxidized and hydrided clad material, typical for high-burnup fuel, is very brittle at room temperature. In RIA scenarios for PWRs, the transient initiates from temperatures around 570 K. At these temperatures, also severely oxidized and hydrided cladding is fairly ductile.

Hence, the initial coolant temperature at onset of RIA is more beneficial for clad ductility in PWRs, and this must be accounted for, when comparing the susceptibility of boiling- and pressurized water reactor fuel to clad tube failure. To this end, it should be noticed that a direct comparison of PWR and BWR fuel rods, tested in the NSSR facility, is misleading: all tests performed on pre-irradiated fuel rods in the NSRR are performed at coolant conditions that correspond to BWR CZP RIA (Fuketa et al., 2000).

3.3.2 Steady-state and transient fuel rod power

The steady-state power history prior to RIA is important, since it influences the initial fuel rod conditions at onset of the transient. As an example, the pre-transient power level affects the fission gas release from the fuel pellets, which in turn influences both pellet-clad heat transfer and the pellet gas-induced swelling under RIA. Moreover, as further discussed in section 3.5.3, pulse reactor tests in the NSRR show that the transient fission gas release under RIA is correlated to the pre-transient power level and gas release under steady-state operation. These tests clearly reveal that high pre-transient fission gas release leads to high gas release also under the transient (Fuketa et al., 2000).

The pre-transient power history also influences the clad corrosion behaviour, especially in PWRs, since the corrosion rate is affected by coolant temperature and clad-to-coolant heat flux (Garzarolli & Holzer, 1992). The pre-transient power history is also believed to affect the precipitation of radially oriented hydrides, which are particularly detrimental to the clad tube ductility; see section 3.4.4.4. Tensile hoop stresses in the cladding, induced by pellet-clad mechanical interaction under high-power or load-follow operation of high-burnup fuel, are reported to promote precipitation of radially oriented hydrides (Chung & Kassner, 1998).

The transient power history under RIA, i.e. the power pulse imposed on the fuel, is generally characterized by two parameters: pulse width and total energy deposition. The pulse width is usually defined as the full width at half maximum (FWHM), whereas the total energy deposition is the time integral of fuel power, evaluated from beginning to end of the transient. Obviously, these two parameters alone cannot provide a full picture of a realistic power pulse.

With respect to PCMI-induced clad failure in high-burnup fuel under RIA, an important feature of the power pulse is the rate of power increase during the early part of the transient. Since the fuel is heated almost adiabatically during the early part of an RIA, the rate of power increase directly controls the rate of fuel pellet thermal expansion. The thermal expansion rate has a strong impact on local stresses at the fuel pellet periphery, and consequently, on fuel pellet fragmentation (Lespiaux et al., 1997) and rapid burst release of intergranular fission gas (Lemoine, 1997). In case the pellet-clad gap is closed, the fuel pellet thermal expansion is directly transferred to the cladding, and the rate of power increase thus also controls the clad strain rate. As shown in section 5.2.2.2, the clad ductility is affected by strain rate. Moreover, the rate of power increase controls the time lag between mechanical loading and heating of the clad tube. A fast power increase results in high PCMI-induced clad stresses at a time when the cladding has not yet been heated from its initial temperature. Since the ductility of oxidized and hydrided cladding is low at low temperature, fast power pulses are prone to cause clad failure. For slow power pulses, the clad temperature evolves in tandem with the mechanical loads, and the risk for brittle clad failure in the early part of the transient is therefore smaller. This is illustrated in figure 3.3, which shows the calculated clad average temperature, plotted with respect to clad hoop strain, for two simulated pulse reactor tests in the CABRI REP-Na program; see section 4.1.6. In the first test, Na-1, the width (FWHM) of the power pulse was 9.5 ms, whereas in the second test, Na-4, it was 75 ms.

The initial clad temperature was 553 K in both tests, and the total energy depositions in the two tests were similar; see section A.4 in appendix A for details. The calculations were done with the SCANAIR computer code (Federici et al., 2000) and (Papin et al., 1997). The temperatures and strains presented in figure 3.3 pertain to the peak power axial positions of the two rods.

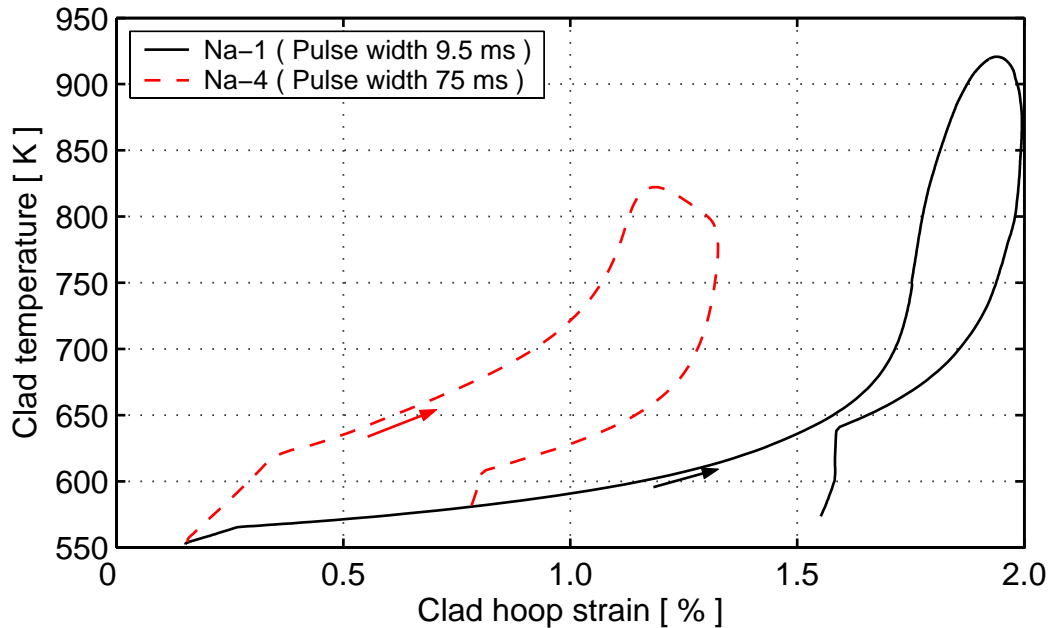


Figure 3.3: Calculated evolution of clad temperature and deformation in CABRI REP Na-1 and Na-4. Calculated temperatures and strains are radial average values, pertaining to the peak power axial positions of the two rods.

Clearly, in the fast power pulse test Na-1, most part of the cladding deformation takes place at temperatures below 600 K. On the other hand, in the Na-4 test, most of the clad deformation occurs at temperatures above 650 K, i.e. in a temperature range where the clad material is comparatively ductile.

Finally, it should be noticed that the effect of pulse width illustrated in figure 3.3 is even more important if the transient starts from room temperature, such as in an RIA at BWR CZP conditions. This follows from the effect of temperature on clad ductility, which is more pronounced at room temperature than at 550-600 K; see section 5.2.2.4.

3.4 Influence of clad tube conditions on failure propensity

In section 3.2, we discussed the influence of certain clad design parameters, such as alloy composition and heat treatment, on the propensity for fuel rod failure under RIA. However, the progressive change in clad tube material properties during irradiation is by far more important than differences in design parameters. The clad tube material properties change during in-reactor operation, primarily by accumulation of irradiation damage in the material, and by metal-water reactions. Both phenomena lead to clad embrittlement, i.e. to loss of ductility and fracture toughness.

The irradiation damage reaches saturation early in life, usually within the first years of fuel operation. Deterioration of the clad material through metal-water reactions, on the other hand, progresses continuously with increasing burnup. Effects of metal-water reactions are therefore more interesting than irradiation damage, when studying the propensity for RIA failures of high burnup fuel rods.

Although the external oxide layer in itself influences both the thermal and mechanical properties of high burnup fuel, the mechanical properties are primarily affected by the migration of dissolved hydrogen, produced by the metal-water reactions, into the material beneath the oxide layer. Hydrogen is known to have a detrimental effect on clad strength and ductility, since it precipitates as zirconium hydrides (Northwood & Kosasih, 1983).

3.4.1 Irradiation damage

Irradiation damage in zirconium alloy clad tubes is caused by fast (energetic) neutrons, which cause microstructural damage to the material through knockout and recoil processes. The damage is in the form of point defects, small dislocations loops, short line dislocations and dislocation entanglements. These defects reduce the ductility of zirconium alloys by hindering dislocation movements, which is the mechanism responsible for plastic deformation in metals. In irradiated cladding, plastic deformation does not take place uniformly in the material, but the dislocation movements are confined to small regions. This localization phenomenon is known as dislocation channelling (Garde et al., 1996).

Irradiation-induced loss of ductility is observable at fairly low neutron fluences: for material irradiated at 600 K, typically at 10^{24} m^{-2} ($E \geq 1 \text{ MeV}$), and the embrittlement generally saturates already under the first cycle of fuel operation. In the absence of other embrittling phenomena, such as hydride precipitation, zirconium alloys seem to have a ductility minimum at a fast neutron fluence of about $2 \times 10^{25} \text{ m}^{-2}$, corresponding to a rod burnup of about $10 \text{ MWdkg}^{-1}\text{U}^{-1}$ (Garde et al., 1996). Further loss of clad ductility beyond this neutron fluence is thus due to embrittling phenomena other than pure irradiation damage.

If the material is held at elevated temperature, the microstructural defects responsible for irradiation embrittlement are annealed, and some of the ductility thus recovered.

The annealing is a time-dependent process, but experiments have shown that significant annealing takes place in less than 15 s at a clad temperature of 823 K (Torimaru et al., 1996). Hence, thermal annealing may have a positive effect on clad ductility under RIA, especially in the late post-DNB phase of the transient.

3.4.2 Direct effects of clad oxide layer

The metal-water reactions at the clad outer surface introduce oxygen and hydrogen into the metal, which affects the mechanical properties of the material. These phenomena are further discussed in sections below. However, the macroscopic behaviour of the clad tube is also directly affected by the external oxide (ZrO_2) layer, which is formed at the metal-water interface.

Firstly, due to its poor thermal conductivity ($\approx 2 \text{ Wm}^{-1}\text{K}^{-1}$), the oxide layer affects the clad temperature. Under steady-state fuel operation with a typical linear heat generation rate of 20 kWm^{-1} , the clad temperature increases by approximately 0.3 K per micrometer external oxide. Hence, if spallation of a 100 μm thick oxide layer takes place, there can be temperature differences of up to 30 K between spalled regions and regions still covered with oxide. These local cold spots in clad tubes with spalled oxide have a strong effect on migration of hydrogen and precipitation of hydrides, as discussed in section 3.4.4 below.

Pulse reactor tests on high-burnup fuel rods show that clad-to-coolant heat transfer is affected by the clad oxide layer not only under steady-state conditions, but also under the RIA transient (Nakamura et al., 2000). In particular, it seems that onset of DNB is suppressed or delayed with oxidized cladding in comparison with un-oxidized or spalled cladding. To this end, it should be noticed that excessive *transient* spallation of the oxide has been observed in pulse reactor tests on highly corroded fuel rods (Schmitz & Papin, 1999). Under an RIA, this phenomenon may introduce debris into the coolant channels in a very short time. The consequences of transient oxide spallation to global core coolability are unknown, but the local effects on clad-to-coolant heat transfer are significant.

Secondly, the brittle oxide layer has a detrimental effect on clad mechanical properties. An important consequence of the oxide layer is that it leads to localization of stress and strain, which lowers the macroscopic ductility of the clad tube. When an oxidized clad tube is subjected to a tensile stress in its hoop direction, radial cracks initiate through the entire thickness of the oxide layer, as shown in figure 3.4. Since the oxide is brittle, this crack formation takes place immediately upon plastic deformation of the metal beneath the oxide. Once the oxide cracks have formed, they may act as initiation sites for further crack propagation through the subjacent metal. Unless the oxide layer delaminates from the underlying material and flakes off, the sharp oxide cracks lead to significant concentration of stress and strain to the crack tip region, and further ductile crack propagation can therefore take place through the metal with very limited plastic deformation being observable at the macroscopic scale. Hence, clad tubes with an external oxide layer exhibit macroscopically brittle behaviour, although the metal beneath the oxide may be fairly ductile (Bai, 1993). Since the stress concentration at the oxide crack rises with increasing crack length, the localization effect increases with growing oxide thickness.

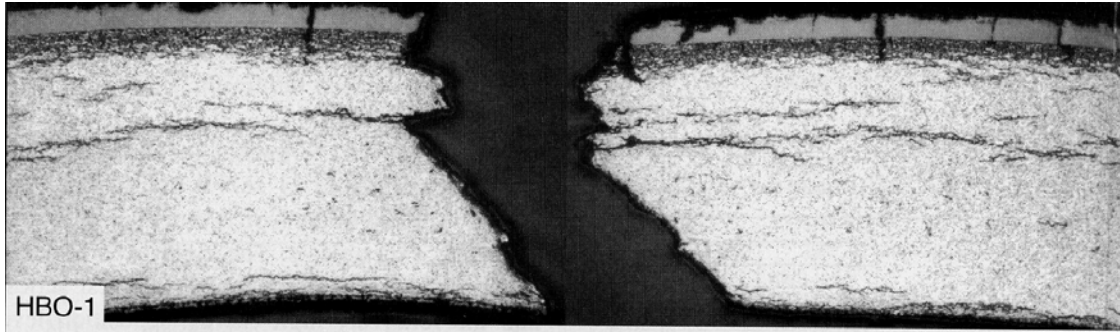


Figure 3.4: Radial oxide cracks act as stress- and strain localization sites. Photograph of clad cross section from the PWR fuel rod HBO-1, tested in the NSSR; see section A.3 in appendix A for details (Fuketa et al., 1996).

Localization of stress and strain is not only caused by cracks through the oxide, but also by spallation of the oxide layer. Clad tubes with spalled oxide have non-uniform temperature, clad wall thickness and material properties, which promotes localized deformation and therefore reduces the macroscopic ductility. Stress concentrations induced by spallation are milder than those from sharp oxide cracks, but in combination with precipitation of hydrides in spalled areas, they can still contribute to the embrittlement.

3.4.3 Effects of oxygen

Oxygen is an alloying element in zirconium alloys, which is added in quantities up to 1200 weights parts per million (wppm) in order to increase the material strength. At still higher concentrations, oxygen has a detrimental effect on ductility and fracture toughness, especially in irradiated materials.

Supported by a single experiment, Chung and Kassner (1998) state that the clad oxygen concentration increases with fuel rod burnup, due to long-term diffusion of oxygen from the oxide-metal interface into the subjacent metal. Hence, in clad tubes of high burnup fuel rods, the material directly beneath the oxide layer is expected to have reduced ductility and fracture toughness due to the locally dissolved oxygen. However, the possibility of oxygen diffusion under normal clad operating temperatures is a matter in dispute. This phenomenon is poorly investigated, and the detrimental effects of oxygen are usually neglected in comparison with the much more studied effects of hydrogen.

3.4.4 Effects of hydrogen

Hydrogen is produced in the metal-water reaction at the clad outer surface, i.e. the reaction $\text{Zr} + 2\text{H}_2\text{O} \rightarrow \text{ZrO}_2 + 2\text{H}_2$. Part of this hydrogen enters the metal, and as the oxidation proceeds, it will precipitate as zirconium hydrides. The precipitation takes place when the hydrogen concentration exceeds the terminal solid solubility, c_{TSS} , of the material.

An approximation to c_{TSS} in pure zirconium and the dilute zirconium alloys used in clad tubes is given by Northwood & Kosasih (1983)

$$c_{TSS}(T) = 1.2 \cdot 10^5 e^{-\Delta H/RT} \quad [\text{wppm}], \quad (3.1)$$

where $\Delta H = 35900 \text{ Jmol}^{-1}$ is an apparent difference between the partial molar heat of solution of hydrogen in the zirconium alloy matrix and the hydride phase, T is the temperature in Kelvin, and $R = 8.3143 \text{ Jmol}^{-1}\text{K}^{-1}$ is the universal gas constant. As long as the hydrogen is dissolved in the metal, i.e. as long as the hydrogen concentration is below c_{TSS} , hydrogen has only a minor embrittling effect. Significant degradation of clad strength and ductility is thus only observed in material with precipitated hydrides. In contrast to the irradiation-induced embrittlement described in section 3.4.1, the degradation due to hydriding does not saturate.

3.4.4.1 Embrittling mechanisms

Hydrogen dissolved in the metal migrates by thermo-diffusion towards cold regions of the cladding, and will thus accumulate close to the comparatively cold outer surface of the clad tube (Sawatzky, 1960). When the local hydrogen concentration exceeds the terminal solid solubility, zirconium hydrides precipitate in the form of thin platelets. The hydrides have either of two crystallographic structures; δ -hydrides ($\text{ZrH}_{1.5}$ to $\text{ZrH}_{1.66}$) with a face-centred cubic structure exist for lower hydrogen concentrations, whereas ϵ -hydrides ($\text{ZrH}_{1.66}$ to ZrH_2) with a face-centred tetragonal structure exist at higher hydrogen concentrations.

The degree of embrittlement due to hydride precipitation is dependent on the amount of hydrogen in excess of the solubility limit, as well as on size, orientation and distribution of the hydrides. Hydride-induced embrittlement is a complex matter, and several mechanisms contribute to the loss of clad strength and ductility (Northwood & Kosasih, 1983):

At hydride concentrations exceeding 250-300 wppm, the embrittlement is mainly due to hydride fracture, i.e. crack propagation is possible through a network of more or less interconnected hydrides, which provide a brittle crack path through the material. This mode of fracture is very sensitive to the hydride orientation with respect to the direction of tensile stress. This is further discussed in section 3.4.4.4 below.

At lower hydride concentrations, continuous crack paths through hydrides cannot be formed. In this case, the embrittlement is attributed to two different effects, pertaining to irradiated and un-irradiated materials, respectively. In irradiated zirconium alloys, plastic deformation takes place in dislocation channels with limited extension, and may therefore be hindered even by a moderate concentration of hydrides (Garde et al., 1996). In an un-irradiated material, plastic deformation takes place uniformly, and it is therefore not so easily hindered by sparsely located hydrides. In this case, the embrittlement is likely due to the fact that hydrides promote initiation and link-up of voids in the material (Yunchang & Koss, 1985). Nucleation and growth of voids reduce the macroscopic ductility of the material, even though the solid material between the voids possesses significant ductility.

The fact that different embrittling mechanisms come into play, depending on the hydride concentration, temperature, irradiation dose and stress state in the material, makes it difficult to interpret experimental data. In addition, there are also differences between tested materials, e.g. in alloy composition and heat treatment, which further complicates the picture. To this end, it should be noticed that the majority of published studies on “hydrided cladding” have been performed on un-irradiated materials, which are charged with hydrogen under elevated temperature in a laboratory environment. Although the hydride distribution and morphology in these materials usually seem similar to those in clad tubes subjected to in-reactor irradiation and oxidation, one should bear in mind that the behaviour observed for the laboratory-type materials is not necessarily representative for in-pile cladding materials. In particular, the effects of irradiation, oxygen uptake and the presence of an external oxide layer are overlooked in tests on laboratory-type materials.

3.4.4.2 Influence of temperature

Temperature is a key parameter for the behaviour of hydrogen in zirconium alloys (Sawatzky, 1960). Firstly, solubility of hydrogen increases with temperature, and hydrides therefore precipitate preferentially in cold regions of the clad tube. The temperature field thus controls the distribution of precipitated hydrides in the material. Secondly, thermo-diffusion of dissolved hydrogen results in migration of hydrogen downhill temperature gradients, and hydrogen will thus migrate towards cold regions of the cladding. Thirdly, hydrided zirconium alloys undergo a ductile-to-brittle transition at a certain temperature, when the hydride content is high enough that hydride fracture is the dominating embrittling mechanism; see section 3.4.4.1. From experiments, it is well known that hydride embrittlement is more pronounced at room temperature compared to typical in-reactor clad temperatures, and studies have been performed to determine ductile-to-brittle transition temperatures (DBT) for hydrided clad materials. A tentative DBT for highly irradiated Zircaloy-4 (Zr-1.5Sn-0.2Fe-0.1Cr by wt%) is shown in figure 3.5.

Figure 3.5 clearly shows that for hydrogen concentrations up to 1000 wppm, the ductile to-brittle transition occurs between room temperature and typical in-reactor clad temperatures (570-620 K). This conclusion is corroborated by experiments on other LWR clad materials, e.g. (Wisner & Adamson, 1998) and (Arsene et al., 2003), as well as by tests on the Zr-2.5%Nb material used in CANDU reactors (Wallace et al., 1989). Therefore, we may expect a significantly more brittle behaviour of severely hydrided cladding under CZP than under HZP RIA in BWRs.

Finally, it should be noted that a ductile-to-brittle transition is difficult to define unambiguously. It can be defined either from a change in macroscopic material properties, such as total elongation or area reduction in tensile tests, or from a change in visual appearance of fracture surfaces, examined locally by microscopy. Since it has been observed that a change in macroscopic behaviour from ductile to brittle need not be reflected in a corresponding change of fractographical appearance, the definition of a ductile-to-brittle transition is somewhat arbitrary (Bertolino et al., 2003) and (Balourdet et al., 1999).

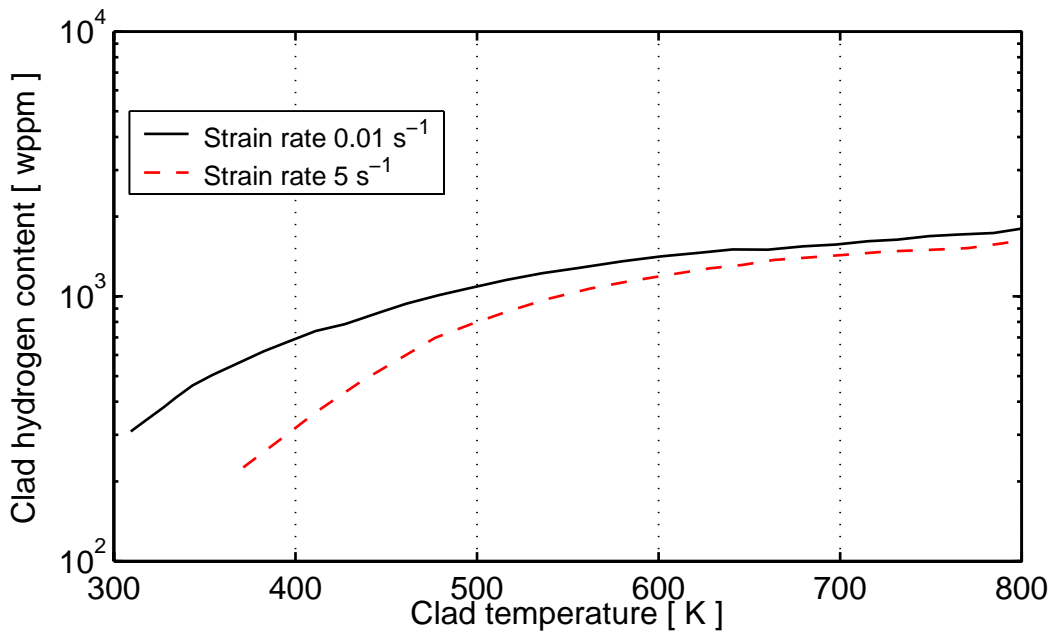


Figure 3.5: Tentative ductile-to-brittle transition temperature for irradiated Zircaloy-4, determined through axial tensile tests at two different strain rates. From Balourdet et al., (1999).

3.4.4.3 Influence of hydride distribution

In experimental studies on hydride-induced embrittlement of clad tubes, the distribution of hydrides in the material has been found equally important as the average hydride content. Most reported studies, e.g. those of Nagase et al. (1995), Fuketa et al. (2000) and Daum et al. (2002) have been performed on un-irradiated materials, which have been artificially hydrided in laboratory environment to obtain desired distributions of hydrides. These investigations have generally shown that, for the same average hydride content, materials with uniformly distributed hydrides are more ductile than those having local concentrations of hydrides in certain regions.

This result has bearing upon the formation of hydride rim structures in highly oxidized and hydrided cladding tubes, which arise from the radial temperature gradient and its effects on migration and precipitation of hydrogen; see section 3.4.4.2. Irradiated and oxidized BWR clad tubes usually have fairly uniform hydride distributions, whereas PWR clad tubes have radial concentration gradients. The tendency for these concentration gradients to turn into layered structures, with a densely hydrided rim at the clad outer surface, as shown in figure 3.4, increases with clad surface heat flux, average hydrogen content and also with the strength of the radial temperature gradient.

A common finding in experiments on laboratory-hydrided un-irradiated material, such as those by Daum et al. (2002), Fuketa et al. (2000) and Pierron et al. (2003), is that the ductility decreases rapidly with increasing thickness of the hydride rim at the clad outer surface. The ductility decreases up to a rim thickness of about 100 μm , after which the embrittlement seems to saturate, and for thicker rims than 100 μm , the ductility is fairly constant.

Daum et al. (2002) and Pierron et al. (2003) have suggested that this results from the fact that the brittle hydride rim cracks at low plastic strain, and that the cracks act as nucleation sites for further crack propagation through the ductile material beneath the rim. Hence, in laboratory-hydrided materials, the hydride rim seems to play the same role as the external oxide layer in in-pile oxidized clad tubes; see section 3.4.2. At present, it is not clear whether the localization effects from the oxide layer and the subjacent hydride rim are additive. If they are, one could suspect that there is a threshold of about 100 μm for the combined oxide + hydride rim thickness, above which the embrittlement saturates.

For irradiated clad materials, there are only a few reported experiments that focus on the influence of a radial gradient in hydride concentration. Garde et al. (1996) tested highly irradiated and corroded Zircaloy-4 cladding, and concluded that the important parameter affecting clad ductility is the *local* hydride concentration, rather than the *average* concentration. Their findings thus corroborate the conclusions drawn in aforementioned tests on un-irradiated materials, that presence of a hydride rim at the clad outer surface has a detrimental effect on clad ductility. This conclusion is also indirectly supported by tests performed on irradiated Zircaloy-2 (Zr-1.5Sn-0.15Fe-0.1Cr-0.05Ni by wt%) by Wisner and Adamson (1998). They tested material taken from water rod tubes, which operate without a temperature gradient, and consequently have an almost uniform hydride distribution. This material was found to have superior ductility in comparison to materials with similar average hydride content, but with the hydrides concentrated to a rim at the clad outer surface.

The detrimental effects of a hydride rim on clad ductility can be understood and successfully modelled by use of fracture mechanics (Kuroda et al., 2001) and (Kuroda & Yamanaka, 2002). However, this is only true as long as crack propagation in the inward radial direction of the clad tube is concerned. When it comes to crack propagation in the tube axial direction, Fuketa et al. (2000) found no detrimental effect of a hydride rim in burst tests on un-irradiated Zircaloy-4 cladding. On the contrary, axial cracks were found to be shorter in samples with hydride rims than in uniformly hydrided samples with similar average hydride content. A reasonable explanation to this observation is that the inner part of the cladding, with low hydride content, had a strong beneficial effect on fracture toughness in the axial direction, which outweighed the detrimental effect of the hydride-rich outer rim.

The non-uniform distribution of hydrides in the clad tube radial direction has received much attention, since it is a consequence of the unavoidable radial temperature gradient under operation. However, gradients in temperature and hydride concentration may under certain conditions appear also in the tube axial and circumferential directions. Regions with high concentrations of hydrogen and clad hydride content are often found at pellet-pellet interfaces, since the clad temperature is somewhat lower at these locations. If inter-pellet axial gaps occur in the fuel column, massive hydriding may appear at the resulting cold rings of the clad tube (Forsberg & Massih, 1990).

Severe local hydriding can also result from spallation of the oxide layer, that creates cold spots at which hydride blisters may form. As shown in figure 3.6, these blisters are lens-shaped, typically a few millimetres in diameter, and contain a very high hydride concentration or even massive hydride (Garde et al., 1996).

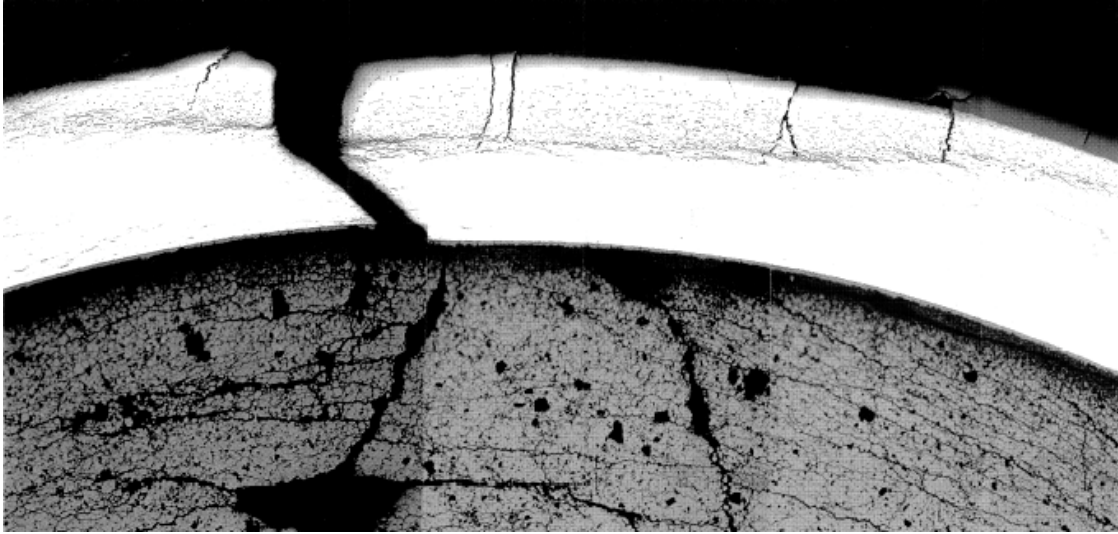


Figure 3.6: Clad failure initiated at a hydride blister in the CABRI REP Na-8 pulse reactor test (Papin et al., 2002).

The influence of hydride blisters on clad ductility has recently been both experimentally and theoretically studied by Pierron et al. (2003). From tensile tests on small-scale un-irradiated Zircaloy-4 specimens with artificially induced hydride blisters, they found that the loss of local ductility correlated well with blister depth. The observed behaviour was successfully explained by an analysis based on non-linear fracture mechanics, in which it was assumed that the blisters provide initiation sites for radial cracks. Hence, it seems that local hydride blisters play a similar role as a hydride rim or external oxide layer for initializing radial cracks, thereby degrading the macroscopic ductility of the cladding.

3.4.4.4 Influence of hydride orientation

Hydrides precipitate in the form of thin platelets, and the orientation of these platelets with respect to residual or applied tensile stresses strongly influences the embrittlement. The orientation of hydrides in clad tubes is affected by the thermo-mechanical treatment of the tubes under manufacturing, and by the stress state prevailing under precipitation. In general, hydride platelets are oriented with their surface normals preferentially aligned to the clad tube radial direction, and the width of the platelets along the tube axial direction is significantly larger than in the circumferential direction. These hydrides, usually termed ‘circumferential’ hydrides, have only a moderate embrittling effect, since there is no tensile stress in the clad tube radial direction, i.e. in the direction perpendicular to the hydride platelets (Northwood & Kosasih, 1983).

However, there are also hydride platelets oriented with their surface normals more or less aligned to the clad circumferential direction. These hydrides, which are usually termed ‘radial’ hydrides, are much more deleterious, since they are perpendicular to the dominating tensile stress in clad tubes of high-burnup fuel rods.

The fraction of these detrimental radial hydrides is larger in recrystallization annealed (RXA) clad materials than in materials subjected to milder heat treatments, such as stress relieved annealed (SRA) cladding (Northwood & Kosasih, 1983). The former heat treatment results in a larger fraction of grain boundaries in the radial direction, and since hydrides tend to precipitate along grain boundaries, this could to some extent explain the differences in hydride orientation between RXA and SRA materials. However, there are also other causes to these differences, such as material texture.

Nakamura et al. (2002b) have reported a more brittle fracture behaviour for typical RXA BWR cladding than for SRA PWR materials, when tested under similar conditions in the NSRR. To this end, it would be interesting to compare the performance of the M5 material (Zr-1.0Nb-0.13O by wt%), which is in RXA state, with other PWR materials that are all in SRA state. One of the benefits of M5 is its low hydrogen pickup fraction, which will reduce the embrittlement effect of hydrogen, but this beneficial feature may be offset by a more radial orientation of the hydrides.

The hydride orientation in the clad tube is not only governed by the thermo-mechanical treatment of the material under fabrication, but also by the stress state prevailing under hydride precipitation. The hydride platelets have a tendency to precipitate perpendicular to the direction of the major principal stress, provided that this stress is tensile (Northwood & Kosasih, 1983). In a cladding tube, the fraction of radial hydrides will consequently increase with burnup, as a result of growing PCMI-induced tensile hoop stresses. Moreover, one could suspect that the fraction of radial hydrides increases in fuel rods subjected to PCMI-induced loading under high power or load-follow operation, as a result of elevated hoop tensile stresses (Chung & Kassner, 1998).

3.5 Influence of fuel pellet conditions on failure propensity

Also the material properties of the fuel pellets change as a result of in-reactor operation. Of particular interest to the fuel rod behaviour under RIA at high burnup is the local buildup of fissile plutonium isotopes and fission products at the fuel pellet periphery. This phenomenon leads to power- and temperature profiles, which are strongly peaked to the pellet surface. It also leads to the formation of a porous rim zone microstructure, which has the potential to affect fuel deformation behaviour and fission gas release in high-burnup fuel (Jernkvist & Massih, 2002).

3.5.1 Radial distribution of power

As UO₂ nuclear fuel is taken into operation, there is a successive change in the radial distribution of fissile material, power and fission products within the fuel pellets. In fresh fuel, the fissile material consists predominantly of ²³⁵U, which is usually uniformly distributed in the fuel pellets. Hence, both power and fission products are generated with a relatively small variation along the fuel pellet radius. However, with increasing burnup, there is a non-uniform buildup of fissile plutonium isotopes through resonance capture of epithermal neutrons by ²³⁸U and subsequent β-decays into ²³⁹Pu and heavier fissile isotopes of plutonium.

Since the neutron capture takes place mainly at the pellet surface, the distributions of fissile material, fission rate and fission products will develop marked peaks at the pellet surface as fuel burnup increases. The shapes of these distributions are dependent not only on irradiation time, but also on the fuel initial content of ^{235}U , pellet radius and the neutron energy spectrum of the reactor. This was illustrated in figure 3.2, section 3.2.2.

Under the initial phase of an RIA, the fuel is heated almost adiabatically, i.e. without heat transfer taking place either inside the fuel pellets or across the pellet-clad gap. During this initial heat-up phase, the radial temperature profile in the pellets therefore agrees very closely to the radial power profile; the faster the energy deposition, the closer is the agreement. This is illustrated in figure 3.7, which shows the radial temperature distribution, calculated at the peak power axial position and at the time of maximum power, for the REP Na-5 rod in the CABRI pulse reactor; see section A.4 in appendix A for details. The normalized radial power profile is shown for comparison. Due to the high burnup of the fuel, $64.4 \text{ MWdkg}^{-1}\text{U}^{-1}$ pellet radial average value, both power and temperature profiles are strongly peaked to the pellet surface.

Hence, the pellet temperature profiles in high-burnup fuel under the early phase of an RIA are very much different from the typical parabolic profiles obtained under normal fuel operation. The surface-peaked temperature profiles lead to rapid thermal expansion of the fuel rim, which induces strong thermal stresses that could possibly lead to fragmentation of the material (Lespiaux et al., 1997). The fragmentation is assisted by stresses induced by expanding fission gases, which are accumulated in grain boundary bubbles and pores within the peripheral rim zone of the pellets.

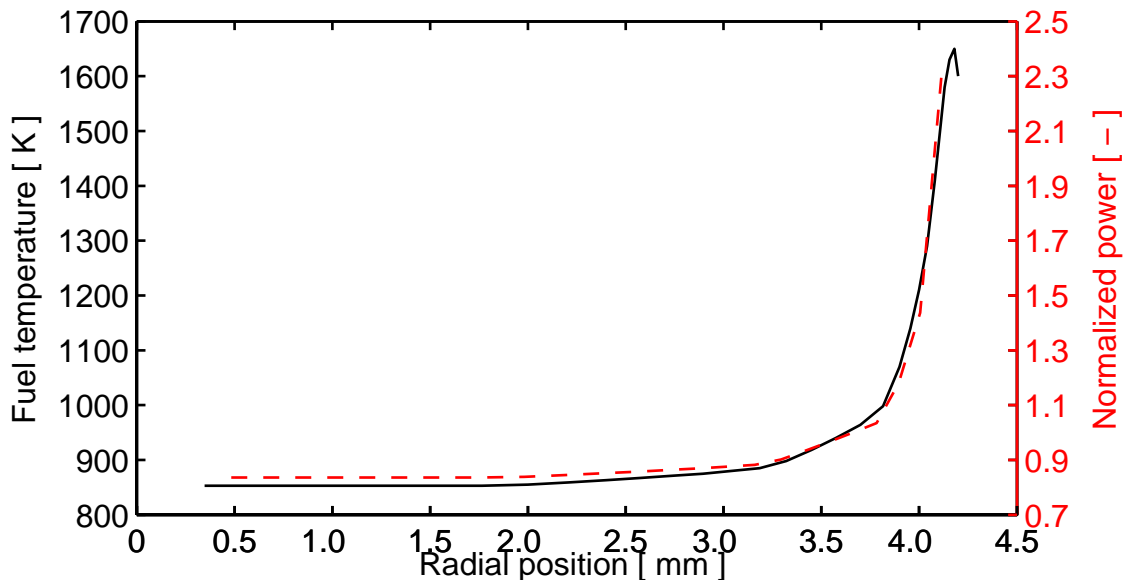


Figure 3.7: Typical temperature (solid line) and power distribution (dashed line) in high-burnup fuel, subjected to fast power pulse. Simulation of the CABRI REP Na-5 pulse reactor test, by use of the SCANAIR computer code. The results refer to the peak power axial position and time.

3.5.2 Rim zone microstructure

As a consequence of accumulated fission products, enhanced local burnup and fission rate in combination with low temperature, a re-structuring of the fuel material takes place at the pellet peripheral rim in high-burnup fuel. Formation of this rim zone microstructure is characterized by a simultaneous reduction in grain size, increase in porosity and depletion of fission gas from the UO₂ matrix, (Matzke, 1995) and (Spino et al., 1996). The formation starts at a local burnup of 60-70 MWdkg⁻¹U⁻¹ by subdivision of grains at the fuel pellet outer surface and at pores and bubbles close to the surface. The progression of the re-structuring process, and the inward propagation of the rim zone towards the pellet centre, is controlled by the radial distributions of both fissile material and temperature. In commercial LWR fuel, the radial width of the rim zone is usually less than 200 µm (Jernkvist & Massih, 2002).

Under normal reactor operation, the fuel temperature in the rim zone is generally below 800 K, and the highly porous material is mechanically stable. However, as shown in figure 3.7 of the preceding subsection, under the initial phase of an RIA, the temperature profile is peaked to the pellet rim zone. As a consequence, the mechanical stability of the material may be lost, either through fragmentation or by fission gas induced swelling.

3.5.2.1 Fuel fragmentation

In ceramographic examinations of high-burnup fuel, which has undergone simulated RIA in pulse reactors, it is usually found that the outermost part of the pellet is fragmented (Lespiaux et al., 1997) and (Fuketa et al., 2000). Typically, a large number of radial cracks are seen at the pellet surface, and these cracks extend a few millimeters towards the pellet centre, i.e. well beyond the re-structured rim zone. These cracks are probably caused by tensile hoop stresses during cool-down of the pellet periphery, i.e. the cracks nucleate late in the transient. In some cases, circumferential cracks are also found at the boundary between the re-structured rim zone and the subjacent part of the pellet. These cracks are most likely caused by tensile radial stresses during the early heat-up phase.

The radial and circumferential cracks described above create fairly large fuel fragments. Much finer fragments have been observed in fuel subjected to power pulses shorter than 10 ms, e.g. for most rods tested in the NSRR and some of the rods tested in CABRI. These fragments result from grain decohesion, caused by overpressurization of gas-filled pores and intergranular bubbles under rapid rise in temperature (Lemoine, 1997). The fuel rim zone microstructure, with its high density of grain boundaries and gas-filled pores, is believed to be particularly sensitive to this fragmentation mechanism. The resulting fragments are very small, typically about 50 µm, and can therefore be easily expelled through cladding cracks in a failed fuel rod (Lespiaux et al., 1997) and (Fuketa et al., 1997). Hence, post-failure fuel dispersal is promoted by this fragmentation mechanism. Moreover, grain decohesion is also believed to aggravate fuel-coolant interaction, due to the large surface-to-volume ratio of the small fragments.

However, grain boundary fragmentation has only been observed in tests with power pulses shorter than 10 ms (Lespiaux et al., 1997). Since a true RIA event is expected to be significantly slower, the concern for this phenomenon may be unjustified. The same is true for the concern about possible contributions of grain boundary fragmentation to the mechanical loading of the clad tube.

3.5.2.2 *Transient fission gas swelling*

The local buildup and accumulation of gaseous fission products in the porous rim zone has been identified as a potential cause to fuel swelling under the elevated temperatures associated with an RIA by many investigators (Lemoine, 1997) and (Nakamura et al., 1996). The fuel swelling from growth of overpressurized pores and bubbles would add to the thermal expansion, and thus aggravate the pellet-clad mechanical interaction in high-burnup fuel. However, the current view seems to be that gaseous swelling is too slow to contribute to PCMI loading under the early heat-up phase of an RIA in UO₂ fuel rods, but that the phenomenon may play a role for MOX fuel. If gaseous swelling does occur in UO₂ fuel, it is believed to follow *after* the power pulse, at a time when the cladding is heated and the material therefore able to withstand large plastic deformation without rupture (Nakamura et al., 1996) and (Nakamura et al., 2002a).

Since the extent of gaseous swelling is dependent on the amount of accumulated fission gases in the fuel, and consequently on the fuel burnup, it is reasonable to expect a change in fuel rod deformation behaviour with increasing burnup. This conjecture is confirmed by figure 3.8, in which we have plotted the measured clad hoop plastic strain for all surviving UO₂ rods in the CABRI REP-Na test series with respect to the increase in fuel enthalpy under the tests.

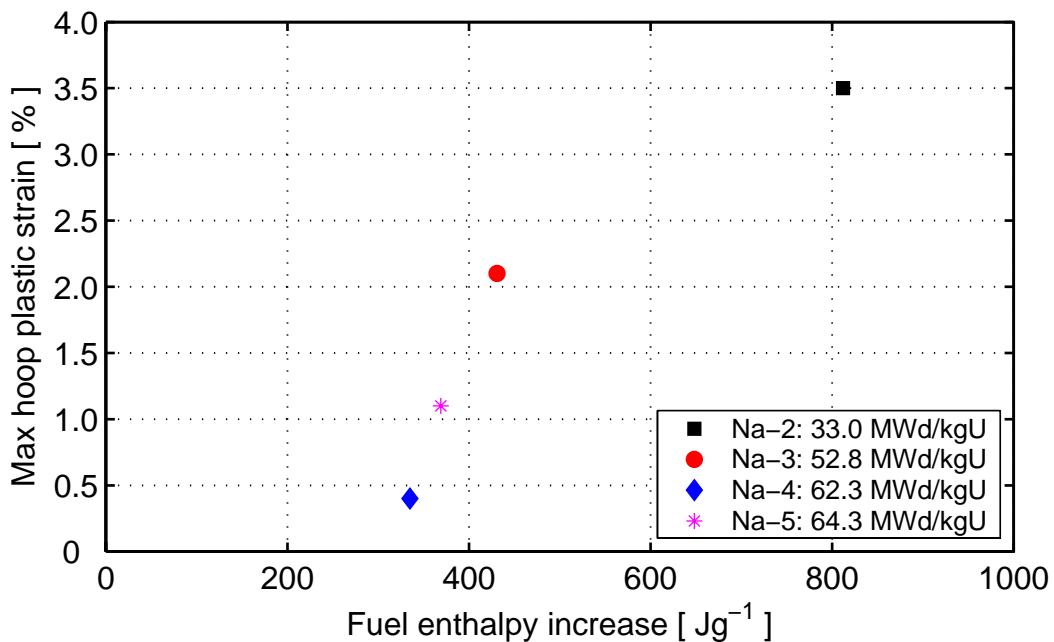


Figure 3.8: Maximum clad plastic hoop strain vs. enthalpy increase for surviving UO₂ rods in the CABRI REP-Na test series.

Clearly, the clad deformation in the high-burnup rods Na-3 to Na-5 is proportional to the enthalpy increase, but the intermediate-burnup rod Na-2 does not follow this linear trend. In comparison with the high-burnup rods, its deformation is surprisingly small, considering the large enthalpy increase. The deviation is most likely due to the fact that rod Na-2 has a smaller inventory of retained fission gases in the fuel, and therefore exhibits less gaseous swelling. This supposition is corroborated by the low transient fission gas release observed in rod Na-2, in comparison with the other rods; see section A.4 in appendix A for details on the tests.

Another observation to make in figure 3.8, is that there is an apparent threshold enthalpy increase of roughly 310 Jg^{-1} (75 calg^{-1}) for onset of clad plastic deformation. This threshold is easily estimated by extrapolating a straight line through the Na-3 to Na-5 data points to its intersection with the x-axis in figure 3.8. As a matter of fact, Vitanza (2002) has proposed a clad failure limit for RIA, based on this apparent enthalpy threshold. However, the applicability of the proposed failure limit to LWR RIA scenarios must be questioned, since the test conditions in the CABRI reactor are not typical for LWRs. This is further discussed in section 4.1.2.

Finally, experimental data from pulse reactor tests clearly show that transient fission gas swelling is much more pronounced in MOX fuel than in UO_2 fuel at similar burnup (Fuketa et al., 2000) and (Sasajima et al., 2000). As touched upon in section 3.2.2, this is a consequence of the heterogeneous structure of MOX fuel, which leads to high fission gas release and gas-induced swelling.

3.5.2.3 Thermal conductivity degradation

An important aspect of high fuel burnup and the formation of a rim zone microstructure is the degradation of fuel thermal conductivity. The degradation is primarily caused by an increased resistance to phonon heat transport, as irradiation damage and fission products accumulate in the crystal lattice (Lucuta et al., 1996). Theoretical models for thermal conductivity of solids, by which the effects of porosity, grain size and lattice defects can be evaluated, indicate that the thermal conductivity should decrease in the fuel rim zone as a consequence of grain subdivision and increased porosity (Jernkvist & Massih, 2002).

The thermal conductivity degradation in high-burnup fuel hinders the radial heat transfer, and leads to an undesired increase in fuel temperature under steady-state reactor operation. The effects of fuel thermal conductivity degradation on fuel rod behaviour under RIA are largely unknown. However, from the tests performed in the NSRR, it is known that departure from nucleate boiling at the clad-to-coolant interface is affected by changes in heat transfer properties of the fuel rod (Nakamura et al., 2000). In particular, it has been found that DNB is suppressed or delayed, when radial heat transfer is hindered by e.g. a large pellet-clad gap or an external clad oxide layer. Although direct experimental evidence on this subject is lacking, the fuel thermal conductivity degradation is expected to have a similar effect on DNB.

3.5.3 Transient fission gas release

Release of retained fission gases under RIA increases the fuel rod internal gas pressure, thereby contributing to the mechanical loading of the clad tube. From simultaneous on-line measurements of clad deformation and rod internal gas pressure under pulse reactor tests in the NSRR, it is clear that the pressure loading from fission gas release (FGR) comes into play somewhat later than the PCMI-induced loading from the thermally expanding fuel pellets (Nakamura et al., 2000) and (Fuketa et al., 2003). Hence, FGR is probably too slow to contribute to clad mechanical loading under the critical heat-up phase of an RIA, but still, it increases the risk for clad high-temperature creep rupture later in the transient.

The fractional release of accumulated fission gas under RIA simulation tests on high-burnup UO_2 fuel rods is generally high, typically in the range from 5 to 25%, and it correlates well with rod burnup and peak fuel enthalpy under the tests (Fuketa et al., 2001), (Lemoine, 1997) and (Nakamura et al., 2000). There is also evidence that transient FGR under RIA is influenced by the steady-state power history experienced by the fuel prior to the transient. Fuel rods operated at elevated steady-state power have shown particularly large FGR, not only under steady-state operation, but also under the subsequent pulse reactor tests in the NSRR (Fuketa et al., 2000). This suggests that release paths for the fission gas, generated during steady-state operation, play an important role for the transient FGR under RIA. However, it must be recognized that the transient FGR under RIA takes place partly by other mechanisms than the two-stage diffusion process that is operative under normal steady-state operation. For example, the grain boundary decohesion discussed in the previous section provides a mechanism for prompt release of gas from intergranular bubbles, which is particular to RIA (Lemoine, 1997).

Two final comments should be made on the differences between mechanical loading imposed on the clad tube by released fission gases and by PCMI. Firstly, the pressure loading from released fission gases is an unstable type of loading, whereas PCMI results in a stable, displacement-controlled loading (Montgomery et al., 2004). Consequently, the failure behaviour of the fuel rod may depend on which type of loading is dominant. Secondly, pressure loading results in a clad stress state with a stress biaxiality ratio $\sigma_{zz}/\sigma_{\theta\theta}$ close to 1/2, whereas loading from PCMI results in a nearly biaxial stress state with $\sigma_{zz}/\sigma_{\theta\theta}$ close to 1. Here, σ_{zz} and $\sigma_{\theta\theta}$ is the axial and tangential component of cladding stress, respectively.

The clad stress state under RIA is illustrated in figure 3.9, which shows the calculated clad biaxiality ratio as a function of time for the CABRI REP Na-2 pulse reactor test. The power pulse is shown for comparison. The clad stress state is completely biaxial during the power pulse, as a result of PCMI. After the power pulse, the pellet-clad gap opens, and the clad tube is loaded only by the rod internal gas pressure.

The difference in stress state from PCMI and pressure loading is important, since the stress biaxiality has significant impact on clad tube ductility. As will be shown in section 5.2.1, the clad material may accommodate twice as large plastic hoop strains under internal pressure loading than under the PCMI-induced biaxial loading.

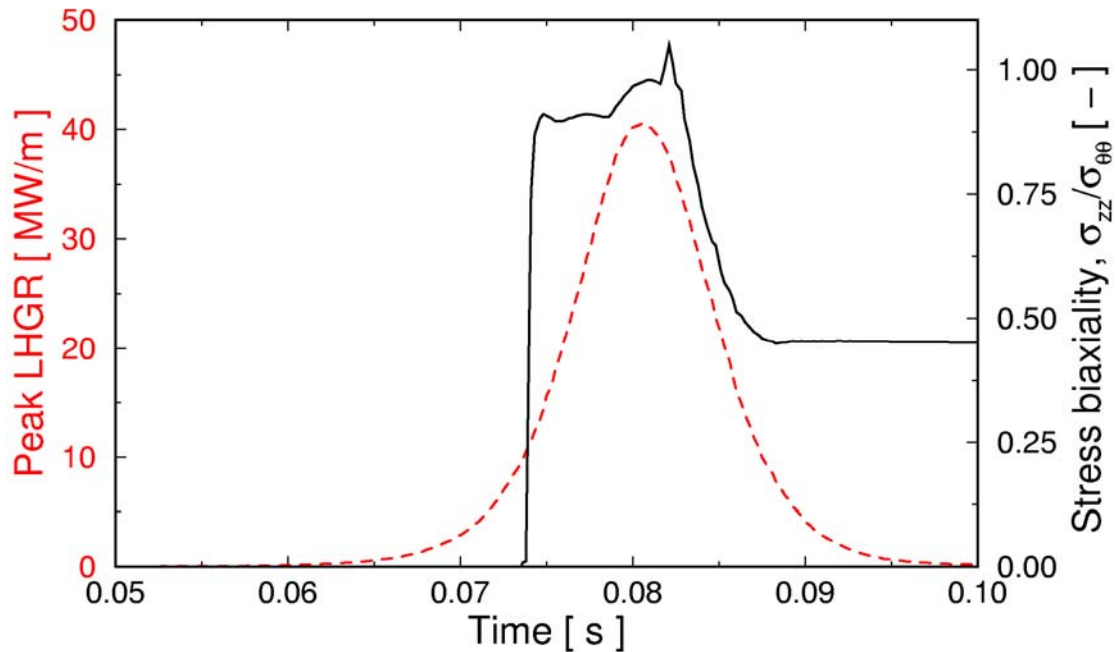


Figure 3.9: Simulation of CABRI REP-Na2 pulse reactor test by use of the SCANAIR computer code. The solid line is the calculated clad biaxiality ratio, and the dashed line is the power pulse. Both parameters are evaluated at the peak power axial position of the fuel rod. Here, σ_{zz} and $\sigma_{\theta\theta}$ is the axial and hoop cladding stress, respectively.

3.5.4 Pellet-clad contact and bonding

The state of pellet-clad contact has a strong impact on the forces transferred to the clad tube from the expanding fuel pellet stack under RIA. Of particular importance is the transfer of axial forces from the fuel column to the clad tube, since these forces introduce a detrimental biaxial stress state in the cladding. From simultaneous on-line measurements of clad tube and fuel stack elongation under pulse reactor tests in the NSRR, it is clear that the clad elongation closely follows the fuel stack elongation, once the pellet-clad gap has closed (Ishijima & Nakamura, 1996) and (Nakamura et al., 2000). Hence, axial sliding between fuel and clad is very unlikely, and this seems to be true for both fresh and high-burnup fuel rods.

In the most severe scenarios for RIAs, the transient starts from zero or very low fuel rod power. For these scenarios, there will thus be a certain radial gap between pellet and cladding at onset of the transient, and only the fuel expansion occurring after closure of this gap need be accommodated by the cladding tube. Consequently, the pre-transient gap size affects the PCMI-induced loading. The pre-transient gap size depends on the as-fabricated gap size, fuel swelling and clad creep-down, which is slower in BWRs than in PWRs. In the pulse reactor tests performed in the NSRR, clad deformations are significantly smaller in BWR than in PWR tests, if fuel rods with similar burnup and peak enthalpy are compared (Fuketa et al., 2000) and (Nakamura et al., 2002a).

In this connection, attention should be paid to the phenomenon of pellet-clad bonding, which may aggravate the pellet-clad mechanical interaction under RIA in high-burnup fuel rods (Nogita & Une, 1997). This phenomenon has been observed in a few high-burnup BWR fuel rods with Zr-liner cladding, belonging to the FK test series in the NSRR; see section A.3 in appendix A. In these rods, the pre-transient gap was completely closed as a consequence of extensive pellet-clad bonding, and PIE results indicate that intense PCMI loading of the clad tube occurred under the tests.

4 Experimental database

More than 80 pre-irradiated LWR fuel rods have so far been studied under simulated RIA conditions in pulse reactor experiments. These investigations provide valuable information on the fuel rod thermo-mechanical behaviour under RIA, and in particular, on the mechanisms of fuel rod failure. In section 4.1, we present a brief review of these investigations, with special attention paid to recent tests on high-burnup fuel rods. A more lengthy presentation, including the most important test results, is given in appendix A. Since there are considerable differences between the pulse reactors used in these studies and commercial LWRs, we also discuss the typicality of each test facility with respect to e.g. power pulses and coolant conditions.

Section 4.2 contains a summary of out-of-pile mechanical property tests, which provide the bases for our derivation of a clad failure criterion. A more detailed compilation of the considered tests, including results and information on test conditions, is given in appendix B. The mechanical property of primary interest is the clad ductility, or more precisely: the maximum hoop plastic strain that a clad tube can sustain under temperature- and loading conditions relevant to the heat-up phase of an RIA.

4.1 Pulse reactor tests

4.1.1 Overview of pulse reactor tests

Under the past four decades, RIA simulation tests have been conducted on pre-irradiated LWR fuel rods in four different power pulse reactors:

- SPERT-CDC (Special Power Excursion Reactor – Capsule Driver Core)
Experiments performed in the United States 1969-1970.
- PBF (Power Burst Facility)
Experiments performed in the United States 1978-1980.
- NSRR (Nuclear Safety Research Reactor)
Ongoing experiments in Japan, carried out since 1980.
- CABRI
Ongoing experiments in France, carried out since 1993.

The test conditions, as well as the investigated fuel rods, differ significantly between these studies. This is illustrated in table 4.1, which summarizes test conditions and key fuel rod properties in each experimental program.

Facility	SPERT	PBF	NSRR	CABRI
Reactor conditions				
Coolant medium	Stagnant water	Flowing water	Stagnant water	Flowing sodium
Coolant temperature [K]	298 (25 °C)	538 (265 °C)	298 (25 °C)	553 (280 °C)
Coolant pressure [MPa]	0.1	6.45	0.1	0.3
Power pulse width [ms]	13 - 31	11 - 16	4 - 7	9 - 75
Fuel rods tested				
Number of tests (PWR/BWR/MOX)	10 (0/10/0)	17 (17/0/0)	47 (26/16/5)	14 (10/0/4)
Burnup [MWdkg ⁻¹ U ⁻¹]	1 - 32.7	0 - 6.1	26.0 - 61.0	33.0 - 64.3
Clad oxide thickness [μm]	0 - 65	0 - 5	4 - 60	4 - 130
Rod active length [mm]	132	≈ 1000	122 - 135	440 - 1000
Peak fuel enthalpy [Jg ⁻¹] (calg ⁻¹)	570 - 1180 (137 - 282)	770 - 1190 (185 - 285)	155 - 605 (37 - 145)	400 - 950 (96 - 228)
Lowest failure enthalpy [Jg ⁻¹] (calg ⁻¹)	356 (85)	586 (140)	251 (60)	125 (30)

Table 4.1: Overview of pulse reactor tests on pre-irradiated LWR fuel rods. The peak and failure enthalpies are axial peak, radial average values for the fuel pellet. It should be noted that the JMTR tests are not included in the NSRR data; see section 4.1.5 for further details.

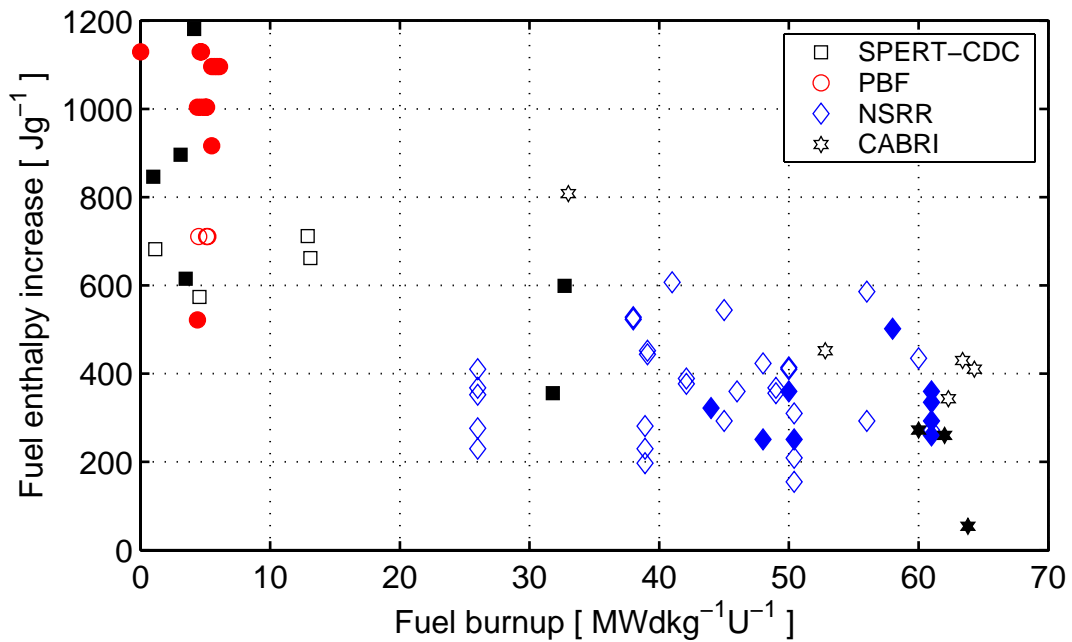


Figure 4.1: Fuel enthalpy increase vs. burnup for uranium dioxide fuel rods. Filled symbols represent failed rods, whereas open symbols are survivals. It should be noted that the JMTR tests are not included in the NSRR data.

In figure 4.1, we have plotted the results of all pulse reactor tests on pre-irradiated fuel rods with respect to fuel burnup. Open symbols represent fuel rods that have survived the tests, whereas filled symbols are failed rods. For the failed rods, the presented fuel enthalpy increase is the increase up to the point of failure, provided that the point of failure is known. Otherwise, the peak fuel enthalpy increase under the test is used. All enthalpies are axial peak, radial average values.

We have plotted the data in figure 4.1 with respect to fuel enthalpy increase during the tests, rather than total enthalpy, because the enthalpy increase is more directly related to the PCMI-induced clad loading under RIA. It is interesting to note the scarcity in data for low and intermediate burnup levels, that is for burnups in the range from 6 to 38 MWdkg⁻¹U⁻¹.

4.1.2 Typicality of test reactor conditions

As shown in table 4.1, the coolant conditions in PBF are close to those expected at HZP in BWRs, but the coolant conditions in the other pulse reactors are different from those in commercial light water reactors. In particular, they differ from the conditions at HZP in PWRs, i.e. flowing water at a temperature of about 300 °C and 15 MPa pressure. This non-typicality makes it difficult to directly apply the results of pulse reactor tests, when formulating fuel rod operating limits for commercial light water reactors. Unfortunately, there are also other differences between the pulse reactor tests and the conditions expected under RIA in LWRs:

- Realistic 3D reactor kinetics simulations of postulated RIA scenarios in high burnup fuel indicate that the pulse widths are at least 30 ms in LWRs (Agee et al., 1995), (Diamond et al., 2002) and (Nakajima et al., 2002). Hence, most pulse reactor tests have been performed with unrealistically narrow pulses.
- As shown in table 4.1, the pulse reactor tests are made on short-length rodlets, and in all but the PBF reactor, the test rods are subjected to a nearly uniform axial power profile throughout the entire transient.

The length of the rod, and also the distribution of power along the rod as a function of time, could affect the transfer of axial forces from the expanding fuel pellets to the cladding. Hence, the cladding stress state in pulse reactor rodlets may not be the same as in full-length LWR rods. However, the PBF tests were nearly prototypical in this respect.

In addition to the non-prototypical test conditions, there is also non-typicality in fuel rod design and pre-irradiation conditions. In particular, it should be noted that the design of the SPERT rodlets was very different from that of LWR fuel rods. The fuel enrichment was increased and the fuel and cladding diameters were reduced in order to increase the attainable energy deposition.

Moreover, some of the rodlets were pre-irradiated in the ETR¹ facility at very high power levels, resulting in fuel restructuring and central hole formation. Also some of the NSRR test rods were pre-irradiated under non-prototypical conditions in the JMTR² facility, inasmuch as they were irradiated in an unpressurized helium environment, and therefore not subjected to clad creep-down, oxidation and hydrogen embrittlement. The JMTR rods are therefore not included in table 4.1 and figure 4.1.

Finally, it should be mentioned that re-fabrication of full-length LWR fuel rods into short-length rodlets for testing in pulse reactors may modify the state of both fuel pellets and cladding. Firstly, the pellet-clad gap state is altered through fuel fragment relocation, when the rods are handled and manipulated. Unless the rodlets are pre-conditioned at normal operating power in the test reactor for a sufficiently long time to reach a new equilibrium pellet-clad contact state, PCMI under the subsequent power pulse will be aggravated by this relocation. A recent assessments of pulse reactor test data, made by the US NRC, indicate that fuel rods tested in the CABRI facility are sufficiently pre-conditioned before the pulse tests, whereas the rods tested in NSRR are not sufficiently pre-conditioned to reach an equilibrium pellet-clad contact state before the transient (NRC, 2004). Secondly, the cladding microstructure may be altered during the re-fabrication process, which usually involves heat input from cutting, welding and thermocouple attachment. Possible effects of these processes on clad properties have been identified and discussed by Garde (2000).

4.1.3 SPERT-CDC tests

The SPERT-CDC tests were conducted by Idaho Nuclear Corporation 1969-1970. The general objective of the tests was to obtain safety-related data on fuel rod behaviour during an RIA (MacDonald et al., 1980). The experimental program included un-irradiated test rods, as well as test rods pre-irradiated in the Engineering Test Reactor (ETR) to rod average burnups in the range of 1 to 33 MWdkg⁻¹U⁻¹. Here, we restrict our attention to pre-irradiated rods.

The SPERT experiments simulated the conditions of a BWR during cold startup. More specifically, the thermal-mechanical behaviour of single fuel rods or small clusters of rods under atmospheric pressure at 298 K, with no forced coolant flow and zero initial power, was investigated. The pulse widths were in the range of 13 to 31 ms. Each test rod contained a short, 132 mm fuel length, clad tube of 10% cold-worked Zircaloy-2. The UO₂ fuel pellets had a density of 0.94 TD (theoretical density) with the enrichment of 7 wt% ²³⁵U. Two different fuel rod designs were used: GEX-type with a cladding outer diameter of 7.94 mm and GEP-type with a diameter of 14.29 mm. The small-diameter GEX-rods were designed to increase the attainable energy deposition in the RIA simulation facility, and their clad wall thickness and fuel-cladding gap were reduced proportionally to the clad diameter.

The results from the SPERT-CDC tests are summarized in section A.1 of appendix A.

¹ Engineering Test Reactor

² Japanese Material Test Reactor

4.1.4 PBF tests

The PBF experiments simulated the hot startup conditions in a BWR, i.e. water temperature 286 °C and pressure 7.0 MPa, using individually shrouded fuel rods at relatively low burnups (MacDonald et al., 1980). In these tests, power excursions were initiated by a fast-acting drive system that moved the rods at a velocity of 9.5 ms⁻¹ through the test reactor core, corresponding to a reactivity insertion time of about 50 ms. This is well above the BWR maximum free-fall control rod velocity of about 6.0 ms⁻¹, and the reactivity insertion time is much shorter than that for a BWR, which is about 1.5 s.

Three series of tests were performed on irradiated PWR fuel rods (Meyer et al., 1997): the RIA 1-1, RIA 1-2 and RIA 1-4 tests. Tests RIA 1-1 and RIA 1-2 each contained four fuel rods, but the rods were in individual flow shrouds such that they behaved as single-rod tests. Test RIA 1-4 was a true multi-rod test with a 3×3 array of 9 fuel rods. The main objective of test RIA 1-4 was to investigate core coolability of clustered pre-irradiated rods for comparison with results of RIA 1-1 tests.

Section A.2 in appendix A summarizes test conditions and results for all rods in these tests. The test energies were relatively high in the PBF test series, because the program was designed to examine fuel behaviour near the 280 calg⁻¹ (1172 Jg⁻¹) fuel enthalpy core coolability limit. The ²³⁵U fuel enrichment for the test rods were 5.7 wt%.

4.1.5 NSRR tests

A large-scale RIA test program has been carried out at the Nuclear Safety Research Reactor (NSRR) by the Japan Atomic Energy Research Institute (JAERI). Ishikawa and Shiozawa (1980) have reviewed in detail the NSRR studies up to 1980, which were performed on fresh fuel rods. Ishikawa et al. (1989) have reviewed and evaluated the NSRR results up to 1989. In addition, there have been several more recent overviews by Fujishiro et al. (1992) and Fuketa et al. (1997 and 2001) on PWR data, and by Nakamura (1999) and Nakamura et al. (1994, 2000 and 2002a) on BWR data. Papers on both PWR and BWR tests have been presented by Fuketa (2000), Fuketa et al. (2000) and Nakamura et al. (2002b). Here, we only report the main results and conclusions from the NSRR tests.

The NSRR facility has a TRIGA-ACPR pool reactor, which generates significantly narrower power pulses than expected under RIA in LWRs. The reactor and reactivity control system yield pulses with full width at half maximum in the range of 4.4 to 7 ms. The RIA simulation tests on pre-irradiated fuel rods employ a test capsule containing stagnant water at atmospheric conditions. The instrumentation for recording the response of the test rod and coolant during the transient is also positioned within the test capsule.

The test rods used in the NSRR tests can be separated into three groups: (i) PWR test rods, (ii) BWR test rods, and (iii) the Japanese Material Test Reactor (JMTR) test rods. The first two groups of rods were pre-irradiated in commercial power plants and then re-fabricated into short-length test rodlets. The rodlets were re-fabricated by cutting 122 mm rod segments from full-length rods. They were back-filled with either pure helium or a mixture of xenon, krypton and helium to pressures ranging from 0.1 to 4.6 MPa in order to simulate the range of gas conditions representing end-of-life gas composition and pressure. The test rods that were pre-irradiated in JMTR were directly inserted into the test capsule after pre-test examinations. Below, we briefly discuss the base irradiation conditions and test rod characteristics for each group. A more detailed presentation is given in section A.3, appendix A.

The tests made on PWR fuel consist of six different series, fetched from six different power reactors. Two of the test series used 14×14 fuel and four of them used 17×17 fuel. The 14×14 rods were base irradiated in the Mihama (MH) reactor and the Genkai (GK) reactor to a rod average burnup of 39 and 42 MWdkg⁻¹U⁻¹, respectively. Concurrently, rods from Ohi 1 (HBO) and Ohi 2 (OI) were pre-irradiated to rod average burnups of 50 MWdkg⁻¹U⁻¹ and 39 MWdkg⁻¹U⁻¹, respectively. In a separate series, 17×17 fuel rods irradiated in Takahama III reactor (TK series) with low tin Zircaloy-4 clad material (1.3 wt% Sn) were subjected to RIA simulation tests. The latest tests on 17×17 fuel were performed on two rods, pre-irradiated in Ohi Unit 4 to 60 and 58 MWdkg⁻¹U⁻¹, respectively. The first rod, OI-10, had MDA cladding (Zr-0.8Sn-0.2Fe-0.1Cr-0.5Nb by wt%), whereas the other rod, OI-11, had ZIRLO (Zr-1.0Nb-0.1Fe by wt%) cladding. A summary of design data, test conditions and results for the PWR test rods is presented in section A.3.1, appendix A.

Two series of BWR rods, TS and FK, were tested in the NSRR. In the TS series, fuel rods from a 7×7 assembly were base irradiated in Tsuruga Unit 1 to a rod average burnup of about 22 MWdkg⁻¹U⁻¹. In the FK series, 8×8 rods were base irradiated in the Fukushima Daiichi unit 3 (FK 1-3 tests) or in the Fukushima Daichi Unit 2 (FK 4-5 and FK 6-12) to different levels of burnup. In the FK 1-3, tests the fuel burnup ranged from 41 to 45 MWdkg⁻¹U⁻¹, and in the FK 4-5 and FK 6-12 tests the burnups were 56 and 61 MWdkg⁻¹U⁻¹, respectively. A summary of design data, test conditions and results for the BWR test rods is given in section A.3.2, appendix A.

A total of 21 rods have been pre-irradiated in the Japanese Material Test Reactor (JMTR) to rod average burnups ranging from 13 to 38 MWdkg⁻¹U⁻¹ and then subjected to RIA simulation tests in the NSRR. The test rods were short 14×14 PWR type rods designed for testing in the NSRR. In section A.3.3, appendix A, we summarise the design data, test conditions and main results. The JMTR tests can be divided into three subgroups: JM series have standard 14×14 rod dimensions with UO₂ fuel of 10 wt% ²³⁵U enrichment, JMH series have 20 wt% ²³⁵U enrichment, and the JMN series have 10 wt% ²³⁵U enrichment with a narrow pellet-clad gap. Higher ²³⁵U pellet enrichments in JMTR rods compared to the concentrations used in PWRs allow for higher energy depositions during the tests. As discussed in section 3.2.2, the radial power distribution in the rod, which has an effect on fuel rod thermal–mechanical response during RIA, is affected by the non-prototypical ²³⁵U enrichments. The JMTR rods are therefore not typical of LWR fuel, and have not been included in table 4.1 and figure 4.1.

4.1.6 CABRI REP-Na tests

The main purpose of the CABRI REP-Na program was to study the validity of the RIA acceptance criteria on high-burnup 17×17 PWR fuel, with emphasis on the behaviour of fuel during the early stage of the transient up to fuel failure (Schmitz & Papin, 1999). A total of twelve tests have been conducted within the program. Eight of the tests were performed on UO₂ fuel and four tests on MOX fuel, pre-irradiated to burnups ranging from 28 to 65 MWdkg⁻¹U⁻¹.

In addition to the CABRI REP-Na program, two tests were performed in November 2002 on PWR fuel rods with burnups around 75 MWdkg⁻¹U⁻¹. These test rods, denoted CIPO-1 and CIPO-2, had ZIRLO and M5 cladding, respectively. Definite test results for these rods, which actually belong to a new test series in the CABRI facility, have not yet been published, and they are therefore not considered here.

The CABRI test reactor is a pool-type light water reactor, designed with a central flux area that can accommodate the insertion of a test device. The central flux area of the reactor contains a flowing sodium loop. The test rod is placed inside a test capsule, which also houses the in-reactor instrumentation used to monitor the fuel behaviour during the transient. The power transients are initiated from zero power, and pulse widths between 9.5 ms to 75 ms can be generated.

Although the coolant medium and pressure (0.46 MPa) are different from those in LWRs, the coolant conditions are considered as representative for studying the fuel rod response up to departure from nucleate boiling under an RIA in LWRs. Hence, the clad-to-coolant heat transfer is expected to be similar to that in LWRs during the first part of the transient. Moreover, the coolant and fuel cladding temperature in CABRI is 553 K at start of the transient, which is close to that of a PWR at hot stand-by.

Except for rod Na-2, all test rods in the CABRI REP-Na series were taken from 17×17 PWR fuel rods irradiated under nominal conditions in commercial PWRs, which were re-fabricated into short-length rodlets. Rod Na-2 was a test reactor rod, pre-irradiated in the BR3 test reactor, Belgium. The cladding material was standard Zircaloy-4, except for rods Na-3 and Na-9 with low-tin Zircaloy-4, and Na-11 with M5 cladding. The basic data on the rods and the main results of the tests are summarised in section A.4, appendix A.

4.2 Mechanical property tests

4.2.1 Introduction

The key mechanical property for clad tube survival under RIA is the clad ductility. Ductility of a material can be defined in many ways. In mechanical property tests, it is conventionally defined either by the total elongation of a test specimen under tension, or by the reduction of specimen cross-sectional area at failure. The former definition is more commonly applied than the latter, since total elongation can be more easily measured than area reduction. However, the total elongation under tension is unfortunately not a well-defined material property. As discussed in section 5.2.1, the experimentally measured total elongation is strongly affected by the size and geometry of the test specimen, and in some cases also by the loading conditions.

In the present work, we are concerned with clad tubes subjected to a biaxial tangential-axial stress state induced by pellet-clad mechanical interaction. The mechanical property of importance to clad failure under these conditions is the material's capacity to deform plastically in the tube hoop direction, or in other words; the hoop total elongation or hoop plastic strain at failure. Accordingly, the bulk of mechanical property data compiled in this section are total elongation data, defined from measured circumferential elongations in clad tube burst tests; i.e. in tests performed on closed-end tube samples loaded by an internal overpressure. The specimen geometry in these tests is thus identical to the clad tube geometry, and the loading conditions resemble those expected under RIA. This warrants the applicability of the data to RIA relevant conditions.

However, total elongation data from open-end burst tests and axial tension tests on clad tube specimens are also included in the compiled database. Although the loading conditions in these tests are not prototypical to RIA, they are abundant in literature, and therefore provide valuable additional information on the effects of e.g. irradiation and hydrogen content on clad ductility. The adaptation of these data to prototypical RIA conditions is not straightforward, and the methodology applied for this purpose is described in section 5.2.1.

Ductility data obtained from tests on non-tubular specimens, such as ring tensile tests or axial tensile tests on non-tubular samples, are not included in the database. There are several reasons for not including them: Firstly, due to the large impact of specimen geometry and size in total elongation measurements, data obtained from non-tubular samples are simply not appropriate for use in a criterion for clad tube failure under RIA (Bates et al., 2000). Secondly, total elongation data determined from ring tensile tests are inevitably ambiguous, since the loading conditions and sample gage length are not clearly defined in these tests. Thirdly, preparation of test specimens from irradiated clad tubes always involves an element of machining. For tubular samples, the machining is restricted to cutting the tube and removing the fuel pellets, which hardly affects the clad tube properties. For other kinds of samples, more extensive machining is needed, which may alter the material properties by local heating (Garde, 2000).

For example, the samples used in the first part of the French PROMETRA test program on irradiated Zircaloy-4 cladding were small-size spark machined, two-wing axial tensile specimens (Balourdet & Bernaudat, 1995). To allow spark machining, the clad oxide layer was first removed by grinding. It is unlikely that these processes could be performed without affecting the clad material. Moreover, as discussed in section 3.4.2, a brittle oxide layer has a direct embrittling effect on the clad tube, since it acts as nucleation site for radial cladding cracks. This effect is completely overlooked, when removing the oxide layer from the test specimens. Consequently, experimental data from neither the PROMETRA program, nor other test programs conducted on small-size machined specimens are used here.

Data from “expansion due to compression” (EDC) tests, recently performed on irradiated cladding at Studsvik (Grigoriev et al., 2002), are also not used here. Even though these tests are performed on tubular samples and very much resemble burst tests, they are difficult to evaluate, since the clad axial stresses under testing are unknown. However, the results of these tests can be used for qualitative comparisons of clad materials with respect to their ductility and survivability under RIA. This is further discussed in section 6.4.

The experimental data used in our derivation of a clad failure criterion comprise ductility measurements, which have been performed on two groups of clad materials:

- 1) Highly irradiated cladding, taken from fuel rods irradiated in commercial reactors and then thoroughly examined with respect to mechanical properties, oxide thickness, hydrogen content and hydride morphology.
- 2) Un-irradiated or moderately irradiated cladding, either in as-fabricated condition or charged with hydrogen under elevated temperature in a laboratory environment.

As discussed in section 3.4.4, the latter group of data is not necessarily typical of highly irradiated and in-reactor oxidized cladding, but it is still useful for studying the specific effects of hydrogen on clad ductility. The test matrix, i.e. the number of tests evaluated for each group of material, is given in table 4.2.

The following subsections give an overview of ductility tests on Zircaloy-2 and Zircaloy-4 materials, which form the experimental basis for the clad failure criterion. Test data are presented in detail in appendix B, and they are systematically explored and interpreted in section 5.2.2.

	Zircaloy-2	Zircaloy-4	Total
Irradiated samples	27	73	100
Un-irradiated samples	57	48	105
Total	84	121	

Table 4.2: Number of evaluated mechanical property tests on Zircaloy-2 and Zircaloy-4 clad samples in irradiated and un-irradiated state.

4.2.2 Zircaloy-2 material

Ductility data from a total number of 84 tests have been compiled for Zircaloy-2 cladding. The considered tests on irradiated Zircaloy-2 clad tubes are summarized in table 4.3, whereas table 4.4 specifies the considered tests on un-irradiated hydrogen charged Zircaloy-2 cladding. Except for dataset A, the data are taken from open literature. The database on Zircaloy-2 is described in detail in section B.1, appendix B.

Test series (Reference)	Test type	Temperature [K]	Hydrogen [wppm]	Strain rate [s ⁻¹]	Fluence ³ [10 ²⁵ m ⁻²]	Number of tests
NFD (Yasuda et al., 1987)	Axial tension	298 – 673	0 – 50	8.33x10 ⁻⁵	0.06 – 3.6	22
Dataset A	Open-end burst	295	28 – 400	1.0	0.8 – 6.5	5

Table 4.3: Tests on irradiated Zircaloy-2 clad tubes, which are included in the database for the clad failure criterion.

Test series (Reference)	Test type	Temperature [K]	Hydrogen [wppm]	Strain rate [s ⁻¹]	Number of tests
Dataset A	Open-end burst	295 – 623	12 – 1941	1.0	46
Studsvik (Pettersson et al., 1979) (Pettersson & Hellstrand, 1978)	Burst	563	< 15	2.0x10 ⁻⁴	6
NFD (Yasuda et al., 1987)	Axial tension	298 – 673	< 15	8.33x10 ⁻⁵	5

Table 4.4: Tests on un-irradiated Zircaloy-2 clad tubes, which are included in the database for the clad failure criterion.

³ Neutron fluence with $E \geq 1$ MeV.

4.2.3 Zircaloy-4 material

Ductility data from a total number of 121 tests have been compiled for Zircaloy-4 cladding. The considered tests on irradiated Zircaloy-4 clad tubes are summarized in table 4.5, whereas table 4.6 specifies the considered tests on un-irradiated hydrogen charged Zircaloy-4 cladding. Except for dataset B, the data are taken from open literature. The database on Zircaloy-4 is described in detail in section B.2, appendix B.

Test series (Reference)	Test type	Temperature [K]	Hydrogen [wppm]	Strain rate [s ⁻¹]	Fluence ⁴ [10 ²⁵ m ⁻²]	Number of tests
Dataset B	Burst	295 – 623	428 – 1691	5.0x10 ⁻⁵	8.0 – 9.8	17
ANO-2 ⁵ (Garde et al.,1996)	Burst	588	162 – 336	6.8x10 ⁻⁵	11	9
	Axial	313 – 673	130 – 360	2.8x10 ⁻⁴	11 – 12	13
CC-1 ⁶ (Garde et al.,1996)	Burst	588	207 – 731	6.8x10 ⁻⁵	12	8
	Axial	313 – 673	150 – 674	2.8x10 ⁻⁴	11 – 12	12
FC ⁷ (Garde,1989)	Burst	588	100 – 400	6.8x10 ⁻⁵	6.1 – 10	10
	Axial	298 – 673	350	4.2x10 ⁻⁴	10	4

Table 4.5: Tests on irradiated Zircaloy-4 clad tubes, which are included in the database for the clad failure criterion.

Test series (Reference)	Test type	Temperature [K]	Hydrogen [wppm]	Strain rate [s ⁻¹]	Number of tests
Dataset B	Burst	295 – 623	7 – 1145	1.0x10 ⁻⁴ - 2.8x10 ⁻⁴	26
JAERI (Fuketa et al., 2000)	Burst	298 – 620	8 – 1036	1.7x10 ⁻⁴ - 2.6x10 ⁻¹	20
FC (Garde, 1989)	Axial tension	298 – 673	< 15	4.2x10 ⁻⁴	2

Table 4.6: Tests on un-irradiated Zircaloy-4 clad tubes, which are included in the database for the clad failure criterion.

⁴ Neutron fluence with $E \geq 1$ MeV.

⁵ ANO-2: Arkansas Nuclear One – Unit 2.

⁶ CC-1: Calvert Cliffs – Unit 1.

⁷ FC: Fort Calhoun.

5 Clad failure criterion

This section deals with the derivation of a criterion for PCMI-induced clad tube failure under the early heat-up phase of RIA. The fundamental assumptions behind the criterion are defined in section 5.1, and the experimental database, upon which the criterion rests, is explored and interpreted in section 5.2. The failure criterion is then laid out in section 5.3, and uncertainties of the criterion are identified and quantified in section 5.4.

5.1 Bases for the clad failure criterion

As described in section 3.1, clad failure under the early heat-up phase of an RIA takes place through a presumed two-stage process in high-burnup fuel rods. The first stage involves radial propagation of flaws in the clad external oxide layer, or the brittle hydride-rich material beneath the oxide layer, into short through-wall defects, and the second stage is a matter of axial propagation of these defects into long axial cracks. The material property of interest for the first stage is the clad ductility in the hoop direction, i.e. the ability of the clad tube to expand radially without rupture. The material properties of interest for the second stage are the clad fracture toughness and tearing modulus, since they control the onset and possible arrest of axial crack propagation (Anderson, 1995).

Due to the two-stage nature of the failure process, it is not obvious how an occurrence of clad failure should be defined, when formulating and applying a failure criterion. For example, what is the necessary axial length of a clad perforation for the perforation to be counted as clad failure? In the work presented here, we make the fundamental definition that *clad failure corresponds to loss of clad tube integrity*. Failure is thus defined as penetration of the clad tube by the initial through-wall defect, and no attention is paid to the axial extension of the crack. This definition of clad failure is without doubt conservative, but it is judged to be appropriate for evaluations of acceptance criteria that are focused on retention of radioactive material.

In consistence with our definition of clad failure, the material property of interest in our study is the clad ductility. Consequently, the failure criterion defined in the sequel is based on a critical hoop plastic strain, or ductility limit, for the clad material. The critical hoop plastic strain is evaluated from the out-of-pile mechanical property tests in section 4.2, and formulated as a correlation with respect to clad temperature, fast neutron fluence and other key parameters. The proposed approach is not novel: Strain-based clad failure criteria are today used in Sweden and elsewhere for normal operation and anticipated transients (NUREG-0800, 1981), and a strain based criterion for clad failure under RIA has recently been advocated by Vitanza (2002).

An essential weakness with strain-based failure criteria is that the strain at failure is generally path-dependent. Hence, the strain at failure is not a true material property, but depends on the time history of mechanical loading and temperature up to the point of failure. This path-dependence makes strain-based failure criteria inappropriate for cases in which temperature and loading vary independently with respect to time. However, in our case, we consider the early heat-up phase of RIA, under which both the clad temperature and mechanical loading are monotonously increasing with time. Under such conditions, the use of strain-based failure criteria is justified.

5.2 Evaluation of mechanical property tests

The mechanical property tests in section 4.2 and appendix B constitute the experimental database, from which the clad failure criterion is derived. The clad ductility data in appendix B are obtained through various testing techniques, with significant differences in size and loading of the specimens. Consequently, the raw ductility data are not consistent between themselves, and neither can they be directly applied in a clad failure criterion for RIA, since the loading of the clad tube differs from that of the test samples. These differences must thus be accounted for, and the applied methodology for considering non-typicality in test conditions is described in section 5.2.1. After this adaptation of test data to prototypical RIA conditions, the experimental data are explored and key parameters for the clad ductility are identified in section 5.2.2.

5.2.1 Adaptation of ductility test data

The parameter of interest in our study is the critical hoop plastic strain, or total circumferential plastic elongation at failure, of clad tubes under biaxial tangential-axial loading, i.e. under a stress state characterized by $\sigma_{zz}/\sigma_{\theta\theta} = 1$. This parameter has to our knowledge been directly measured in only three experiments. Two of the experiments were performed on un-irradiated Zircaloy clad tubes at room temperature (Maki & Ooyama, 1975) and (Andersson & Wilson, 1979). The third experiment was made on Zr-1%Nb clad tubes in both un-irradiated and irradiated state, for temperatures between 300 and 723 K (Kaplar et al., 2001).

Consequently, the bulk of experimental data at hand are determined under test conditions that are more or less non-prototypical with respect to specimen geometry, size and loading conditions. The experimental data compiled in appendix B can be divided into three categories, as shown in table 5.1.

Category	$\sigma_{zz}/\sigma_{\theta\theta}$	Specimen gage length	Number of tests
1) Normal burst tests	$\frac{1}{2}$	Clad tube perimeter	96
2) Open-end burst tests	0	Clad tube perimeter	51
3) Axial tensile tests	∞	Various axial lengths	58

Table 5.1: Categories of test data used for determination of the clad failure criterion.

The loading conditions and geometry for category (1) are quite similar to the conditions expected under RIA, whereas category (3) contains the most non-prototypical test data. Due to the non-typical stress state, the measured total elongation (plastic strain to failure) in these tests cannot be directly interpreted as critical hoop plastic strain in evaluations of RIA. The measured total elongation, ε_{te} , is therefore converted to an equivalent critical hoop plastic strain, henceforth simply referred to as “failure strain”, ε_f , according to

$$\varepsilon_f = C_{Ri} \varepsilon_{te}. \quad (5.1)$$

Here, ε_f is the hoop plastic strain at failure, relevant to the geometry and stress state under RIA, i.e. to a clad tube subjected to biaxial loading. C_{Ri} is an empirically found reduction factor, < 1 , where index i refers to the data category 1, 2 or 3 in table 5.1. Hence, the reduction factor is specific to the category of data under consideration, as further described below. Finally, ε_{te} is the measured total elongation. For data in categories 1 and 2, ε_{te} is the *hoop* total elongation, whereas it corresponds to the measured *axial* total elongation for category 3.

5.2.1.1 Burst test data (C_{R1} and C_{R2})

The burst tests in categories 1 and 2 differ from true RIA conditions only with respect to the stress biaxiality ratio $\sigma_{zz}/\sigma_{\theta\theta}$; see table 5.1. The reduction factors C_{R1} and C_{R2} are determined from the results of two experiments, in which the influence of $\sigma_{zz}/\sigma_{\theta\theta}$ on the hoop total elongation was studied (Maki & Ooyama, 1975) and (Andersson & Wilson, 1979). Both studies were performed on un-irradiated cladding tubes at room temperature. The former study was on RXA Zircaloy-2 material⁸, and the latter on RXA Zircaloy-4. The results from these experiments are summarized in figure 5.1, which shows that the hoop total elongation is strongly influenced by the stress biaxiality ratio.

The reduction factors C_{R1} and C_{R2} are derived directly from the data in figure 5.1:

$$C_{R1} = \frac{\bar{\varepsilon}_{te}(\sigma_{zz}/\sigma_{\theta\theta} = 1)}{\bar{\varepsilon}_{te}(\sigma_{zz}/\sigma_{\theta\theta} = 1/2)} = \frac{10.77}{23.61} = 0.456, \quad (5.2)$$

$$C_{R2} = \frac{\bar{\varepsilon}_{te}(\sigma_{zz}/\sigma_{\theta\theta} = 1)}{\bar{\varepsilon}_{te}(\sigma_{zz}/\sigma_{\theta\theta} = 0)} = \frac{10.77}{52.00} = 0.207. \quad (5.3)$$

Here, $\bar{\varepsilon}_{te}$ alludes to the average value of hoop total elongation at a specific biaxiality ratio, evaluated from the data in (Maki & Ooyama, 1975) and (Andersson & Wilson, 1979). It should be noticed that these investigations were restricted to un-irradiated Zircaloy cladding at room temperature, and it is therefore interesting to compare the results with the study by Kaplar et al. (2001), who measured the total elongation of Zr-1%Nb cladding at two different stress states, $\sigma_{zz}/\sigma_{\theta\theta}=1$ and $\sigma_{zz}/\sigma_{\theta\theta}=1/2$, for both un-irradiated and irradiated material at temperatures between 300 and 723 K. For un-irradiated Zr-1%Nb at room temperature, the measured hoop total elongation was no less than 65% at $\sigma_{zz}/\sigma_{\theta\theta}=1/2$, and 18% at $\sigma_{zz}/\sigma_{\theta\theta}=1$.

⁸ Only materials B,C and D from the study are considered here.

A comparison with figure 5.1 reveals that these data are inconsistent with the hoop total elongation of RXA Zircaloy cladding. In particular, the data for un-irradiated Zr-1%Nb indicate that $C_{RI} \approx 18/65 \approx 0.27$, which is much different from the reduction factor determined from the tests on un-irradiated Zircaloy in eq. (5.2). Moreover, for irradiated Zr-1%Nb, Kaplar et al. (2001) found that the hoop total elongation was practically insensitive to the applied stress state, thus implying that the reduction factor C_{RI} should be close to unity for irradiated cladding.

In conclusion, the results of Kaplar et al. (2001) indicate that the use of $C_{RI}=0.456$ in evaluations of burst test data may lead to conservative estimates of the failure strain ϵ_f , when applied to irradiated samples, and to non-conservative estimates when applied to un-irradiated samples.

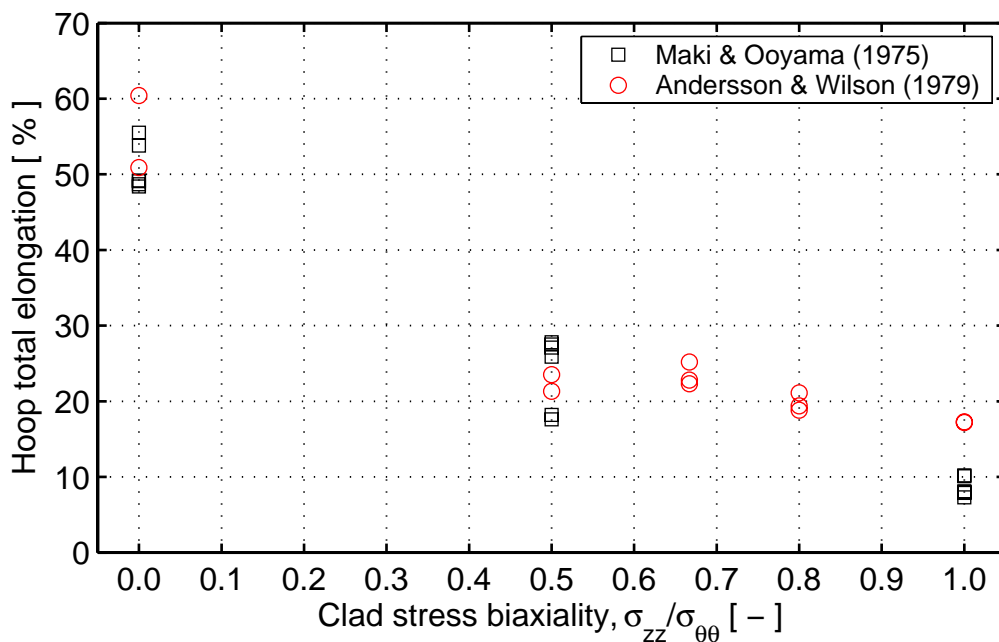


Figure 5.1: Influence of clad stress biaxiality on hoop total elongation. Data for un-irradiated Zircaloy RXA cladding at room temperature from (Maki & Ooyama, 1975) and (Andersson & Wilson, 1979).

5.2.1.2 Axial tensile test data (C_{R3})

The conversion of measured total elongation in the clad axial direction to an equivalent critical plastic strain in the hoop direction is not straightforward. As shown in table 5.1, not only the loading direction and stress state differ, but also the gage lengths used for calculating the total elongation from measured axial displacements. The gage length influences the total elongation results, which can be understood by recognizing that the total elongation of a test specimen is the sum of uniform elongation and localized deformation, usually referred to as necking. Hence, for a specimen with gage length L_o , the total elongation can be written

$$\epsilon_{ie} = \frac{\Delta L}{L_o} = \frac{\delta + \epsilon_{ue} L_o}{L_o} = \frac{\delta}{L_o} + \epsilon_{ue}. \quad (5.4)$$

In eq. (5.4), δ is the localized extension from necking. The uniform elongation, ε_{ue} , is a material property, which is independent of specimen geometry, but weakly affected by temperature and other test conditions. The necking, on the other hand, depends on specimen geometry as well as on material properties. Barba (1880), empirically found that δ is proportional to the linear dimensions of the cross-sectional area of the specimen, A_o . The relation

$$\delta = \beta \sqrt{A_o} \quad (5.5)$$

is therefore known as Barba's law. Here, β is a parameter related to the local ductility of the material, i.e. the ability of the material to deform plastically at the microscopic level. By combining eqs. (5.4) and (5.5), we have

$$\varepsilon_{te} = \beta \frac{\sqrt{A_o}}{L_o} + \varepsilon_{ue}, \quad (5.6)$$

from which it is evident that the total elongation depends on both gage length and cross-sectional area of the specimen. In axial tensile tests on clad tubular specimens, the cross-sectional area A_o is given by the clad tube dimensions, and therefore does not vary significantly between tests. However, the gage length L_o may vary considerably. In the axial tensile tests compiled in appendix B, it ranges from 50 to 76 mm. This variation is fortunately moderate, and we have not found it necessary to adjust the experimental data with respect to differences in L_o .

The reduction factor C_{R3} in eq. (5.1) is determined from the results of a study by Garde et al. (1996), in which both axial tensile tests and burst tests were performed on the same material. The material under study was Zircaloy-4, which had been irradiated to about 10^{26} m^{-2} ($E \geq 1 \text{ MeV}$) in the Calvert Cliffs Unit 1 (CC-1) and the Arkansas Nuclear One Unit 2 (ANO-2) PWR. The testing temperature was 573-588 K, and the gage length used in the axial tension tests on tubular specimens was 76 mm. The results from these tests, which are presented in detail in section B.2.4, appendix B, are summarized in figure 5.2, where the total elongation data have been plotted with respect to the clad wall radial average hydrogen concentration of each specimen. In these tests, the measured total elongation in the axial direction is evidently about twice as large as in the hoop direction, and the reduction factor C_{R3} is determined from eqs. (5.1) and (5.2)

$$C_{R3} = C_{R1} \frac{\bar{\varepsilon}_{te-burst}}{\bar{\varepsilon}_{te-axial}} = 0.456 \frac{2.741}{5.506} = 0.227, \quad (5.7)$$

where $\bar{\varepsilon}_{te-burst}$ and $\bar{\varepsilon}_{te-axial}$ are the average total elongations in the burst tests and axial tensile tests, respectively, determined from the data presented in figure 5.2. Hence, in determining C_{R3} , we have neglected any possible influence of hydrogen content and temperature on the reduction factor. This may be a simplistic assumption, considering the study performed by Yunchang and Koss (1985). They studied the impact of stress biaxiality on the ductility of hydrogen-charged Zircaloy-2 sheets at room temperature, and their results indicate that the reduction factor in eq. (5.7) most probably depends on hydrogen concentration. This can be understood from the interplay of loading direction and hydride orientation, which lends a direction dependency to the hydrogen embrittlement; see section 3.4.4.4.

Finally, figure 5.3 shows the failure strain, ϵ_f , i.e. the equivalent critical hoop plastic strain, relevant to RIA conditions, evaluated by applying eq. (5.1) to the data presented in figure 5.2. As evidenced by figure 5.3, the differences between axial and burst test results are effectively eliminated, but there are still significant differences between the CC-1 and ANO-2 data sets.

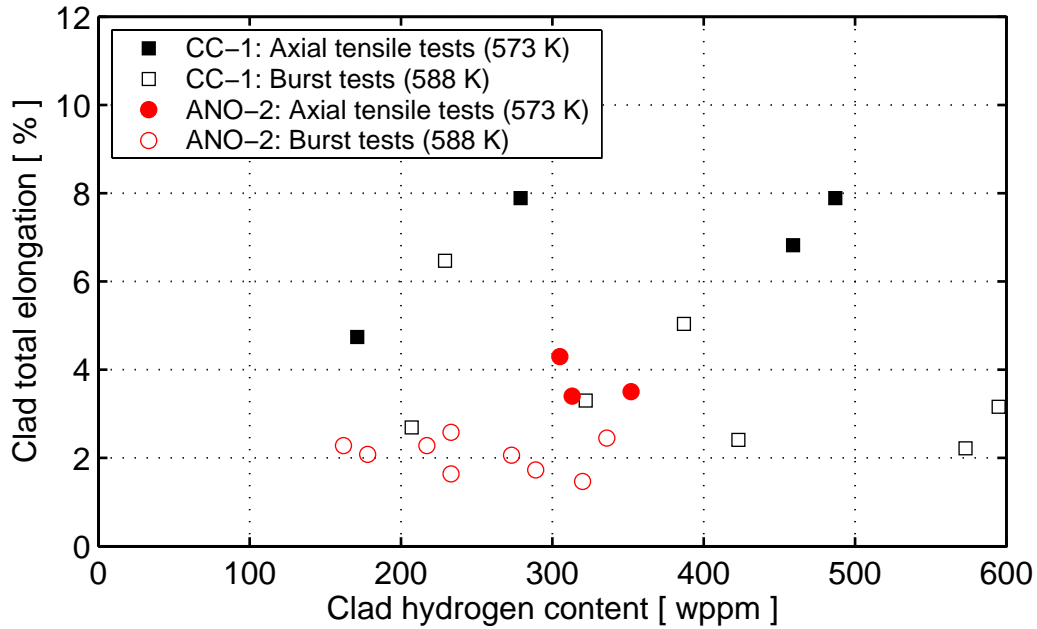


Figure 5.2: Comparison of total elongation data, obtained from axial tensile tests and burst tests on highly irradiated cladding tubes (Garde et al., 1996).

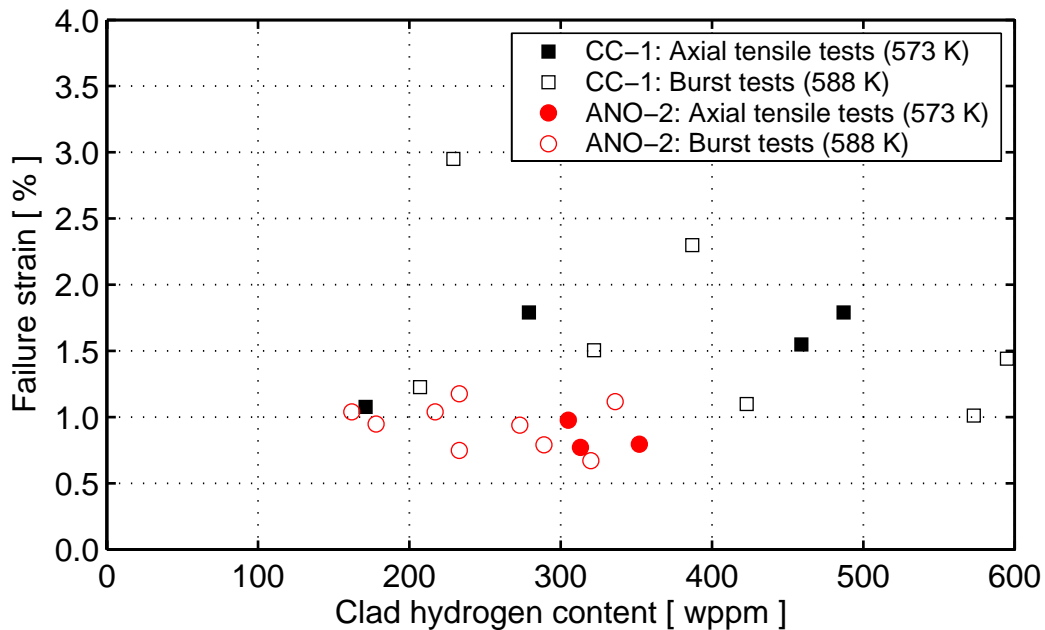


Figure 5.3: Results from conversion of the data in figure 5.2 to equivalent hoop plastic failure strain, ϵ_f , by use of eqs. (5.1), (5.2) and (5.7).

5.2.2 Exploration and interpretation of test data

By use of the methodology described in the foregoing section, the clad total elongation data from the mechanical property tests in appendix B can be readily transferred to an equivalent hoop plastic failure strain, ε_f . In this section, we make a systematic study of the thus determined failure strain, aiming at identifying key parameters for the clad ductility. Hence, the failure strain discussed below refers to ε_f in equation (5.1), i.e. to the equivalent hoop plastic failure strain, which is relevant to the stress state under RIA.

5.2.2.1 Influence of clad temperature

The influence of clad temperature on failure strain is shown in figure 5.4, which comprises failure strain data from un-irradiated material with low hydrogen content, determined in tests with low strain rates. More precisely, the average hydrogen content was below 15 wppm, and the strain rate was less than 10^{-3} s^{-1} for the presented data.

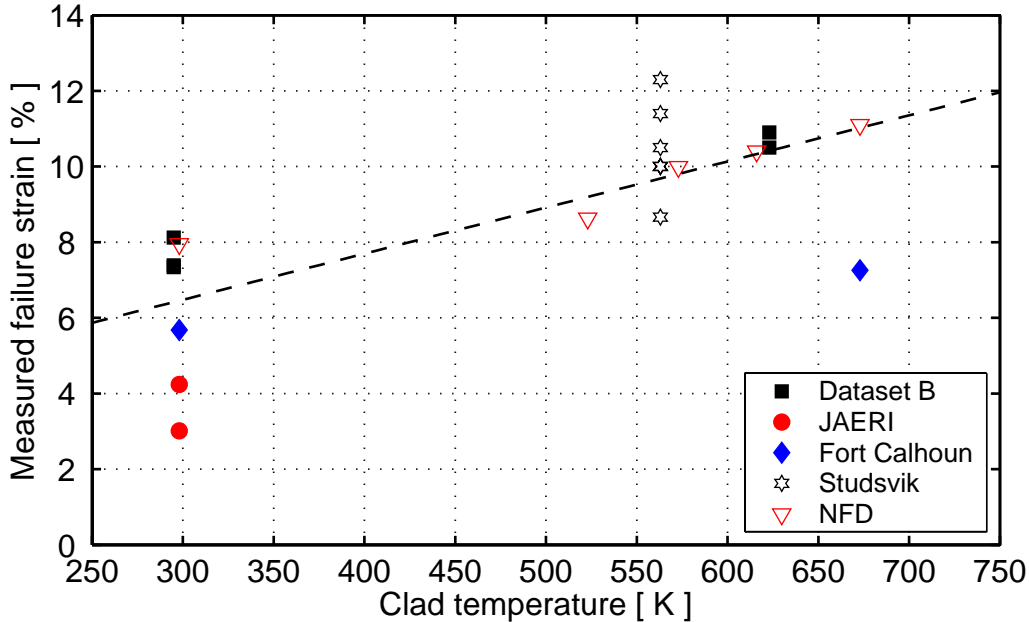


Figure 5.4: Clad failure strain vs. temperature for un-irradiated samples with negligible hydrogen content, tested at low strain rate. Filled symbols: Zircaloy-4. Open symbols: Zircaloy-2.

Clearly, the ductility increases with temperature, and a linear fit to the data is included in the figure. The regression line has the following equation

$$\varepsilon_{fo}(T) = 2.82 + 1.22 \cdot 10^{-2} T \quad [\%], \quad (5.8)$$

where T is the clad temperature in Kelvin.

It is interesting to note that the spread in data is significant, even for these un-irradiated samples, taken from clad tubes in as-fabricated condition. Moreover, the spread is just as large within individual test series, as it is between different series.

From the presented data, it is not possible to discern notable differences between Zircaloy-2 and Zircaloy-4. However, figure 5.4 indicates superior room-temperature ductility for Zircaloy-2. This is consistent with observations made, that RXA type materials are more ductile than SRA materials in un-irradiated state, see e.g. (Yagnik et al., 2004). This difference between RXA and SRA materials generally disappears after irradiation.

Finally, it should be noticed that the effect of temperature on the ductility of hydrided cladding is much more complex than for the almost hydride-free cladding shown in figure 5.4. This is further discussed in subsection 5.2.2.4 below.

5.2.2.2 Influence of strain rate

In figure 5.5, we have added results of tests performed under high strain rate to the data presented in figure 5.4. Hence, also in this case, we restrict our attention to un-irradiated clad material with less than 15 wppm hydrogen.

As expected, the figure shows that the ductility decreases with increasing strain rate. At a strain rate of 1 s^{-1} , the failure strain is below 2%, irrespective of clad temperature. Although the failure strain is higher in the high-temperature tests, the high- and low-temperature data follow the same trend with respect to strain rate. Hence, we may conclude that the embrittling effect of increased strain rate is not significantly influenced by temperature, as long as un-irradiated cladding with negligible hydrogen content is concerned. However, as will be shown in subsection 5.2.2.4 below, this conclusion is not valid for hydrided material.

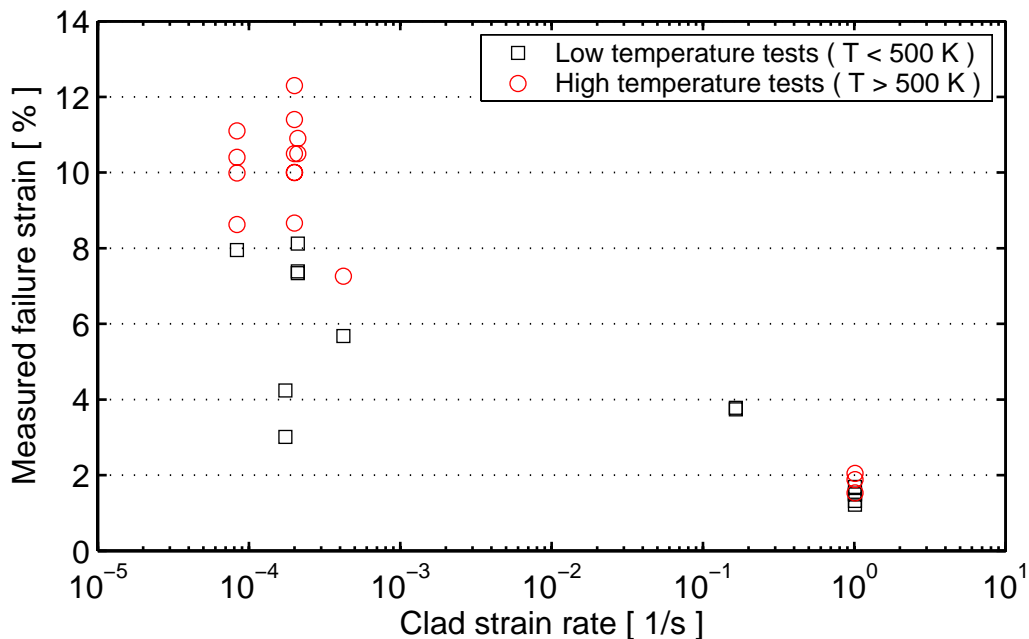


Figure 5.5: Clad failure strain vs. hoop strain rate for un-irradiated material with negligible hydrogen content (<15 wppm).

5.2.2.3 Influence of irradiation

Next, we study the influence of irradiation on the clad failure strain by comparing data from tests on un-irradiated and irradiated material. The comparison is shown in figure 5.6. All data are taken from tests at low strain rate ($<10^{-3} \text{ s}^{-1}$), and the data for irradiated material refer to samples with low hydrogen content. Accordingly, the embrittling effects of elevated strain rate and hydrogen are negligible for the data presented here. The fast neutron fluence for the irradiated material ranged from 6×10^{23} to $1.2 \times 10^{26} \text{ m}^{-2}$ ($E \geq 1 \text{ MeV}$). At these fluences, the irradiation-induced embrittlement is believed to be saturated; see section 3.4.1.

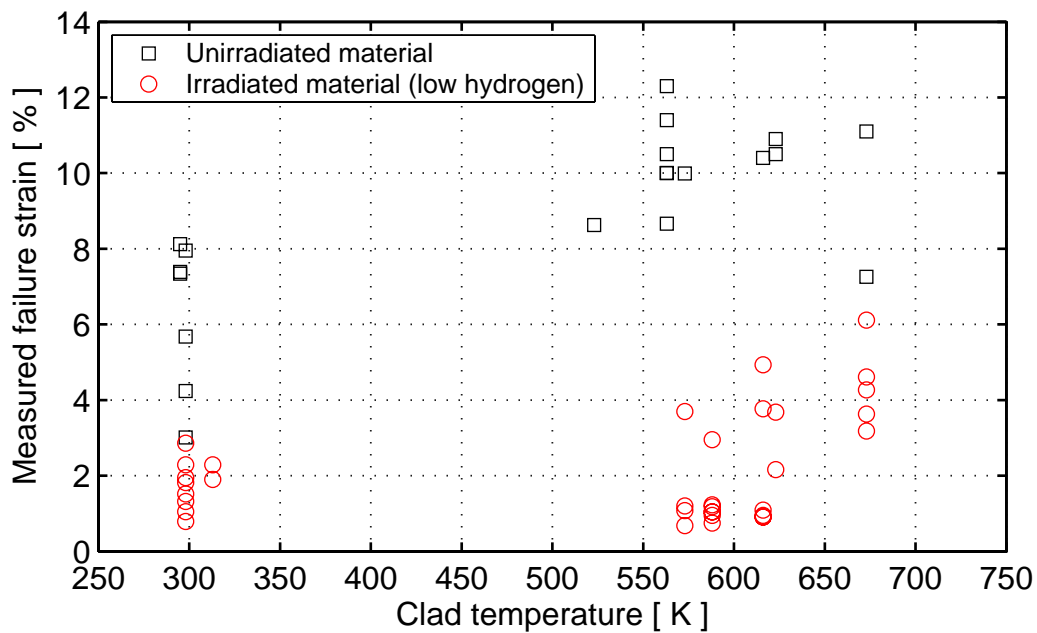


Figure 5.6: Clad failure strain vs. temperature for un-irradiated and irradiated materials. All tests were conducted at low strain rate ($<10^{-3} \text{ s}^{-1}$).

Clearly, the irradiated material has a typical failure strain of about 2%, which is significantly lower than for un-irradiated material. However, for the highest temperature covered by the data (673 K), the irradiated material shows a significantly higher ductility. This is probably due to thermal annealing of irradiation damage, which at 673 K is believed to be sufficiently fast to take place under testing of the material (Torimaru et al., 1996). However, it is not clear to what extent annealing will contribute to recovery of ductility under RIA, where the hold time at elevated temperature is much shorter. This issue is further discussed in section 5.3.3.

5.2.2.4 Influence of hydrogen

The influence of hydrogen on clad ductility is a complex matter, which is much more difficult to characterize than the effects of irradiation damage or strain rate. As described in section 3.4.4, the embrittling effect of hydrogen is strongly affected by temperature, and there is a ductile-to-brittle transition for the hydrided material at a certain temperature.

As shown in figure 3.5, section 3.4.4.2, the ductile-to-brittle transition depends on three parameters: hydrogen concentration, temperature and strain rate. The interdependence of these parameters is clearly observable in the failure strain data for un-irradiated, hydrogen charged cladding in appendix B. Figures 5.7 and 5.8 show the measured failure strain with respect to clad average hydrogen content at room temperature and high (523-673 K) temperature, respectively. In the figures, distinction is made between data from low ($<10^{-3} \text{ s}^{-1}$) and high ($>10^{-1} \text{ s}^{-1}$) strain rate tests.

From figure 5.7, it is clear that the combination of low temperature and high strain rate is extremely detrimental to clad ductility; the failure strain falls off by roughly two orders of magnitude as the hydrogen content exceeds 500 wppm. At low strain rate, the embrittling effect of hydrogen is somewhat milder, but still, the plastic failure strain is reduced to less than 1% in the hydrided material.

The embrittling effect of hydrogen is much less pronounced at elevated temperature. As shown in figure 5.8, the failure strain in tests performed at low strain rate and temperatures between 523 and 673 K is only weakly affected by clad hydrogen content. Unfortunately, the database does not comprise high strain rate tests on severely hydrided material, so it is not possible to tell if the same trend applies also to high strain rates.

A comparison between figures 5.7 and 5.8 clearly shows that there is a ductile-to-brittle transition temperature (DBT) for hydrided cladding, and that the DBT is to be found in the range 300 to 520 K. As already mentioned in section 3.4.4.2, this makes a BWR RIA at CZP more deleterious to clad integrity than at HZP.

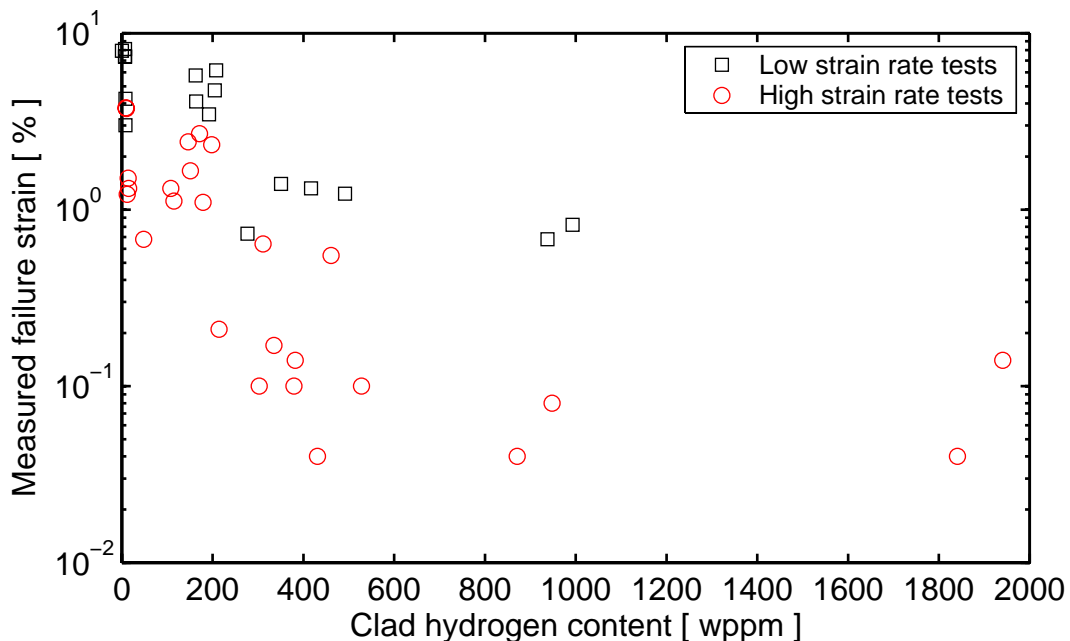


Figure 5.7: Clad failure strain vs. hydrogen content, determined from tests on un-irradiated material at room temperature. Data from low ($<10^{-3} \text{ s}^{-1}$) and high ($>10^{-1} \text{ s}^{-1}$) hoop strain rate tests are shown separately.

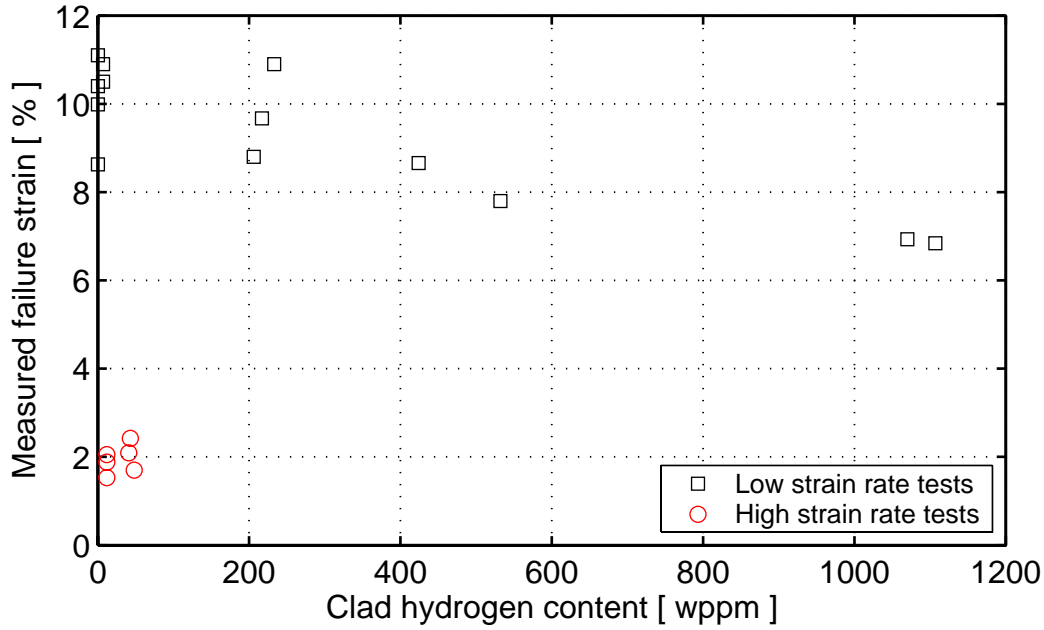


Figure 5.8: Clad failure strain vs. hydrogen content, determined from tests on unirradiated material at temperatures between 523 and 673 K. Data from low ($<10^{-3} \text{ s}^{-1}$) and high ($>10^{-1} \text{ s}^{-1}$) hoop strain rate tests are shown separately.

5.3 Proposed clad failure criterion

In the sequel, the clad failure criterion is formulated in the form of a correlation for hoop critical plastic strain, expressed in terms of the key parameters that were identified in the preceding section. Following the discussion in section 5.1, we simply postulate that a clad tube fails when

$$\varepsilon_{\theta\theta}^p \geq \varepsilon_f(T, \dot{\varepsilon}, c_H, \phi). \quad (5.9)$$

Here, $\varepsilon_{\theta\theta}^p$ is the clad hoop plastic strain and ε_f is the hoop failure strain, i.e. the hoop plastic strain at failure. As shown in section 5.2.2, the failure strain depends on clad temperature, T , strain rate, $\dot{\varepsilon}$, hydrogen content, c_H , and fast neutron fluence, ϕ . These parameters, together with the clad hoop plastic strain, are calculated by most fuel performance codes intended for transient analyses, and the failure criterion in eq. (5.9) can therefore easily be applied in analyses of RIA. The criterion should be checked in each time step of an analysis.

Following the discussion in section 5.1, the clad failure criterion in eq. (5.9) is restricted to the heat-up phase of RIA, and we therefore add the following supplementary condition to eq. (5.9)

$$\dot{T} > 0. \quad (5.10)$$

Hence, clad failure takes place if both eq. (5.9) and (5.10) are satisfied. All properties in these two equations are defined as radial average values in a certain axial cross section of the clad tube, and the criterion should be applied in each axial node of a fuel rod.

The failure strain ε_f on the right-hand side of eq. (5.9) is a best-estimate correlation with experimental data. Based on the analysis of these data in section 5.2.2, we write the correlation as

$$\varepsilon_f(T, \dot{\varepsilon}, c_H, \phi) = \varepsilon_{fo}(T) \cdot F(T, \dot{\varepsilon}, c_H, \phi), \quad (5.11)$$

where ε_{fo} is the failure strain of un-irradiated material at low strain rate, defined by eq. (5.8), and F is a ductility reduction factor. This factor is equal to unity for un-irradiated material at low strain rate, and falls off with increasing strain rate and as a result of irradiation- and hydrogen-induced clad embrittlement. The mathematical form of F is determined by making a best possible fit of the calculated failure strain in eq. (5.11) with experimental data. The “best possible fit” is found by minimizing the Euclidian norm of the relative errors, defined by the cost function

$$\Gamma = \sqrt{\sum_{i=1}^N \left| 2 \frac{\varepsilon_f^i - \varepsilon_m^i}{\varepsilon_f^i + \varepsilon_m^i} \right|^2}, \quad (5.12)$$

where ε_f^i and ε_m^i are the calculated and measured failure strains for the i :th test, and N is the number of tests. The cost function in eq. (5.12) is used in all fitting procedures described below. The minimization of Γ is performed by use of a standard Nelder-Mead Simplex algorithm, included in the MATLAB mathematical software (MATLAB, 2000). MATLAB is used throughout the data-fitting procedure, and also for visualization of the results.

As discussed in section 3.4, clad embrittlement is generally caused by several interacting phenomena, and the mathematical form of the ductility reduction factor F is therefore not easily determined. Here, we pursue the course from section 5.2.2, and start by characterizing the embrittling effects of elevated strain rate, hydrogen and irradiation damage separately. Thereafter, we merge the obtained results from these separate effect studies into a single correlation for the ductility reduction factor F .

As a first step, we therefore use the experimental data to determine ductility reduction factors, f_1 , f_2 and f_3 , for the following separate effects:

- f_1 : Ductility reduction factor, related to elevated strain rate.
Determined from tests on un-irradiated cladding with less than 15 wppm hydrogen.
- f_2 : Ductility reduction factor, related to hydrogen-induced embrittlement.
Determined from tests on un-irradiated, hydrogen charged cladding.
- f_3 : Ductility reduction factor, related to irradiation-induced embrittlement.
Determined from tests on irradiated cladding.

These separate-effect ductility reduction factors range from 0 to 1, and they are monotonously decreasing functions of strain rate, hydrogen content and fast neutron fluence, respectively.

They are related to the ductility reduction factor in eq. (5.11) by

$$\frac{1}{F} = \frac{1}{3} \left(\frac{1}{f_1} + \frac{1}{f_2} + \frac{1}{f_3} \right), \quad (5.13)$$

which inserted into eq. (5.11) yields

$$\varepsilon_f = 3 \frac{f_1 \cdot f_2 \cdot f_3}{f_1 \cdot f_2 + f_1 \cdot f_3 + f_2 \cdot f_3} \varepsilon_{fo}. \quad (5.14)$$

Equation (5.13) is a purely empirical relation, which defines the interaction between embrittling effects due to elevated strain rate, hydrogen and irradiation. From eq. (5.14), we find that $\varepsilon_f = \varepsilon_{fo}$ when $f_1 = f_2 = f_3 = 1$, i.e. when embrittling effects are absent. Otherwise, $\varepsilon_f \approx \min(f_1, f_2, f_3) \varepsilon_{fo}$, which means that the clad ductility is limited by the most severe of the aforementioned embrittling effects.

5.3.1 Effect of elevated strain rate

The ductility reduction factor f_1 is determined by fitting eq. (5.14) to failure strain data from tests on un-irradiated cladding with negligible hydrogen content. Since $f_2 = f_3 = 1$ in these tests, eq. (5.14) simplifies to

$$\varepsilon_f(T, \dot{\varepsilon}) = 3 \frac{f_1(\dot{\varepsilon})}{1 + 2f_1(\dot{\varepsilon})} \varepsilon_{fo}(T). \quad (5.15)$$

Here, ε_{fo} is defined by eq. (5.8), and an expression for f_1 can therefore be found by fitting eq. (5.15) to the failure strain data shown in figure 5.5 of section 5.2.2.2. The fit is made by minimizing the cost function defined by eq. (5.12), which yields

$$f_1(\dot{\varepsilon}) = \begin{cases} 0.046 - 0.31 \log_{10} \dot{\varepsilon} & \dot{\varepsilon} \leq 1 \text{ s}^{-1} \\ 0.046 & \dot{\varepsilon} > 1 \text{ s}^{-1} \end{cases}. \quad (5.16)$$

Here, the clad hoop strain rate $\dot{\varepsilon}$ is in units of s^{-1} . Figure 5.9 shows a comparison of failure strains, calculated by eqs. (5.15) and (5.16), with experimental data from which the expression for f_1 was derived. The data cover strain rates from 1.7×10^{-4} to 1.0 s^{-1} , and temperatures from 295 to 673 K.

5.3.2 Effect of hydrogen

The ductility reduction factor f_2 is determined by fitting eq. (5.14) to failure strain data from tests on un-irradiated, hydrogen charged cladding. Since $f_3 = 1$ for un-irradiated material, eq. (5.14) simplifies in this case to

$$\varepsilon_f(T, \dot{\varepsilon}, c_H) = 3 \frac{f_1(\dot{\varepsilon}) f_2}{f_1(\dot{\varepsilon}) f_2 + f_1(\dot{\varepsilon}) + f_2} \varepsilon_{fo}(T). \quad (5.17)$$

Here, ε_{f0} and f_1 are defined by eqs. (5.8) and (5.16), respectively, and an expression for f_2 can therefore be found by fitting eq. (5.17) to the failure strain data from tests on hydrogen charged cladding. For the time being, we do not include samples with artificially induced hydride rims or samples with extremely high fractions of radial hydrides in this fitting procedure. These samples will be considered in section 6.3.

The ductility reduction factor f_2 is dependent on clad hydrogen content, temperature and strain rate. It can be described by

$$f_2(c_H, T, \dot{\varepsilon}) = 0.01 + 0.99 e^{-\gamma(T, \dot{\varepsilon}) c_{HEx}}, \quad (5.18)$$

where c_{HEx} is the clad excess hydrogen content in wppm, i.e. the amount of hydrogen in excess of the terminal solid solubility, c_{TSS} :

$$c_{HEx} = \max(0, c_H - c_{TSS}). \quad (5.19)$$

Here, c_{TSS} is calculated through eq. (3.1), and c_H is the clad total hydrogen content in wppm. The coefficient γ in eq. (5.18) is correlated to temperature and strain rate through

$$\gamma(T, \dot{\varepsilon}) = 6.52 \cdot 10^{-4} + 2.21 \cdot 10^{-3} (6 + \log_{10} \dot{\varepsilon}) \left(1 - \tanh\left(\frac{T - 298}{8.5}\right) \right). \quad (5.20)$$

Here, T is in Kelvin and the hoop strain rate $\dot{\varepsilon}$ is in units of s^{-1} .

Figure 5.10 shows a comparison of failure strains, calculated by eqs. (5.17) – (5.20), with experimental data from which the expressions for f_2 were determined. The data cover strain rates from 1.7×10^{-4} to $1.0 s^{-1}$, temperatures from 295 to 673 K, and clad hydrogen contents up to 1941 wppm.

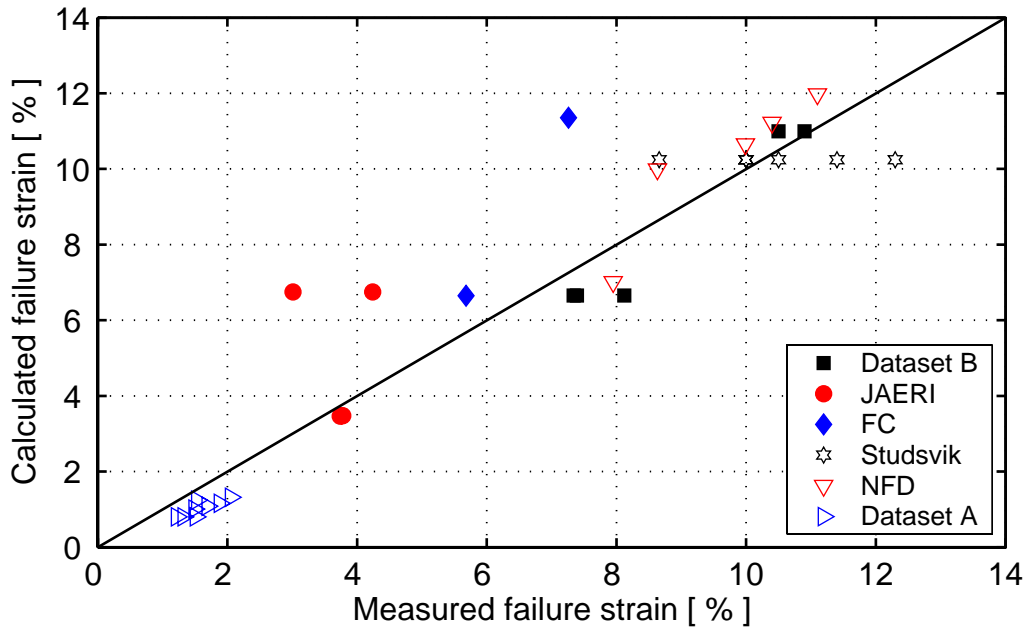


Figure 5.9: Calculated vs. measured clad failure strain for un-irradiated material with negligible hydrogen content (<15 wppm). Filled symbols: Zircaloy-4. Open symbols: Zircaloy-2. The tests alluded to in the legend are defined in section 4.2.

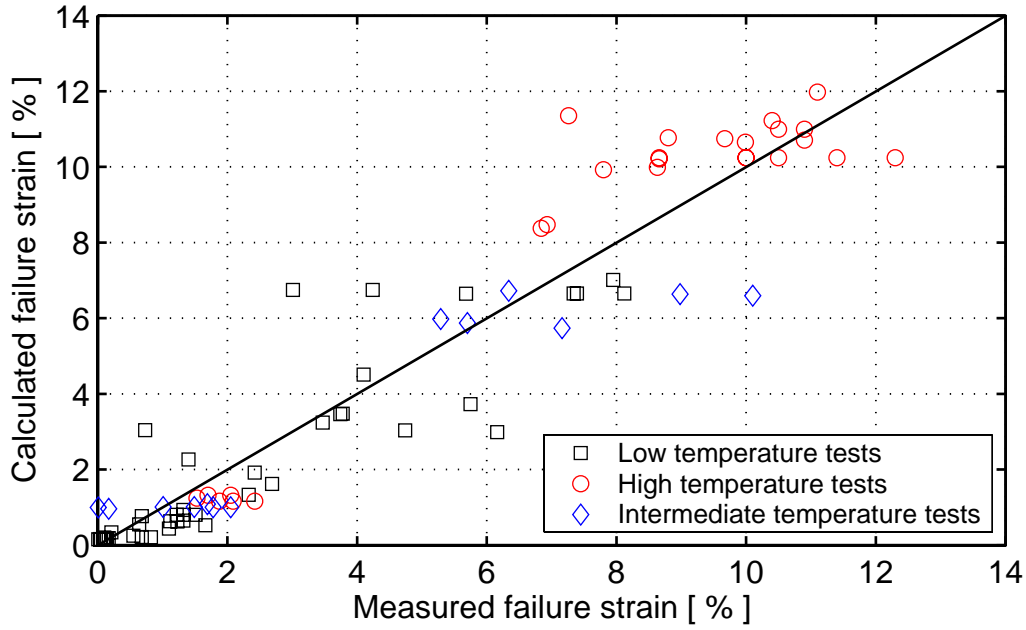


Figure 5.10: Calculated vs. measured clad failure strain for un-irradiated, hydrogen charged material. Low temperature: 295-298 K, High temperature: 523-673 K, Intermediate temperature: 373-473 K.

5.3.3 Effect of irradiation

Once f_1 and f_2 have been determined from tests on un-irradiated samples, the last ductility reduction factor, f_3 , can be determined from tests performed on irradiated samples. By using the known expressions for f_1 and f_2 , we find a correlation for f_3 by fitting eq. (5.14) to the failure strain data from tests on irradiated cladding. In this fitting procedure, we temporarily exclude samples with spalled oxide layer. These samples will be considered in section 6.3.

From failure strain data on all irradiated samples with non-spalled oxide layer, we find a first approximation to f_3

$$f_3(\phi) = 0.05 + 0.95 e^{-2.89 \cdot 10^{-24} \phi}, \quad (5.21)$$

where ϕ is the fast ($E \geq 1 \text{ MeV}$) neutron fluence in m^{-2} . Figure 5.11 shows the measured failure strains for all irradiated samples with non-spalled oxide layer, compared with their calculated counterparts.

As evidenced by figure 5.11, there are a number of tests, particularly those performed by NFD, in which the failure strain is significantly underestimated. A closer analysis of these cases reveals that the tests were performed at high temperature, either at 623 or 673 K. The unusually high measured failure strains in these tests are therefore probably a result of thermal annealing of irradiation damage. As shown by the data exploration in section 5.2.2.3, irradiation-induced embrittlement can be partly recovered by thermal annealing, provided that the cladding is held at elevated temperature for a sufficiently long period. This recovery is not considered in equation (5.21), which therefore underestimates the failure strain.

Figure 5.12 shows a comparison between calculated and measured failure strains, in which all the tests performed at high temperature, i.e. at 623-673 K, are excluded. As evidenced by the figure, the agreement between calculated and measured failure strain is fairly good for this data set.

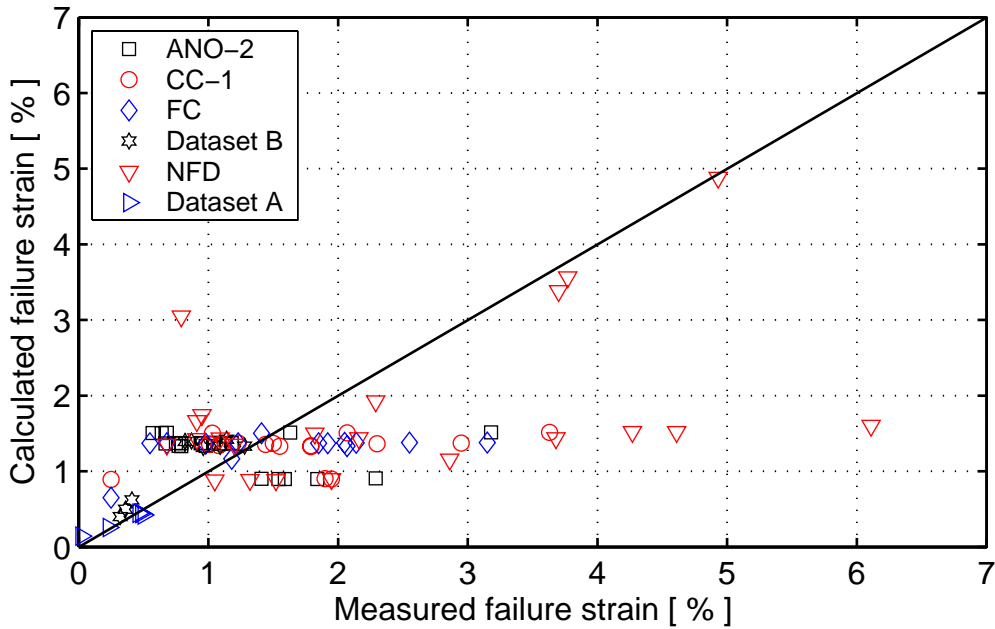


Figure 5.11: Calculated vs. measured clad failure strain for all tests on irradiated samples with non-spalled oxide layer. The irradiation-induced embrittlement is considered by use of eq. (5.21).

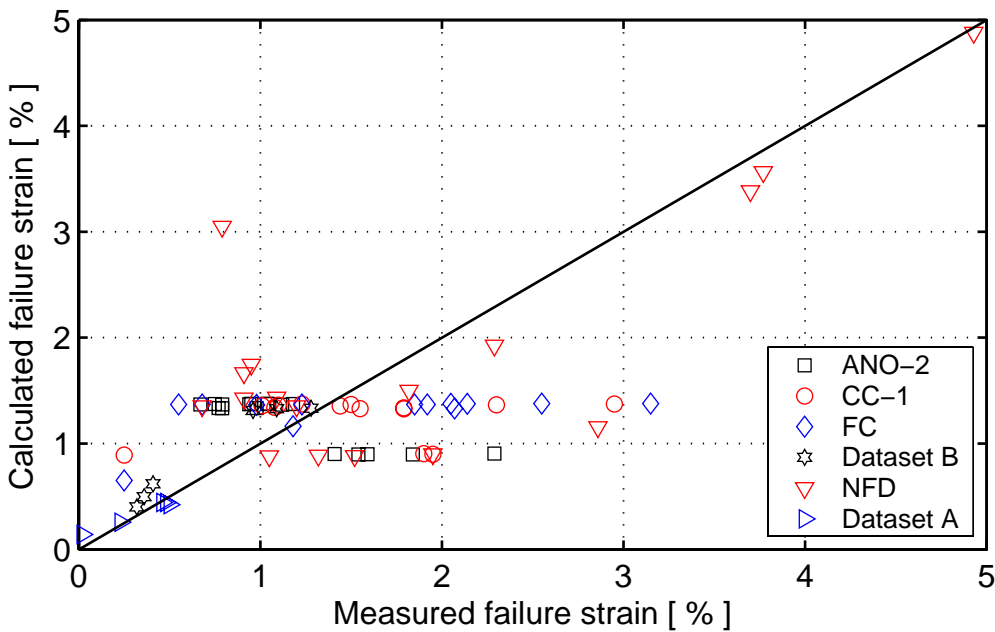


Figure 5.12: Calculated vs. measured clad failure strain for irradiated samples with non-spalled oxide layer, tested at temperatures below 623 K.

Unfortunately, information on the hold time at elevated temperature is not available for any of the tests considered here, and it is therefore impossible to consider the effect of thermal annealing on the test results. However, this effect has been studied in other experiments, the results of which can be used to improve eq. (5.21). Consequently, we make use of the work by Torimaru et al. (1996), and introduce in eq. (5.21) a dimension-free parameter, α , related to thermal annealing of irradiation damage

$$f_3(T, \phi) = \alpha(T) + (1 - \alpha(T)) e^{-2.89 \cdot 10^{-24} \phi} . \quad (5.22)$$

In accordance with eq. (5.21), the annealing parameter α is taken as 0.05 at beginning of the transient, but is then allowed to increase with temperature and time. In case α reaches unity, the irradiation damage is completely annealed out. The evolution of α is calculated from a correlation, which is entirely based on the work of Torimaru et al. (1996)

$$\alpha = \frac{1.12 \cdot 10^{11} (1 - \alpha) e^{-2.09 \cdot 10^5 / RT}}{\ln(0.95) - \ln(1 - \alpha)} \text{ [s}^{-1} \text{] ,} \quad (5.23)$$

where $R=8.3143 \text{ Jmol}^{-1}\text{K}^{-1}$ is the universal gas constant and T is in Kelvin.

Figure 5.13 shows the evolution of α , calculated through eq. (5.23), under isothermal conditions. The evolution is shown for three different temperatures. From these results, we may conclude that thermal annealing of irradiation damage is negligible under the early heat-up phase of an RIA, but that the phenomenon may improve clad ductility under the post-DNB or post-dryout phase of the transient. Since we restrict our analyses to the early heat-up phase, f_3 can be calculated from eq. (5.21).

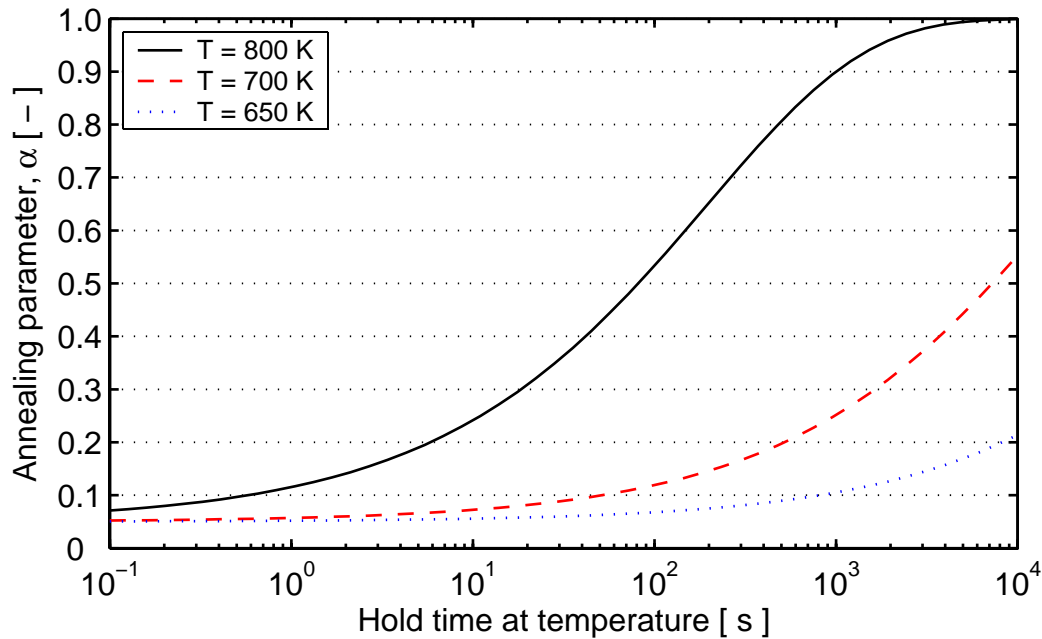


Figure 5.13: Evolution of parameter α under isothermal conditions. The parameter defines the extent of thermal annealing of irradiation damage.

5.4 Uncertainties of the clad failure criterion

Calculated failure strains from the proposed failure criterion are directly compared with results from mechanical property tests in section 5.4.1 below, and general uncertainties of the failure strain criterion are analysed and quantified. Section 5.4.2 contains a sensitivity study, in which the relative differences between calculated and measured failure strains are analysed with respect to the key parameters temperature, strain rate, hydrogen content and fast neutron fluence. The purpose of this study is to reveal systematic errors in the correlation for clad failure strain.

5.4.1 Direct comparison with mechanical property tests

Figure 5.14 shows measured failure strain data from mechanical property tests, in comparison with their calculated counterparts. The calculated failure strains are obtained by applying eq. (5.14) and the correlations for ϵ_{fo} , f_1 , f_2 and f_3 to the test conditions. These conditions, together with measured failure strains, are given in appendix B. It should be noticed that the hold time at elevated temperature under the tests is unknown, and the possible effects of thermal annealing of irradiation damage cannot be considered in calculations. Hence, eq. (5.21) is used for calculating the ductility reduction factor f_3 , rather than the full expressions in eqs. (5.22) and (5.23).

The measured data presented in figure 5.14 comprise 173 points, and constitute the database from which the failure strain correlation in section 5.3 is formulated. As mentioned in section 4.2, the entire database of mechanical property tests comprises 205 tests. Hence, 32 of these tests have been excluded when formulating the failure criterion. These are:

- Tests on irradiated clad tubes with spalled oxide layer and non-uniform hydride distribution (11 samples).
- Tests on un-irradiated hydrogen charged specimens with purposely introduced hydride rims or radial hydrides (21 samples).

The reason for excluding these samples when determining the failure strain correlation is that the correlation is formulated solely in terms of clad *average* hydrogen content, which is readily calculated through metal-water reaction models in most fuel performance codes. In order to accurately predict clad failure in spalled samples or samples with hydride rim, we need detailed information on the *local* hydrogen content at spalled regions or in the rim. This information is simply not provided by current fuel performance codes, and it is therefore not possible to capture the failure behaviour of cladding tubes with highly non-uniform hydrogen distributions, unless the required information can be obtained elsewhere.

Moreover, some of the un-irradiated samples with purposely introduced hydride rims are not typical of in-reactor oxidized and hydrided cladding. In some of these samples, the radial gradient in hydride concentration is unrealistically steep, and in other samples, there is a hydride rim not only at the clad outer surface, but also at the inner surface.

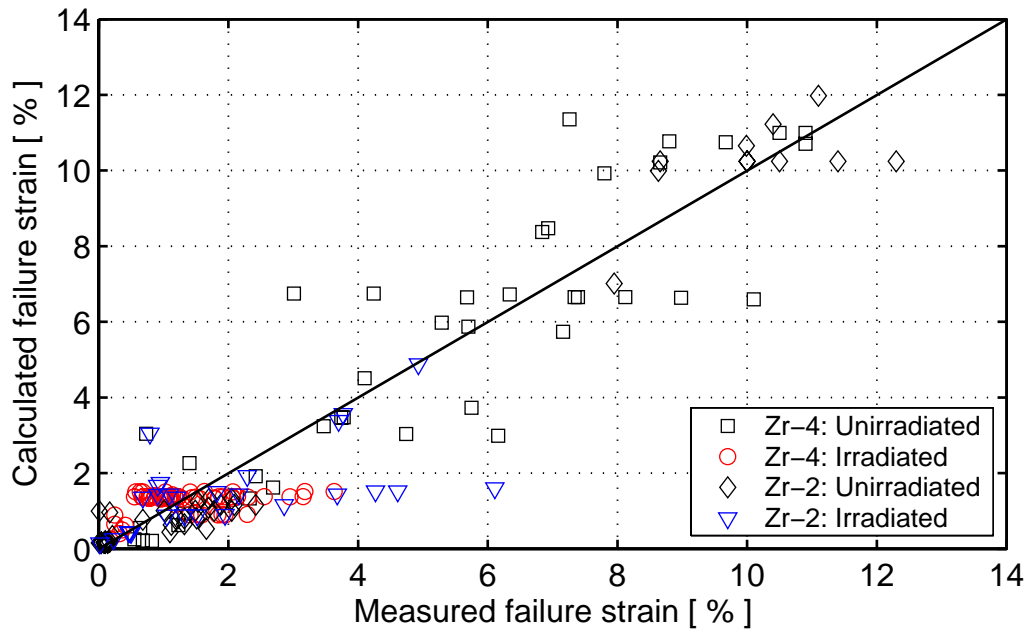


Figure 5.14: Calculated vs. measured failure strain for the database used for formulation of the failure criterion (173 points). A close-up of the low-strain region is shown in figure 5.15.

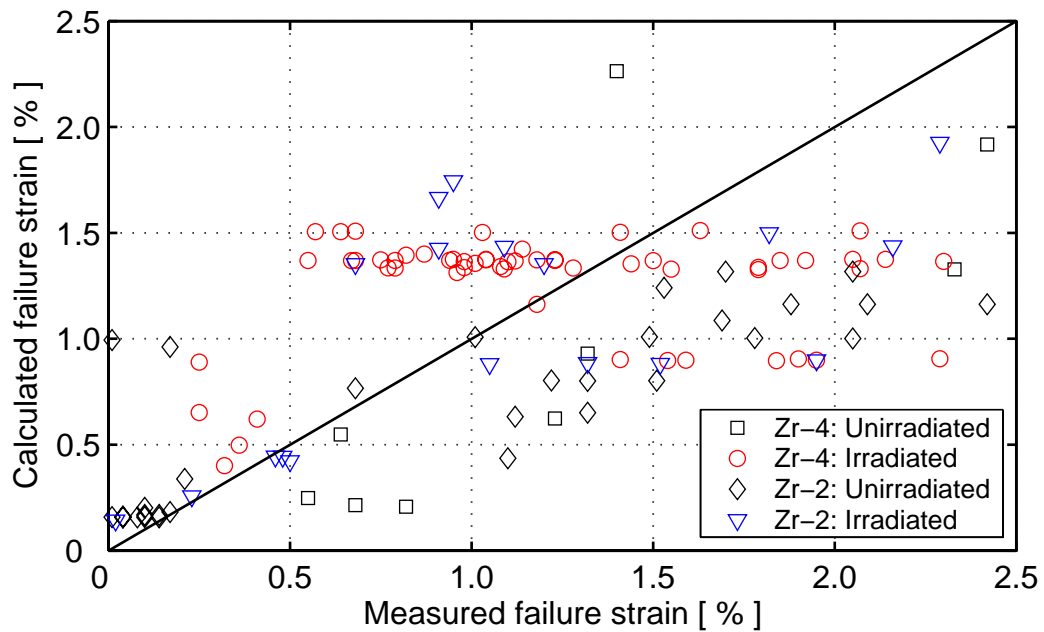


Figure 5.15: Close-up of the low-strain region in figure 5.14.

The uncertainties of the failure criterion can be estimated from statistical evaluations of absolute and relative differences between calculated and measured failure strains. Hence, for a certain test we define the absolute difference as

$$\Delta \varepsilon_f = \varepsilon_f^c - \varepsilon_f^m \quad [\%], \quad (5.24)$$

where ε_f^c and ε_f^m are the calculated and measured failure strains, respectively. The relative difference for a certain test is here defined by

$$\delta \varepsilon_f = 2 \frac{\varepsilon_f^c - \varepsilon_f^m}{\varepsilon_f^c + \varepsilon_f^m} \quad [-]. \quad (5.25)$$

The arithmetic average of ε_f^c and ε_f^m is used in the denominator of eq. (5.25), since the spread in ε_f^m is large. Moreover, ε_f^m is zero in some of the reported tests, which makes it impossible to use this parameter alone in the denominator to eq. (5.25). The average values, $\bar{*}$, and standard deviations, $\sigma(*)$, of absolute- and relative differences between calculated and measured failure strains are given in table 5.2. As can be seen from the average value of $\delta \varepsilon_f$, the failure strain correlation is a best-estimate model with respect to relative errors.

Data	$\Delta \varepsilon_f$ [%]	$\sigma(\Delta \varepsilon_f)$ [%]	$\delta \varepsilon_f$ [-]	$\sigma(\delta \varepsilon_f)$ [-]
All samples (173 tests)	-0.1322	1.1164	0.0	0.5726

Table 5.2: Statistics on absolute- and relative differences between calculated and measured failure strains.

Figures 5.16 and 5.17 show the same data as in figures 5.14 and 5.15, but for clarity, the data are shown with respect to material type only. Evidently, the predictability of the model is similar for Zircaloy-2 and Zircaloy-4, and no obvious difference can be found between the two materials. This is confirmed by table 5.3, which presents average values and standard deviations of the absolute- and relative differences between calculated and measured failure strains for Zircaloy-2 and Zircaloy-4, separately. It is interesting to note that the average value of the relative difference $\delta \varepsilon_f$ is slightly positive for Zircaloy-2 and slightly negative for Zircaloy-4. Hence, there is a small overestimation of the clad failure strain for Zircaloy-2, and a small underestimation for Zircaloy-4. In addition, the standard deviation of $\delta \varepsilon_f$ is larger for Zircaloy-2.

Data	$\Delta \varepsilon_f$ [%]	$\sigma(\Delta \varepsilon_f)$ [%]	$\delta \varepsilon_f$ [-]	$\sigma(\delta \varepsilon_f)$ [-]
Zircaloy-2 (71 tests)	-0.2907	1.0223	0.0039	0.6752
Zircaloy-4 (102 tests)	-0.0218	1.1697	-0.0022	0.4924

Table 5.3: Statistics on absolute- and relative differences between calculated and measured failure strains for Zircaloy-2 and Zircaloy-4, respectively.

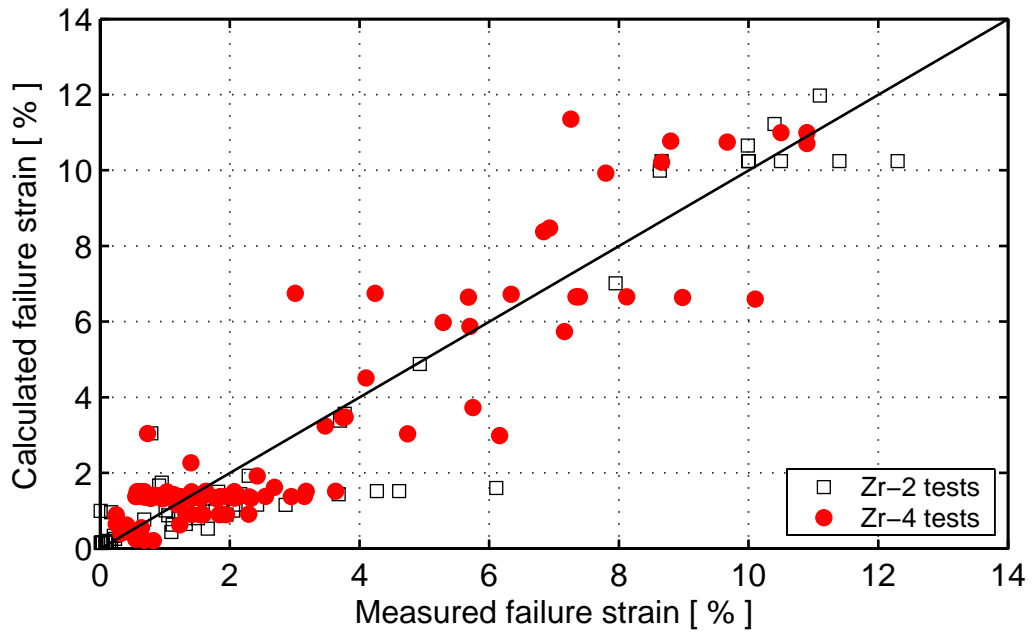


Figure 5.16: Calculated vs. measured failure strain for the database used for formulation of the failure criterion. The database comprises 71 tests on Zircaloy-2 and 102 tests on Zircaloy-4. A close-up of the low-strain region is shown in figure 5.17.

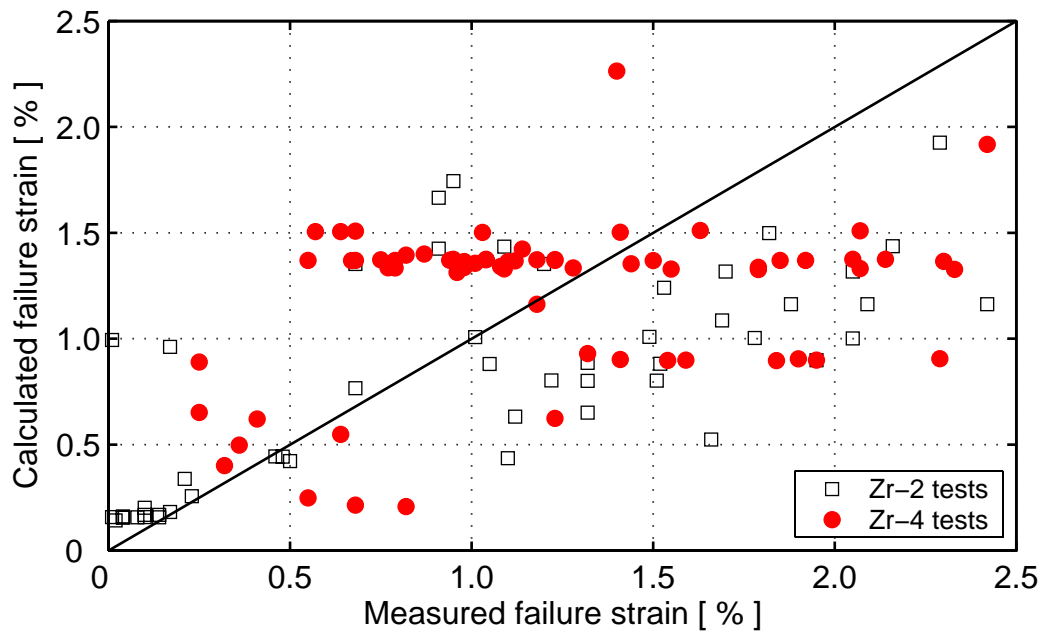


Figure 5.17: Close-up of the low-strain region in figure 5.16.

Figures 5.18 and 5.19 show the same data as in figures 5.14 and 5.15, but the data are split with respect to irradiation condition only. As evidenced by the figures, the accuracy of the model seems to be similar for un-irradiated and irradiated samples. However, it is difficult to directly compare the tests on un-irradiated and irradiated samples, since the failure strains are generally much lower in the latter.

Table 5.4 presents average values and standard deviations of the absolute- and relative differences between calculated and measured failure strains for un-irradiated and irradiated samples separately. According to the average values of the relative difference $\delta\epsilon_f$, the failure strain is slightly overestimated for irradiated samples, and slightly underestimated for un-irradiated samples.

Data	$\Delta\epsilon_f$ [%]	$\sigma(\Delta\epsilon_f)$ [%]	$\delta\epsilon_f$ [-]	$\sigma(\delta\epsilon_f)$ [-]
Un-irradiated (84 tests)	-0.0495	1.2495	-0.0103	0.5936
Irradiated (89 tests)	-0.2101	0.9751	0.0103	0.5553

Table 5.4: Statistics on absolute- and relative differences between calculated and measured failure strains for un-irradiated and irradiated samples, respectively.

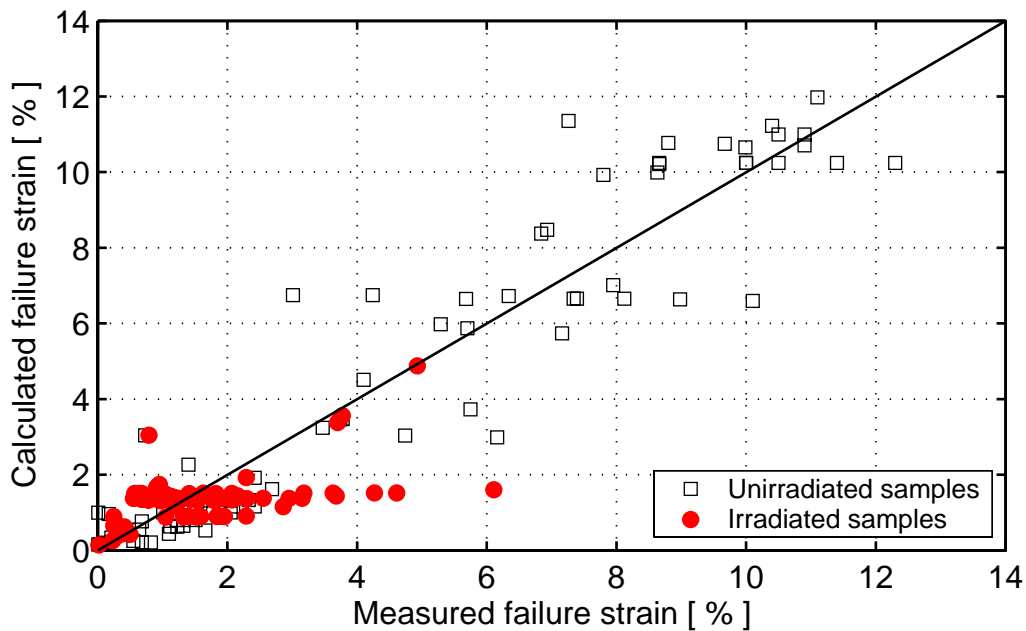


Figure 5.18: Calculated vs. measured failure strain for the database used for formulation of the failure criterion. The database comprises 84 tests on un-irradiated and 89 tests on irradiated samples. A close-up of the low-strain region is shown in figure 5.19.

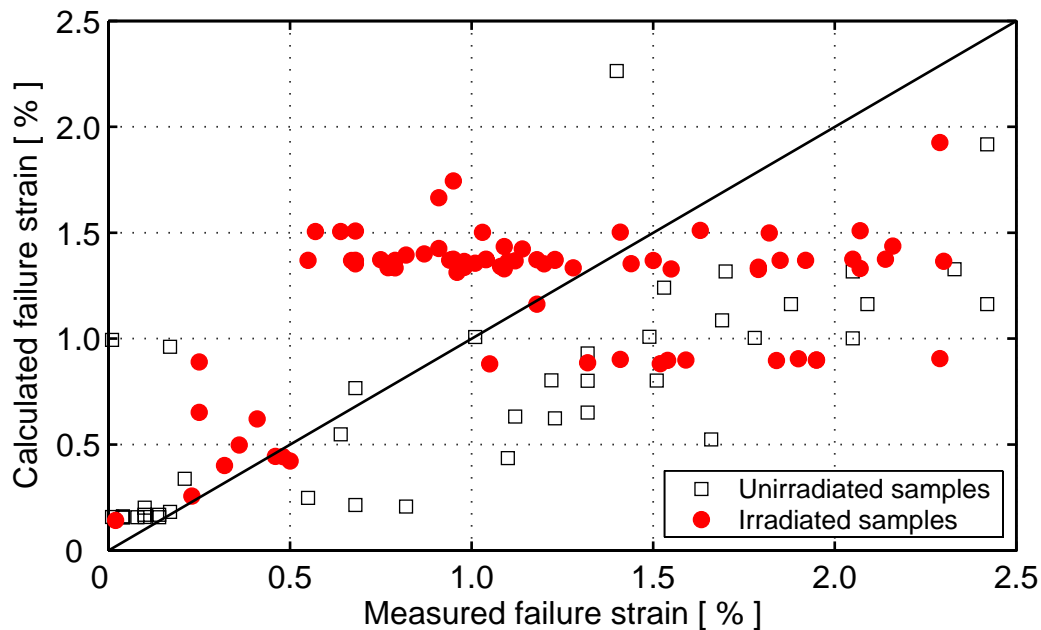


Figure 5.19: Close-up of the low-strain region in figure 5.18.

5.4.2 Sensitivity study

In the foregoing section, statistical data on the relative difference between calculated and measured failure strain were presented with respect to material type and state of irradiation. These data are useful for identifying differences between the data sets, and also provide information on model uncertainties. In the sequel, we present a sensitivity study, in which the influence of key parameters on the relative difference between calculated and measured failure strain is analysed. The purpose of this study is to identify and quantify systematic errors in the failure strain correlation.

The relative difference between calculated and measured failure strain, defined by eq. (5.25), is plotted with respect to temperature, strain rate, hydrogen content and fast neutron fluence in figures 5.20 to 5.23. The presented data comprise the previously defined 173 tests, from which the failure strain correlation is determined. A linear best fit to the presented data is included as a dot-dashed line in each figure. In an ideal situation, this regression line should coincide with the coordinate axis. Hence, the relative difference between calculated and measured failure strain should be centered around zero, and on average, they should not depend on the ordinate. A non-zero slope of the regression line indicates that the failure strain correlation does not accurately represent the database. The steeper the slope, the more significant is the error.

From figures 5.20 and 5.23, it is clear that the influence of temperature and fast neutron fluence on the clad failure strain is perfectly represented by the correlation. Figure 5.21 shows that the measured failure strains are somewhat overestimated for the high strain rate tests, but the error is very small in comparison with the spread in data.

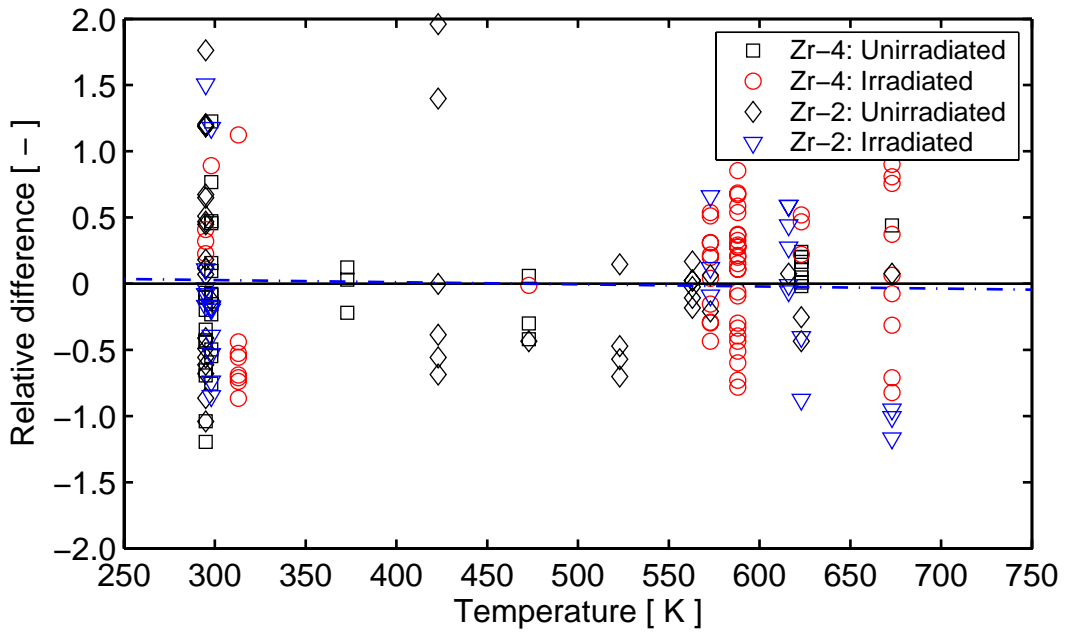


Figure 5.20: Relative differences between calculated and measured failure strain, plotted with respect to clad temperature.

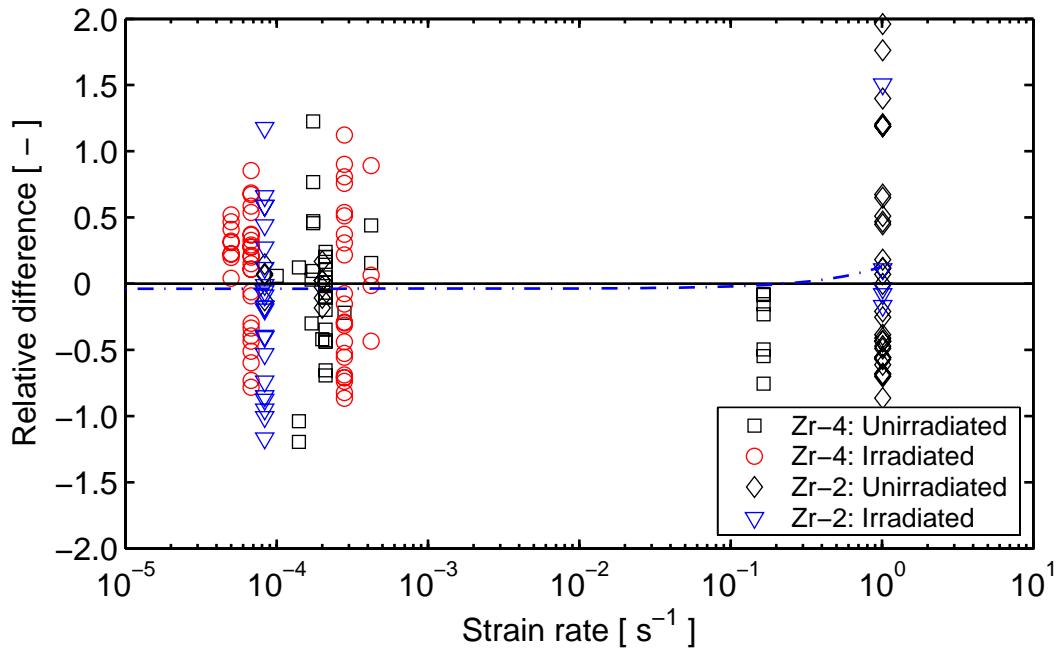


Figure 5.21: Relative differences between calculated and measured failure strain, plotted with respect to clad hoop strain rate.

Finally, it is clear from figure 5.22 that for low hydrogen concentrations, the failure strain is underestimated, whereas the opposite is true for severely hydrided material. The best agreement between measured and calculated failure strains is found at clad hydrogen concentrations around 250 wppm.

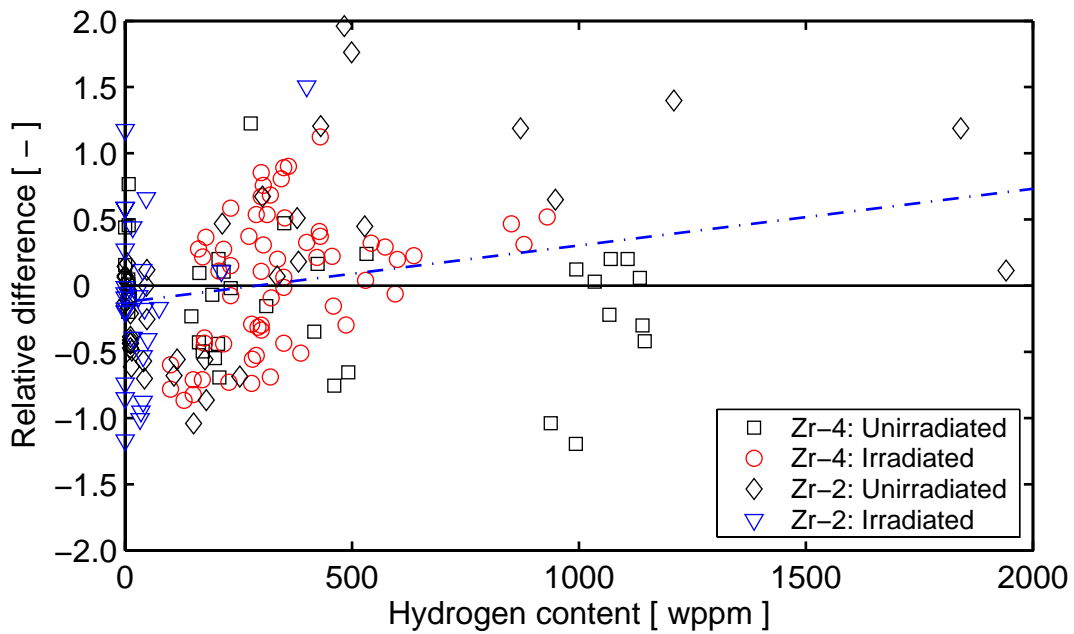


Figure 5.22: Relative differences between calculated and measured failure strain, plotted with respect to clad hydrogen content.

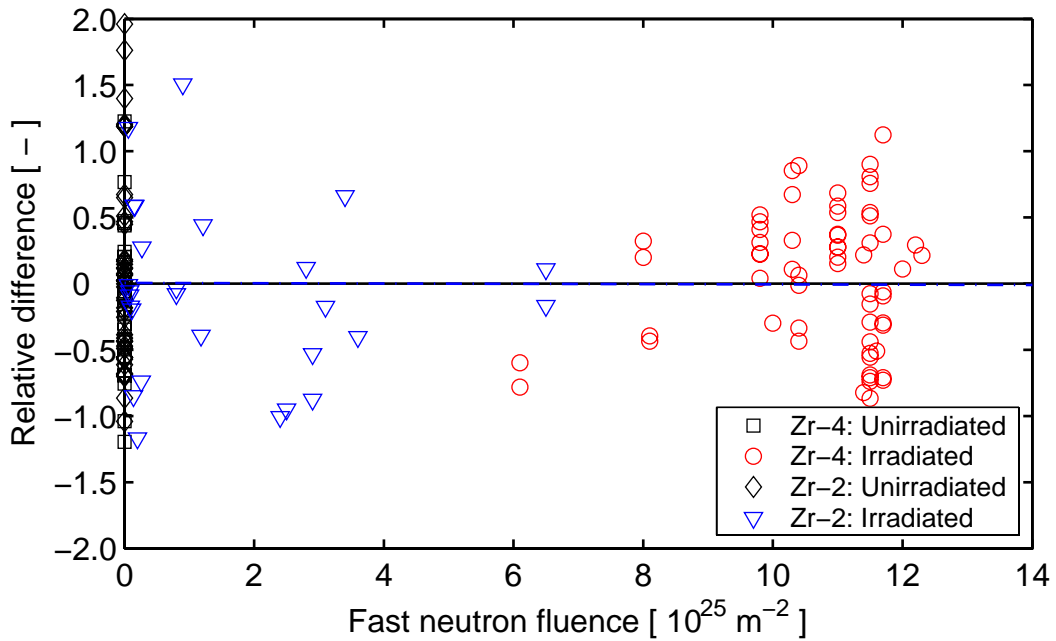


Figure 5.23: Relative differences between calculated and measured failure strain, plotted with respect to fast neutron fluence ($E \geq 1 \text{ MeV}$).

Evidently, the influence of hydrogen on clad failure strain is not perfectly captured by the correlation. However, considering the complexity of the involved physical phenomena and the comparatively simple model, the correlation does a fairly good job.

6 Discussion

In section 6.1, the failure criterion is applied in analyses of five RIA simulation tests in the CABRI pulse reactor. The purpose is to demonstrate the applicability of the criterion to in-reactor transients, and also to test the criterion in combination with the SCANAIR computer code. In section 6.2, the proposed strain-based failure criterion is compared with two failure criteria based on strain energy density. The differences between the criteria are evaluated and discussed.

Section 6.3 deals with the detrimental effects of a spalled oxide layer and non-uniform distribution of hydrogen on clad ductility. A simple approach is proposed, by which these effects can be considered in the failure criterion. Finally, we discuss the range of application and limitations of the proposed failure criterion in section 6.4.

6.1 Application of the failure criterion to CABRI tests

The proposed failure criterion is here applied in simulations of five pulse reactor tests within the CABRI REP-Na program. The analyses are performed with the SCANAIR computer code (Federici et al., 2000) and (Papin et al., 1997), into which the failure criterion has been implemented. This code calculates, among others, the time evolution of clad temperature, clad hoop plastic strain and hoop strain rate. These properties are needed as input to the failure criterion, together with the clad hydrogen content and fast neutron fluence.

All input to SCANAIR used in the performed simulations was provided by IRSN in the form of qualified input decks for each of the tests Na-1 to Na-5 (Lamare, 2001). Key properties for the considered rods and the applied test conditions are summarized in table 6.1. The clad hydrogen contents presented here were estimated from the measured clad oxide layer thicknesses. Also the presented fast neutron fluences are approximate values, estimated from fuel burnup.

Main results from the simulations with SCANAIR are summarized in table 6.2, where all data pertain to the rod axial peak power position. The damage index is simply defined as the ratio between calculated hoop plastic strain and predicted failure strain,

$$D(t) = \frac{\varepsilon_{\theta\theta}^p(t)}{\varepsilon_f(t)}, \quad (6.1)$$

where $\varepsilon_{\theta\theta}^p$ is the radial average value of the hoop plastic strain. Hence, $D < 1$ means no failure, whereas $D \geq 1$ implies clad tube failure.

The calculated maximum damage index for rod Na-1 is below unity, although the rod failed the pulse reactor test. However, the clad oxide layer of Na-1 was severely spalled, and the cladding had a non-uniform distribution of hydrides, with hydride blisters at spalled regions of the tube.

As discussed in section 6.3, the proposed failure criterion derived in section 5.3 is not applicable to cladding tubes with this kind of exceptionally non-uniform distribution of hydrogen. The failure of the criterion to accurately predict the outcome of test Na-1 is therefore not surprising.

More surprisingly, however, are the predicted failures for the uniformly oxidized rods Na-2 and Na-3, which survived the tests. The calculated damage index for rod Na-3 is close to unity, which implies that this is a borderline case. For Na-2, however, the calculated damage index indicates clear failure. From the measured plastic hoop strain, 3.5 %, one would also suspect clad failure for Na-2, considering that figure 5.18 clearly shows that the failure strain for irradiated cladding is generally below 2 to 3 % in mechanical property tests. The unexpected survival of rod Na-2 can possibly be explained by the fact that it was a test reactor rod, base-irradiated in the BR3 test reactor, and not typical of fuel rods in commercial light water reactors. Obvious differences with respect to commercial fuel rods are the high enrichment (6.85%) of the fuel pellets, and the thin oxide layer of the cladding; see table 6.1.

Property	Na-1	Na-2	Na-3	Na-4	Na-5
Neutron fluence ($E \geq 1\text{MeV}$) [10^{25} m^{-2}]	13	7	11	12	13
Pulse width [ms]	9.5	9.5	9.5	75	9.5
Max fuel enthalpy [Jg^{-1}] (calg^{-1})	460 (110)	882 (211)	502 (120)	404 (97)	439 (105)
Max plastic hoop strain [%]	-	3.5	2.1	0.4	1.1
Clad failure?	Yes	No	No	No	No
Rod peak burnup [$\text{MWdkg}^{-1}\text{U}^{-1}$]	64	33	53	62	64
Clad oxide thickness [μm]	80 ⁹	4	40	80	20
Clad hydrogen content [wppm]	> 600	30	280	570	140

Table 6.1: Summary of simulated tests. The clad hydrogen content is estimated from measured oxide layer thickness, and the neutron fluence is estimated from rod burnup.

Clad property	Na-1	Na-2	Na-3	Na-4	Na-5
Max damage index [-]	(0.62)	2.58	1.13	0.17	0.57
Max temperature [K]	921	1005	969	822	807
Max plastic hoop strain [%]	1.29	5.75	1.89	0.52	0.92
Max hoop strain rate [s^{-1}]	1.56	5.75	1.84	0.15	1.53

Table 6.2: Calculated clad properties. All data are radial average values, evaluated at the rod peak power axial position. The calculated damage index for rod Na-1 is set within brackets, since the failure criterion is not applicable to cladding with spalled oxide unless additional assumptions are made; see section 6.3 for further details.

⁹ Clad tube with severely spalled oxide layer and hydride blisters

The calculated damage index varies between the rods in close correlation to the calculated plastic hoop strain and strain rate. This is clearly seen by comparing rods Na-2 and Na-4, which were subjected to very different power pulses. The calculated damage index for rod Na-4 is well below zero, which indicates a significant margin to clad failure. As shown in table 6.2, both the calculated plastic hoop strain and the hoop strain rate are low for this rod.

6.2 Comparison with SED-based failure criteria

There are currently two criteria for clad tube failure under RIA, which are available in open literature. The best known of these criteria has been put forth by ANATECH Corporation, under the auspices of the Electric Power Research Institute (EPRI), (Rashid et al., 1995) and (Rashid et al., 2000). The second criterion is of later date, and follows very closely the approach laid out by Rashid and co-workers. It has been formulated by CIEMAT, under the sponsorship of the Spanish nuclear regulatory authority CSN, (del Barrio & Herranz, 2002).

Both criteria are based on the concept of a critical strain energy density, stating that clad failure takes place when the strain energy density (SED) in the clad material reaches a critical value. The critical value, usually termed critical strain energy density (CSED), is claimed to be a material property. However, as further shown in appendix C, this is not really the case. In the work by ANATECH and CIEMAT, the CSED is correlated to clad oxide thickness, temperature and strain rate. The correlations are fully described in appendix C.

Provided that both the stress state and the constitutive relation for the material, i.e. the relation between stresses and strains, are known, it is possible to transform a critical strain energy density into critical strain at failure and *vice versa*. This transformation, which is detailed in appendix C, allows us to compare our correlation for hoop failure strain from section 5.3 with the aforementioned correlations for CSED.

In our comparison, we consider a typical Zircaloy-4 clad tube in a 17×17 PWR fuel assembly at high burnup. The assumed clad properties are defined in table 6.3, and the calculated failure strains from our model is compared with failure strains obtained from transformed CSED in figures 6.1 to 6.4.

Clad tube properties		
Clad wall thickness	0.6	mm
Fast neutron fluence ($E \geq 1\text{MeV}$)	1×10^{26}	m^{-2}
Stress biaxiality ($\sigma_{zz}/\sigma_{\theta\theta}$)	1.0	-
Hydrogen pickup fraction	18	%

Table 6.3: Clad tube properties and test conditions assumed in the comparison between failure criteria in figures 6.1 to 6.4. A constant hydrogen pickup fraction of 18 % has been assumed in calculations of clad hydrogen content from clad oxide thickness.

Figure 6.1 shows the influence of temperature on clad failure strain, according to the three failure criteria. Here, the assumed hoop strain rate was 0.5 s^{-1} . Moreover, a $40 \text{ }\mu\text{m}$ thick oxide layer was assumed, corresponding to a clad hydrogen content of 285 wppm. Our proposed failure criterion spans the full temperature range in figure 6.1, whereas the SED-based criteria are restricted to narrower temperature bands. The restrictions are due to lack of data in the supporting databases to the SED-based criteria; see section C.2 in appendix C.

At high temperature, our proposed criterion is very close to the criterion by EPRI/ANATECH, but substantially more conservative than that of CSN/CIEMAT. At low temperature, our proposed criterion predicts a higher failure strain than the criterion by EPRI/ANATECH. Moreover, it also predicts a rapidly increasing failure strain, as the temperature is raised from room temperature.

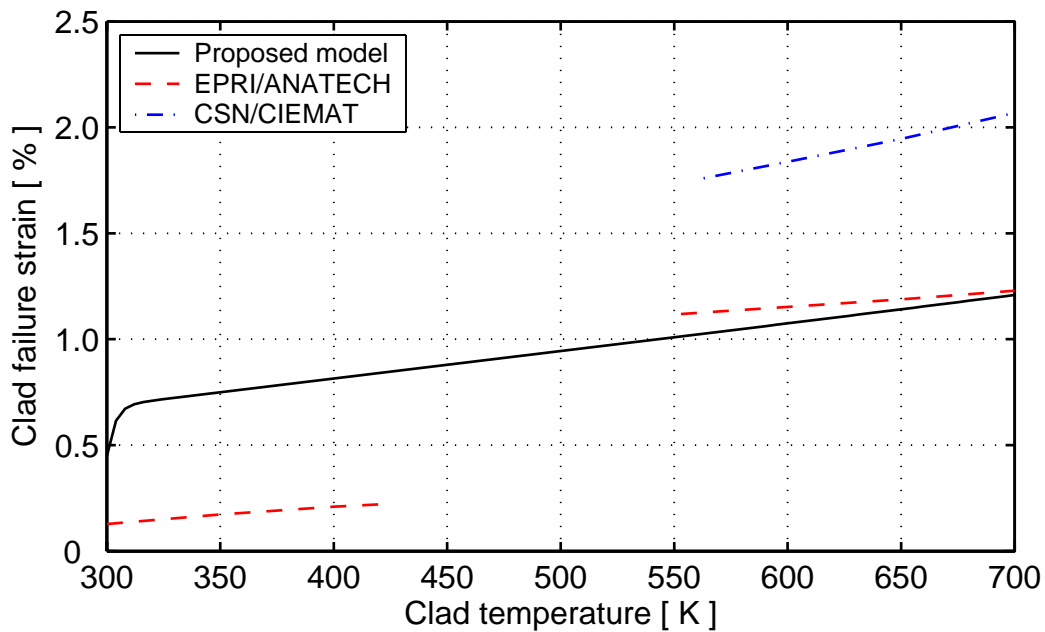


Figure 6.1: Comparison of predicted clad failure strains with respect to temperature. Failure strains from the correlations by ANATECH and CIEMAT are transformed values, calculated from critical strain energy density as described in appendix C.

Figure 6.2 shows the calculated influence of hoop strain rate on clad failure strain. Here, the assumed clad temperature was 600 K, whereas the oxide layer and hydrogen content are the same as assumed in figure 6.1. Obviously, our proposed criterion is very close to the criterion by EPRI/ANATECH at low strain rates, but at strain rates above 0.2 s^{-1} , it predicts a clear drop in failure strain, which is not seen in the criterion by EPRI/ANATECH. On the other hand, this drop is predicted by the CSN/CIEMAT criterion, although the magnitude of the failure strain is higher for that model.

Finally, it should be noticed that the proposed criterion has an upper cut-off limit at a hoop strain rate of 1.0 s^{-1} . This limit corresponds to the maximum strain rate applied in the mechanical property tests, on which the criterion is based. Application of the criterion to strain rates above this limit is therefore not recommended; see section 6.4.

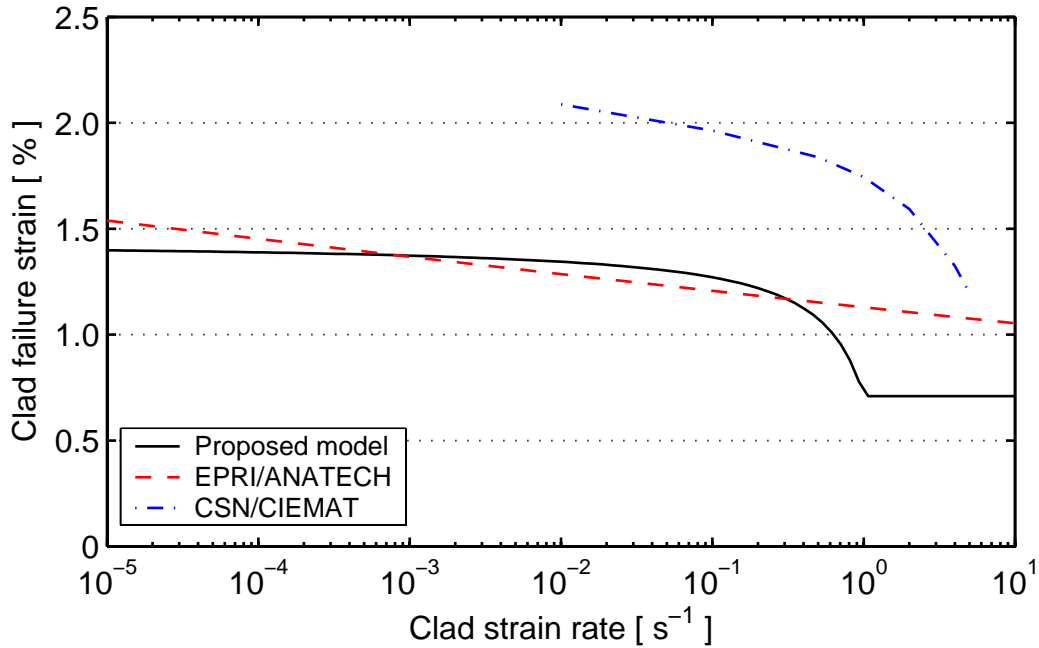


Figure 6.2: Comparison of predicted clad failure strains with respect to hoop strain rate. Failure strains from the correlations by ANATECH and CIEMAT are transformed values, calculated from critical strain energy density as described in appendix C.

Figures 6.3 and 6.4 show the calculated influence of clad hydrogen content on failure strain. The results in figure 6.3 are for room temperature, whereas figure 6.4 shows the calculated influence of hydrogen at 600 K. A hoop strain rate of 0.5 s^{-1} was used for both calculated cases.

At room temperature, the failure strain calculated by our proposed model follows about the same trend with respect to clad hydrogen content as the EPRI/ANATECH model, although our predicted failure strain is generally higher. For the high-temperature case considered in figure 6.4, our proposed failure criterion predicts that clad embrittlement is dominated by irradiation damage and elevated strain rate, and that the additional embrittlement by hydrogen is negligible at this temperature. This is much different from the SED-based failure criteria, which predict a significant influence of hydrogen also at high temperature.

A comment should be made on the range of hydrogen content displayed in figure 6.4: Clad average hydrogen concentrations above 500 wppm are hardly found in clad tubes with uniform oxide layers. Concentrations in excess of 500 wppm are normally found only in cladding with spalled oxide. However, none of the failure criteria shown in figure 6.4 account for the detrimental effect of oxide spallation on clad ductility, which means that the right-hand part of figure 6.4 is actually outside the range of application for the criteria. This is further discussed in section 6.3.

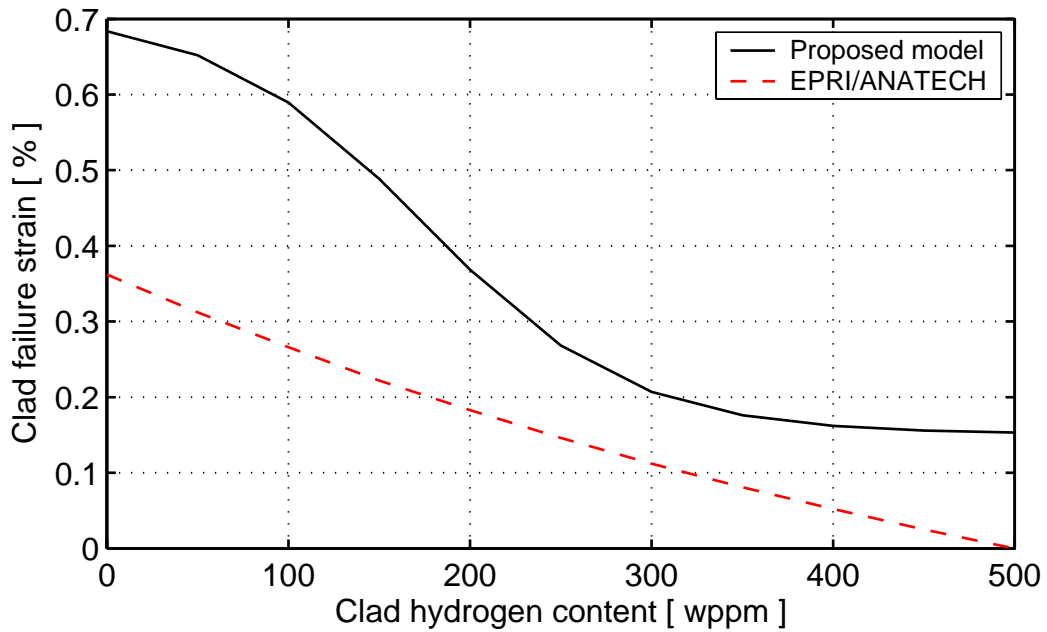


Figure 6.3: Comparison of predicted clad failure strains with respect to hydrogen content at a clad temperature of 295 K. Failure strains from the correlation by ANATECH are transformed values, calculated from critical strain energy density as described in appendix C.

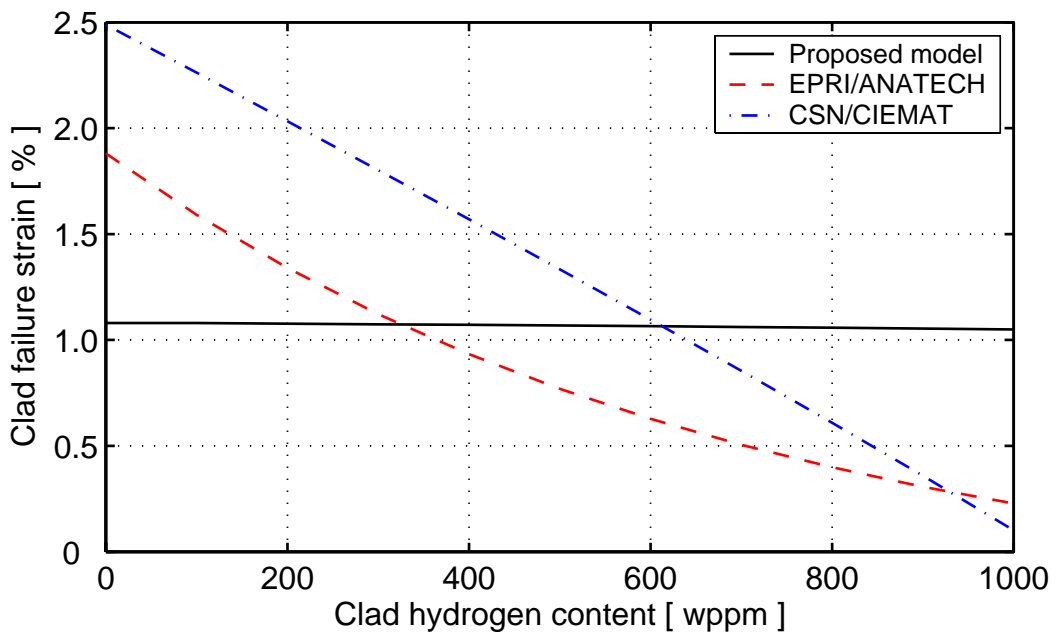


Figure 6.4: Comparison of predicted clad failure strains with respect to hydrogen content at a clad temperature of 600 K. Failure strains from the correlations by ANATECH and CIEMAT are transformed values, calculated from critical strain energy density as described in appendix C.

In conclusion, the presented comparison shows that there are significant differences between the considered clad failure criteria. The criterion proposed by CSN/CIEMAT generally yields failure strains that are much higher than those predicted by the other two criteria. However, the failure strains predicted by our proposed criterion agree surprisingly well with those of the EPRI/ANATECH model for high temperatures, low strain rates and clad hydrogen concentrations around 300 wppm.

An additional comparison of the considered failure criteria is made by applying them to the simulated CABRI pulse reactor tests in section 6.1. To this end, the damage index defined in eq. (6.1) for our strain-based failure criterion is compared with calculated damage indices for the SED-based criteria. These damage indices are simply defined by

$$D(t) = \frac{SED(t)}{CSED(t)}, \quad (6.2)$$

where SED is the radial average value of the strain energy density, calculated by SCANAIR, and the critical strain energy density CSED is calculated through the correlations proposed by EPRI/ANATECH and CSN/CIEMAT, respectively. It should be remarked that this procedure may yield somewhat misleading results: As explained in appendix C, the correlations for CSED proposed by both EPRI/ANATECH and CSN/CIEMAT are determined from mechanical property tests on Zircaloy-4 by use of a stress-strain relation from MATPRO (Hagrman et al., 1981). For consistency, the same material model should be used in SCANAIR for calculating SED. However, this is not the case, and the calculated damage index from eq. (6.2) could possibly be biased by differences between the stress-strain relation used in SCANAIR and the one defined in MATPRO. This illustrates a fundamental drawback with SED-based failure criteria: for consistency, the stress-strain relation used for determining the CSED from material property tests must also be applied in the computer code used for evaluating the SED under a simulated transient.

The maximum values of the damage indices, calculated at the peak power positions of each rod, are presented in table 6.4. The calculated damage indices for rod Na-1 is set within brackets, since none of the failure criteria is applicable to cladding with spalled oxide and non-uniform hydrogen distributions. See section 6.3 for further details on this matter.

Failure criterion	Na-1	Na-2	Na-3	Na-4	Na-5
Proposed model (Strain)	(0.62)	2.58	1.13	0.17	0.57
EPRI/ANATECH (SED)	(1.12)	0.85	0.80	0.58	0.48
CSN/CIEMAT (SED)	(0.70)	0.63	0.51	0.36	0.33

Table 6.4: Calculated damage indices for the CABRI tests discussed in section 6.1. The damage index is calculated through eq. (6.1) for the proposed strain-based failure criterion, and through eq. (6.2) for the SED-based criteria.

The largest differences between the criteria are found in the calculated damage indices for rod Na-2 and Na-4. From table 6.1, it is clear that these rods were subjected to very different power pulses, both with respect to pulse width and amplitude.

From the results in table 6.4, it seems that our proposed failure criterion is more sensitive to the differences in pulse characteristics than the SED-based criteria. For the “normal” power pulses in tests Na-3 and Na-5, the calculated damage indices from our proposed failure criterion and the criterion by EPRI/ANATECH are quite close. The damage indices predicted by the CSN/CIEMAT criterion are generally lower than those from the other two criteria, which supports the conclusions drawn earlier in this section.

6.3 Effect of spalled oxide layer

As mentioned in section 5.4.1, the database, from which the failure strain correlation in section 5.3 is derived, does not include irradiated samples with spalled oxide or hydride blisters, nor does it include un-irradiated hydrogen charged samples with purposely introduced hydride rims or radial hydrides. These samples were excluded from the database, since the proposed failure criterion is neither intended to, nor capable of handling the embrittling effects of a non-uniform hydrogen distribution in the cladding.

However, it is interesting to compare the failure strains measured in the excluded tests on samples with non-uniform hydrogen distributions, with those calculated by our model. Such a comparison is shown in figures 6.5 and 6.6. Distinction is here made between “ordinary samples”, which are the previously considered 173 samples with comparatively uniform hydrogen distribution, and the hitherto excluded samples with spalled oxide, hydride rim or unusually large fractions of radial hydrides.

As expected, the failure strain is generally overestimated for the samples with non-uniform hydrogen distribution or radial hydrides. In particular, the un-irradiated samples with hydride rim fail at much lower strain than predicted by the model. However, one should bear in mind that these samples are prepared by hydrogen charging, aimed at producing a marked hydride rim. The behaviour of these specimens is therefore not necessarily representative of clad tubes degraded by in-reactor irradiation, oxidation and hydriding.

The samples with spalled oxide, on the other hand, originate from clad tubes that have been operated and irradiated in commercial reactors. Their behaviour is therefore without doubt representative. It is interesting to note that the failure strain is accurately calculated for two of these samples, whereas it is strongly overestimated for the remaining nine samples with spalled oxide. A closer investigation into possible differences between these two groups of data reveals that the accurately predicted tests were performed at room temperature, whereas the overestimated tests were made at elevated temperature. This is illustrated in figure 6.7, where the ratio between calculated and measured failure strain is plotted with respect to temperature for the eleven samples with spalled oxide. For the two low-temperature tests, the calculated failure strains agree quite well with those measured, but for the high-temperature tests, the failure strain is significantly overestimated. The average value of the ratio between calculated and measured failure strain for the nine high-temperature tests is 3.6.

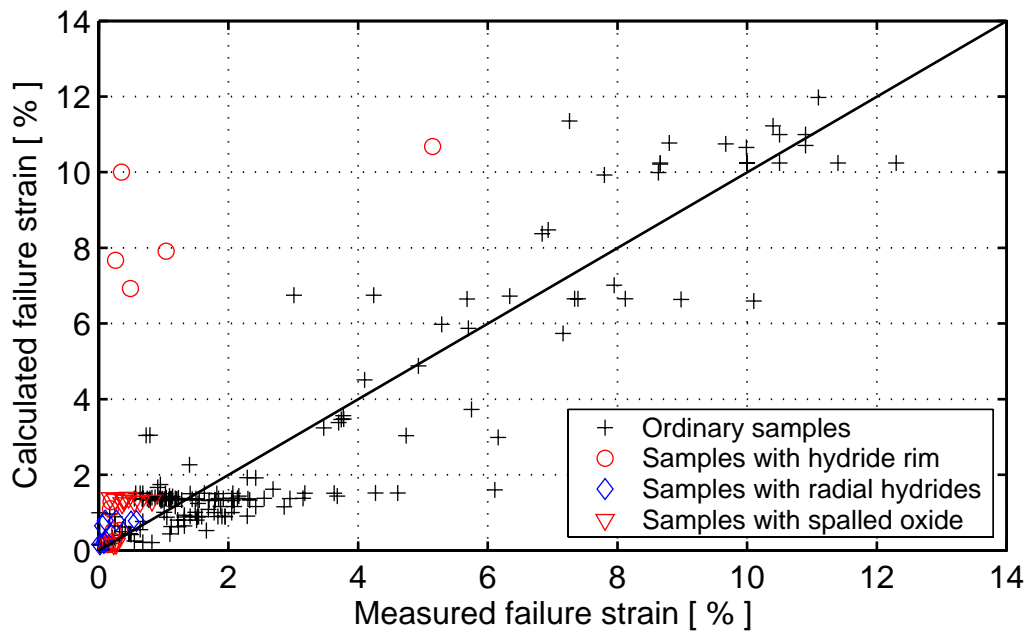


Figure 6.5: Calculated vs. measured failure strain. The “ordinary samples” have uniform hydrogen distribution, and constitute the database from which the failure strain correlation is determined.

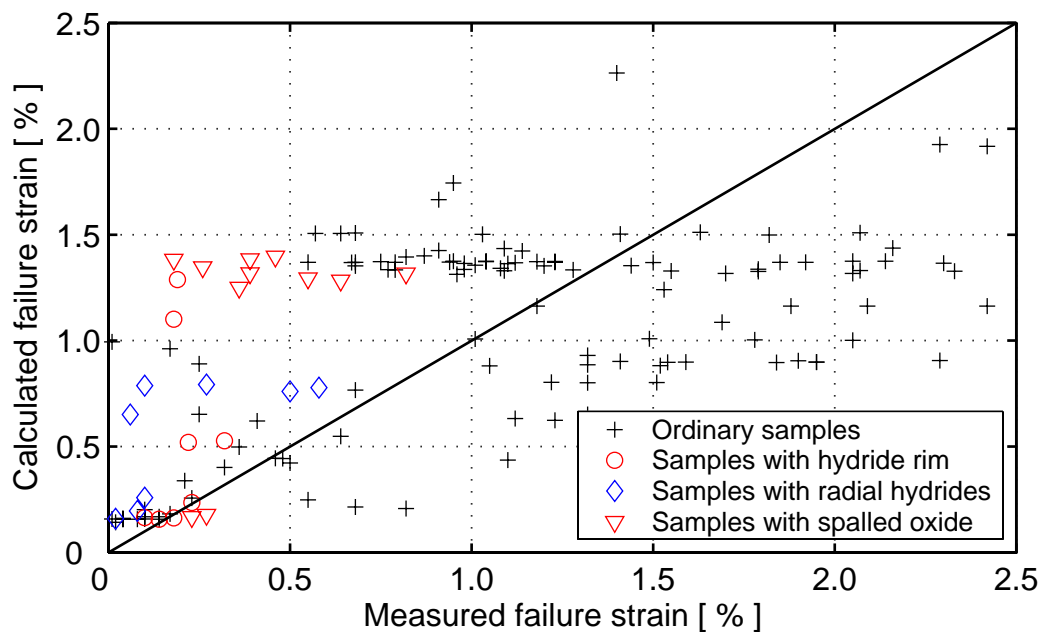


Figure 6.6: Close-up of the low-strain region in figure 6.5.

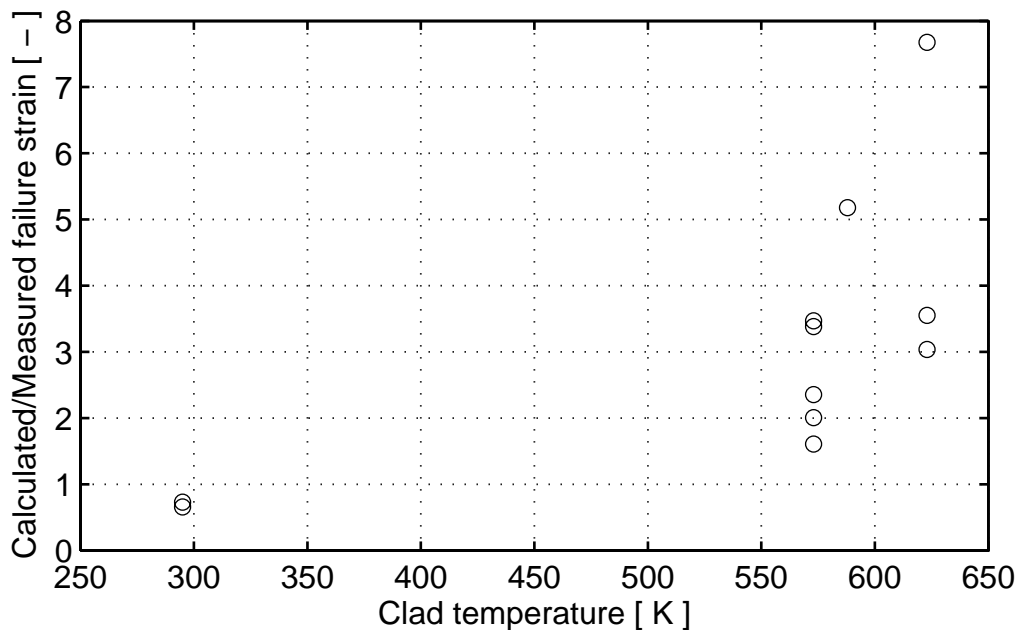


Figure 6.7: Ratio of calculated to measured failure strain vs. temperature for irradiated samples with spalled clad oxide layer.

Figure 6.7 is interesting, since it indicates that oxide layer spallation, resulting in build-up of a non-uniform hydrogen distribution in the cladding, has a detrimental effect on clad ductility only at elevated temperatures. At room temperature, the ductility of spalled samples is not notably different from that of samples with smooth oxide layers and uniform hydrogen distributions. A plausible explanation to this observation is that the ductility of densely hydrided material at spalled regions differs significantly from that of normally hydrided material only at elevated temperature. At room temperature, the difference in ductility between the material at spalled and non-spalled regions of the cladding is probably less pronounced, which means that the macroscopic behaviour of the clad tube can be fairly well characterized by the average hydrogen content.

As mentioned in section 5.4.1, fuel performance codes are usually not capable of handling oxide layer spallation and its consequences on the clad hydrogen distribution. The embrittling effect of hydride blisters or densely hydrided regions at spalled regions of the clad tube can only be predicted, if detailed information on the shape and properties of the blisters are known.

A fracture mechanics approach to treat the embrittling effects of blisters have recently been presented by Pierron et al. (2003), who also performed mechanical tests on small-scale un-irradiated Zircaloy-4 sheet samples with artificially induced hydride blisters. The embrittling effects of hydride blisters and other local clad defects have also been approached within the theoretical framework of localized plasticity; see e.g. the work by Link et al. (1997) and Jernkvist (2003). Unfortunately, both these approaches require detailed data on the local clad defects, which are not available in predictive analyses of the fuel rod behaviour. The required data can only be obtained *a posteriori*, by post-irradiation metallographic examinations of the clad material.

However, a very simple approach for considering the effect of oxide spallation in predictive analyses would be to reduce the predicted failure strain from the correlation in section 5.3, based on the data shown in figure 6.7. Hence, for clad tubes with spalled oxide layers, we modify the failure strain correlation

$$\varepsilon_f^{Spalled} = \varepsilon_f \cdot S(w_{Ox}, T), \quad (6.3)$$

where ε_f is the failure strain of non-spalled clad tubes, and S is a reduction factor, which depends on the clad average oxide thickness, w_{Ox} , and clad temperature. Based on the observation that oxide spallation usually occurs when the clad oxide layer thickness is in the range from 60 to 100 μm (Garzarolli & Holzer, 1992), we assume that clad ductility decreases gradually in this interval, and thus propose the following form for the ductility reduction factor

$$S(w_{Ox}, T) = \begin{cases} 1.0 & w_{Ox} < 60 \mu\text{m} \\ \frac{5 - 3S_\infty}{2} - \frac{1 - S_\infty}{40} w_{Ox} & 60 \mu\text{m} \leq w_{Ox} \leq 100 \mu\text{m} \\ S_\infty & 100 \mu\text{m} < w_{Ox} \end{cases} \quad (6.4)$$

Here, S_∞ is the ductility reduction factor for clad tubes with fully developed oxide spallation. From the data in figure 6.7, we find

$$S_\infty = \begin{cases} 1.0 & \text{at room temperature} \\ 1/3.6 = 0.28 & \text{at elevated temperature} \end{cases} \quad (6.5)$$

To conclude, we illustrate the effect of the ductility reduction factor defined above by re-calculating the case presented in figure 6.4. Here, we assume a constant hydrogen pick-up fraction of 18 %, which means that the clad hydrogen content c_H is proportional to the oxide layer thickness through

$$c_H = 7.11 w_{Ox}, \quad (6.6)$$

where c_H is in wppm and w_{Ox} is in microns. In figure 6.8, we compare the failure strain calculated without consideration of oxide spallation, i.e. ε_f in eq. (6.3), with $\varepsilon_f^{\dot{}}$ from the same equation.

Finally, it could be interesting to apply the reduction factor S in eq. (6.4) to the simulation of rod Na-1 in the CABRI REP-Na tests, which was described in section 6.1. Rod Na-1 was severely spalled, with an average oxide layer thickness of 80 μm . In this case, it would therefore be natural to set $S = S_\infty$, since the clad oxide is known to be severely spalled. However, we disregard this information, and from the oxide layer thickness, we find $S = 0.64$ by use of eq. (6.4).

If oxide spallation is considered, the calculated clad damage index for rod Na-1 thus changes from 0.62 to $0.62/0.64 = 0.97$. Hence, our failure criterion still predicts survival of rod Na-1, although the predicted margin to failure is very small.

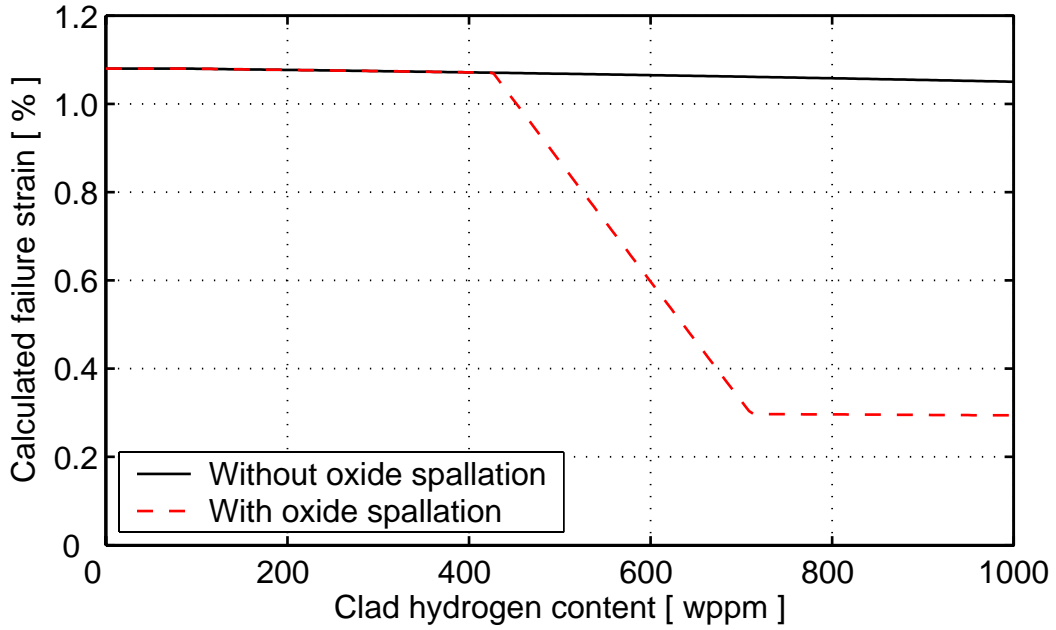


Figure 6.8: Predicted effect of oxide spallation at a clad temperature of 600 K. Equations (6.3) to (6.5) are applied to the case presented in figure 6.4 of section 6.2.

6.4 Range of application and limitations

The proposed clad failure criterion is determined from out-of-pile mechanical property tests, performed on clad tubes of standard Zircaloy-2 and Zircaloy-4. The application of the criterion should be restricted to these materials and to clad operating conditions, which are spanned by the supporting database. Consequently, the range of application for the failure criterion is limited to temperatures, strain rates, fast fluences and clad hydrogen contents defined in table 6.5.

The upper limit for the clad hydrogen content in table 6.5 is not the maximum concentration in the tested samples. A large number of tests in the database were in fact performed on samples with higher hydrogen concentrations, but these were all un-irradiated hydrogen-charged samples, which are not necessarily representative of highly irradiated and oxidized cladding. The upper limit of 750 wppm in table 6.5 represents the highest average hydrogen concentration among the irradiated, in-reactor oxidized samples in the database.

Clad property		Range
Material		Zr-2, Zr-4
Temperature	[K]	295 – 673
Hoop strain rate	[s ⁻¹]	1x10 ⁻⁶ – 1.0
Neutron fluence ($E \geq 1\text{MeV}$)	[m ⁻²]	0 – 1.2x10 ²⁶
Hydrogen content	[wppm]	0 – 750

Table 6.5: Range of application for the proposed failure criterion. All numbers refer to clad radial average values.

It should be noticed that the criterion can be applied also to clad tubes with spalled oxide, although its experimental support is restricted to only 11 mechanical property tests made on clad tubes with spalled oxide.

The database is limited to Zircaloy-2 and Zircaloy-4 clad tubes of standard design, and does neither include tests on liner (duplex) cladding, nor tests on Zr-Nb alloys for light water reactors, such as ZIRLO or M5. However, there is no reason to believe that the ductility of the latter materials is substantially different from that of Zircaloys, at comparable hydrogen concentrations. In other words, the expected differences between Zr-Nb alloys and the standard Zircaloys are primarily in the oxidation rates and the hydrogen pickup fractions, but not in the mechanical properties.

The ductility of irradiated Zircaloy-4 and ZIRLO at high strain rate has actually been compared in recent tests at Studsvik, Sweden (Grigoriev et al., 2002). The total (elastic+plastic) hoop strain to failure of the two materials was measured in EDC (“Expansion Due to Compression”) tests, at hoop strain rates ranging from 0.2 to 2.4 s⁻¹. Four ZIRLO tube samples were fabricated from a 15×15 PWR fuel rod, irradiated to a rod average burnup of 50 MWdkg⁻¹U⁻¹ in Ringhals 2. For comparison, five Zircaloy-4 samples were taken from a 17×17 PWR fuel rod, irradiated in Ringhals 3 to a rod average burnup of 54 MWdkg⁻¹U⁻¹. The samples, tests conditions and results for the nine samples are summarized in table 6.6.

Clad property	ZIRLO samples				Zircaloy-4 samples				
	1a	1b	3a	3b	A	B	C	D	E
Temperature [K]	298	298	298	613	293	293	613	613	293
Hydrogen [wppm]	125	125	550	550	650	570	470	530	320
Oxide layer [μm]	17	17	50-60	50-60	50-55	55-60	60-65	55	35-40
Strain rate [s ⁻¹]	≈0.2	≈2	≈0.2	≈0.2	0.23	0.15	0.37	2.4	≈0.2
Max hoop strain [%]	6.7	17.3	3.4	10.8	2.3	1.5	3.7	7.3	1.9
Clad failure?	No	No	Yes	No	Yes	Yes	No	Yes	Yes

Table 6.6: Summary of Studsvik EDC tests on irradiated ZIRLO and Zircaloy-4 cladding. Data from Grigoriev et al. (2002).

It is interesting to note that only one of the ZIRLO samples failed, and that it failed at a higher total strain than the two Zircaloy-4 samples (A and B) that had comparable hydrogen content and test temperature. Moreover, the unfailed ZIRLO samples were remarkably ductile.

Albeit the number of tests is small, the comparison indicates that ZIRLO has superior ductility to Zircaloy-4 at comparable hydrogen concentrations. In conclusion, application of the proposed failure criterion to fuel rods with ZIRLO cladding is justified, and with consideration of the results from the Studsvik EDC tests, failure will most likely be conservatively predicted for ZIRLO cladding.

High strain rate tests on irradiated cladding are scarce, and only five tests of this kind are currently available in the database; see section 4.2. If more data of this kind become available in the future, it is highly recommended to at least compare the experimentally measured hoop plastic strains to failure with those predicted by our correlation. If needed, the new tests should be included in the database, and the correlation tuned to the new set of data.

As mentioned in section 5.2.1, the study on Zr-1%Nb by Kaplar et al. (2001) is to our knowledge the only tests that have been made on irradiated cladding under RIA-relevant loading conditions, i.e. under pure biaxial stress ($\sigma_{zz}/\sigma_{\theta\theta}=1$). Considering the observed importance of stress state to ductility for un-irradiated material, additional tests of this kind on irradiated cladding are certainly warranted (Fuketa et al., 2003). Such tests would eliminate much of the uncertainty in adapting burst- and axial tension test data to biaxial stress conditions. As described in section 5.2.1, the adaptation used in our study is based on investigations performed on un-irradiated material at room temperature.

Finally, we note that all mechanical property tests in the considered database were made at constant and uniform clad temperature. The testing conditions are thus very much different from those expected under an RIA, where the temperature varies in both space and time. The difference can be important for two reasons:

- The effects of a radial temperature gradient across the clad wall on local material properties and thermal stresses are overlooked in the mechanical property tests.
- Time-dependent effects on e.g. hydride dissolution and brittle-to-ductile transition are also overlooked in the mechanical property tests.

The importance of these effects on the clad behaviour under RIA can only be assessed by performing mechanical property tests under transient heating. Such tests have been tried within the PROMETRA experimental program, but unfortunately, they suffer from lack of temperature control in the samples (Balourdet et al., 1999). A new improved testing technique is underway (Yvon et al., 2001).

7 Conclusions

A strain-based failure criterion for prediction of clad tube failure under reactivity initiated accidents in light water reactors was derived, based on data from more than 200 out-of-pile mechanical property tests on Zircaloy-2 and Zircaloy-4 cladding. Most of these tests are clad tube burst tests, which were shown to be more representative of the true loading conditions under RIA than e.g. uniaxial tensile tests or ring specimen tests. From the experimental database, which comprises both highly irradiated cladding and un-irradiated hydrogen-charged samples, we formulated a correlation for clad hoop plastic strain at failure, ε_f , with respect to clad temperature, irradiation damage, strain rate and hydrogen content. The correlation for ε_f takes the form

$$\varepsilon_f = \frac{3 \cdot \varepsilon_{f0} \cdot S \cdot f_1 \cdot f_2 \cdot f_3}{f_1 \cdot f_2 + f_1 \cdot f_3 + f_2 \cdot f_3}, \quad (7.1)$$

where ε_{f0} represents the failure strain of as-fabricated cladding at low strain rate, S is a ductility reduction factor, catering for detrimental effects of oxide spallation, and f_1 , f_2 and f_3 are ductility reduction factors accounting for elevated strain rate, hydrogen-induced embrittlement and irradiation damage, respectively. The correlation is a best-fit to experimental data, but it is based on the conservative assumption that a biaxial tangential-axial stress state ($\sigma_{zz}/\sigma_{\theta\theta}=1$) prevails in the clad tube under RIA. Hence, ε_f represents the clad hoop plastic strain at failure under biaxial loading.

Clad tube failure is assumed to take place when

$$\varepsilon_{\theta\theta}^p \geq \varepsilon_f, \quad (7.2)$$

where $\varepsilon_{\theta\theta}^p$ is the radial average hoop plastic strain in any cross-section of the clad tube. The failure criterion in eq. (7.2) is strictly focused on PCMI-induced clad tube failure under the early heat-up phase of RIA, which is believed to be the most restricting failure mode for high-burnup fuel rods. The range of application for the proposed failure criterion is defined in table 7.1.

Clad property		Range
Material		Zr-2, Zr-4
Temperature	[K]	295 – 673
Hoop strain rate	[s ⁻¹]	1x10 ⁻⁶ – 1.0
Neutron fluence ($E \geq 1\text{MeV}$)	[m ⁻²]	0 – 1.2x10 ²⁶
Hydrogen content	[wppm]	0 – 750

Table 7.1: Range of application for the proposed failure criterion. All numbers refer to clad radial average values.

Since the criterion is derived from mechanical property tests on Zircaloy-2 and Zircaloy-4 only, it should strictly not be applied to other clad materials. However, a limited number of EDC tests on irradiated ZIRLO cladding have recently been performed in Studsvik, and the results of these tests indicate that failure will most likely be conservatively predicted, if the proposed criterion is applied to ZIRLO cladding.

Statistical evaluations of the failure strain correlation and its supporting database showed that the standard deviation of relative differences between predicted and measured failure strain was 0.57. This is a relatively large value, which reflects the spread in experimental failure strain data.

A sensitivity study with respect to clad temperature, strain rate, fast neutron fluence and hydrogen content was performed in order to identify and quantify systematic errors in the failure strain correlation. The study revealed that the correlation accurately captures the influence of all aforementioned parameters, but that the failure strain is somewhat underestimated for hydrogen levels < 250 wppm, whereas it is overestimated for hydrogen concentrations above this value.

The proposed failure criterion was compared with two criteria from open literature. These criteria, formulated by EPRI/ANATECH and CSN/CIEMAT, respectively, are based on the concept of critical strain energy density and intended for prediction of clad tube failure under RIA in pressurized water reactors. The comparison showed that there are significant differences between the considered clad failure criteria. The criterion proposed by CSN/CIEMAT generally yields failure strains that are much higher than those predicted by the other two criteria. Moreover, our proposed criterion seems more sensitive to strain rate and less sensitive to clad hydrogen content than the criteria based on critical strain energy density. The observed differences are understandable, since the underlying experimental databases differ between the criteria. In addition, the criteria based on critical strain energy density rely on constitutive relations for the clad material, which are probably not identical to the one used in this report for transforming critical strain energy density into hoop strain at failure. However, the failure strains predicted by our proposed criterion agree surprisingly well with those of the EPRI/ANATECH model for high temperatures, low strain rates and clad hydrogen concentrations around 300 wppm.

Finally, the proposed failure criterion was applied in simulations of five pulse reactor tests within the CABRI REP-Na program. The simulations were made with the SCANAIR computer code, into which the failure criterion has been implemented. Reasonable clad failure strains were calculated for the five simulated tests, although failure/no-failure was accurately predicted for only two of the five tests.

Based on the performed analysis of mechanical property test data and simulated pulse reactor tests, we conclude that the proposed failure criterion is able to predict clad tube failure for a wide spectrum of transient conditions with fair accuracy. In particular, the range of application covers reactivity initiated accidents at BWR CZP as well as PWR HZP conditions.

8 Nomenclature

The symbols and abbreviations used in this report are listed below, together with a brief explanation to the notation. The ambition to conform to prevalent nomenclature in international literature has unfortunately lead to inevitable conflicts. However, in case a symbol is used in different contexts with different meanings, this is clearly indicated in the list. Throughout the text, all mathematical symbols are printed in italic.

Latin symbols:

A_o	Test specimen cross-sectional area	[m ²]
c_H	Hydrogen concentration	[wppm]
c_{TSS}	Hydrogen terminal solid solubility (solubility limit)	[wppm]
C_R	Reduction factor used in evaluation of total elongation data	[-]
D	Clad damage index	[-]
E	Neutron energy	[eV]
E_Y	Young's modulus	[Pa]
f_1	Clad ductility reduction factor related to elevated strain rate	[-]
f_2	Clad ductility reduction factor related to hydrogen	[-]
f_3	Clad ductility reduction factor related to irradiation	[-]
F	Total clad ductility reduction factor	[-]
H_p	Radially averaged fuel peak enthalpy	[J(gUO ₂) ⁻¹]
L_o	Test specimen gage length	[m]
R	Universal gas constant ($R=8.3143$)	[Jmol ⁻¹ K ⁻¹]
t	Time	[s]
S	Clad ductility reduction factor related to oxide spallation	[-]
T	Temperature	[K]
w_{Ox}	Clad oxide layer thickness	[m]
x	Ratio of clad oxide thickness to clad wall thickness	[-]

Greek symbols:

δ	Extension of test sample due to local deformation (necking)	[m]
$\epsilon_{\theta\theta}$	Clad hoop strain (relative elongation in circumferential direction)	[-]
ϵ_f	Clad failure strain (calculated clad hoop plastic strain to failure under biaxial loading, i.e. under $\sigma_{zz}/\sigma_{\theta\theta} = 1$)	[-]
ϵ_{te}	Total elongation (measured plastic strain to failure)	[-]
ϵ_{ue}	Uniform elongation (measured plastic strain to instability)	[-]
ϕ	Clad fast neutron fluence ($E>1\text{MeV}$)	[m ⁻²]
σ	Uniaxial or effective stress	[Pa]
$\sigma_{\theta\theta}$	Clad hoop (circumferential) stress	[Pa]
σ_{zz}	Clad axial (longitudinal) stress	[Pa]
σ_y	Clad yield stress	[Pa]
$\sigma(x)$	Standard deviation of variable x	

Abbreviations:

BWR	Boiling Water Reactor
CIEMAT	Centro de Investigaciones Energéticas, Medioambientales y Tecnológicas (Spanish Research Centre for Energy, Environment and Technology)
CRDA	Control Rod Drop Accident
CSED	Critical Strain Energy Density
CSN	Consejo de Seguridad Nuclear (Spanish Commission for Nuclear Safety)
DBT	Ductile-to-Brittle Transition
DNB	Departure from Nucleate Boiling
EDC	Expansion Due to Compression
EPRI	Electric Power Research Institute (USA)
ETR	Engineering Test Reactor (USA)
FGR	Fission gas Release
FWHM	Full Width at Half Maximum
HZP	Hot Zero Power
JAERI	Japan Atomic Energy Research Institute
JMTR	Japanese Material Test Reactor
LVDT	Linear Variable Differential Transformer
LWR	Light Water Reactor
MOX	Mixed Oxide (UO_2/PuO_2)
NFD	Nippon Nuclear Fuel Development
NRC	Nuclear Regulatory Commission (USA)
NSRR	Nuclear Safety Research Reactor (Japan)
PBF	Power Burst Facility (USA)
PCMI	Pellet-Clad Mechanical Interaction
PWR	Pressurized Water Reactor
REA	Rod Ejection Accident
RIA	Reactivity Initiated Accident
RXA	Recrystallization Annealed
SED	Strain Energy Density
SKI	Statens Kärnkraftinspektion (Swedish Nuclear Power Inspectorate)
SPERT	Special Power Excursion Reactor (USA)
SRA	Stress Relieved Annealed
TD	Theoretical Density

9 References

- Abe, T., Nakae, N., Kadato, K. and Matsumoto, M., 1992.
Failure behaviour of plutonium-uranium mixed oxide fuel under reactivity initiated accident condition,
J. Nucl. Mat. 188, pp 154-161.
- Agee, L.J., Dias A.F., Eisenhart, L.D. and Engel R.E., 1995.
Realistic scoping study of reactivity insertion accidents for a typical PWR and BWR core, Proc. CSNI specialist meeting on transient behaviour of high burnup fuel, Cadarache, France, September 12-14, 1995, pp 291-304.
- Anderson, T.L., 1995.
Fracture mechanics: fundamentals and applications, 2nd ed.,
CRC Press, Boca Raton, FL, USA.
- Andersson, T. and Wilson, A., 1979.
Ductility of Zircaloy canning tubes in relation to stress ratio in biaxial testing,
In: Zirconium in the nuclear industry; 4th international symposium, ASTM STP-681,
J.H. Schemel and T.P. Papazoglou (eds), American Society for Testing and Materials,
pp 60-71.
- Arsene, S., Bai, J.B. and Bompard, P. 2003.
Hydride embrittlement and irradiation effects on the hoop mechanical properties of pressurized water reactor (PWR) and boiling water reactor (BWR) Zircaloy cladding tubes: Part I. Hydride embrittlement in stress-relieved, annealed, and recrystallized Zircalloys at 20C and 300C,
Metallurgical and Materials Transactions A. 34A, pp 553-566.
- Bai, J.B., 1993.
Influence of an oxide layer on the hydride embrittlement in Zircaloy-4,
Scripta Metallurgica et Materialia, 29, pp 617-622.
- Balourdet, M. and Bernaudat C., 1995.
Tensile properties of Zircaloy-4 cladding submitted to fast transient loading,
Proc. CSNI specialist meeting on transient behaviour of high burnup fuel, Cadarache, France, September 12-14, 1995, pp 417-431.
- Balourdet, M., Bernaudat, C., Basini, V. and Hourdequin, N., 1999.
The PROMETRA programme: Assessment of mechanical properties of Zircaloy-4 fuel cladding during an RIA, Proc. 15th international conference on structural mechanics in reactor technology (SMiRT-15), August 15-20, 1999, Seoul, Korea.

Barba, M.J., 1880.
Mem. Soc. Ing Civils Part I, p 682.

Bates, D.W., Koss, D.A. and Motta, A.T., 2000.
Influence of specimen design on the deformation and failure of Zircaloy cladding,
Proc. ANS topical meeting on light water reactor fuel performance, Park City, Utah,
April 10-13, 2000.

Bertolino, G., Meyer, G. and Perez Ipina, J., 2003.
Effects of hydrogen content and temperature on fracture toughness of Zircaloy-4,
J. Nucl. Mat. 320, pp 272-279.

Chung, H.M., 2000.
Fundamental metallurgical aspects of axial splitting in zircaloy cladding,
Proc. ANS topical meeting on light water reactor fuel performance, Park City, Utah,
April 10-13, 2000.

Chung, H.M. and Kassner, T.F., 1998.
*Cladding metallurgy and fracture behavior during reactivity-initiated accidents at high
burnup*, Nucl. Engng. Design, 186, pp 411-427.

Cox, B., 1990.
Pellet-clad interaction (PCI) failures of zirconium alloy fuel cladding – a review,
J. Nucl. Mat. 172, pp 249-292.

Daum, R.S., Majumdar, S., Bates, D.W., Motta, A.T., Koss, D.A. and Billone, M.C.,
2002. *On the embrittlement of Zircaloy-4 under RIA-relevant conditions*,
In: Zirconium in the nuclear industry; 13th international symposium, ASTM STP-1423,
G.D. Moan and P. Rudling (eds), American Society for Testing and Materials, pp 702-
719.

del Barrio, M.T. and Herranz, L.E., 2002.
*Predictive methodology of a cladding failure criterion based on PROMETRA database:
Application to CABRI-CIP01 experiment*, Proc. EHPG meeting, September 8-13, Gol,
Norway. OECD Halden reactor project report HPR-359, Volume 2, Halden, Norway.

Diamond, D.J., Bromley, B.P. and Aronson, A.L., 2003.
Pulse width in a rod ejection accident,
Proc. of the NEA topical meeting on RIA fuel safety criteria, May 13-15, 2002, Aix-en-
Provence, France. Report NEA/CSNI/R(2003)8.

Federici, E., Lamare, F, Bessiron, V. and Papin, J., 2000.
*Status of the development of the SCANAIR code for the description of fuel behavior
under reactivity initiated accidents*, Proc. ANS topical meeting on light water reactor
fuel performance, Park City, Utah, April 10-13, 2000.

Forsberg, K. and Massih, A.R., 1990.
Redistribution of hydrogen in Zircaloy,
J. Nucl. Mat. 172, pp 130-134.

- Fujishiro, T., Yanagisawa, K., Ishijima, K. and Shiba, K., 1992.
Transient fuel behaviour of preirradiated PWR fuels under reactivity initiated accidents,
J. Nucl. Mat. 188, pp 162-167.
- Fuketa, T., 1999.
Experimental insights on high burnup PWR fuel behaviour during RIA,
Proc. of the 23rd NSRR technical review meeting, November 11-12, 1999, Tokyo, Japan.
- Fuketa, T., 2000.
High burnup BWR fuel response to reactivity transients and a comparison with PWR fuel response, Proc. of the 24th NSRR technical review meeting, November 13-14, 2000, Tokyo, Japan.
- Fuketa T., Nagase, F., Ishijima, K. and Fujishiro, T., 1996.
NSRR/RIA experiments with high-burnup PWR fuels,
Nucl. Safety 37(4), pp 328-342.
- Fuketa, T., Sasajima, H., Mori, Y. and Isjijima, K., 1997.
Fuel failure and fission gas release in high burnup PWR fuels under RIA conditions,
J. Nucl. Mat. 248, pp 249-256.
- Fuketa, T., Nakamura, T., Sasajima, H., Nagase, F., Uetsuka, H., Kikuchi, K. and Abe, T., 2000.
Behavior of PWR and BWR fuels during reactivity-initiated accident conditions,
Proc. ANS topical meeting on light water reactor fuel performance, Park City, Utah, April 10-13, 2000.
- Fuketa, T., Sasajima, H. and Sugiyama, T., 2001.
Behavior of high-burnup PWR fuels with low-tin Zircaloy-4 cladding under reactivity-initiated-accident conditions, Nucl. Technology, 133, pp 50-62.
- Fuketa, T., Sugiyama, T. Nakamura, T., Sasajima, H. and Nagase, F., 2003.
Effects of pellet expansion and cladding hydrides on PCMI failure of high burnup LWR fuel during reactivity transients, Nuclear safety research conference, October 21, 2003, Washington DC, USA.
- Garde, A.M., 1989.
Effects of irradiation and hydriding on the mechanical properties of Zircaloy-4 at high fluence, In: Zirconium in the nuclear industry; 8th international symposium, ASTM STP-1023, L.F.P. van Swam and C.M. Eucken (eds), American Society for Testing and Materials, pp 548-569.

Garde, A.M. 2000.

Influence of cladding microstructure on the low enthalpy failures in RIA simulation tests, In: Zirconium in the nuclear industry; 12th international symposium, ASTM STP-1354, G.P. Sabol and G.D. Moan (eds), American Society for Testing and Materials, pp 234-255.

Garde, A.M., Smith, G.P. and Pirek, R.C., 1996.

Effects of hydride precipitate localization and neutron fluence on the ductility of irradiated Zircaloy-4, In: Zirconium in the nuclear industry; 11th international symposium, ASTM STP-1295, E.R. Bradley and G.P. Sabol (eds), American Society for Testing and Materials, pp 407-430.

Garzarolli, F. and Holzer, R., 1992.

Waterside corrosion performance of light water power reactor fuel, Nucl. Energy, 31(1), pp 65-86.

Glasstone, S. and Sesonske, A., 1991.

Nuclear reactor engineering, 3rd ed., Krieger Publishing Company, Malabar, Florida, USA.

Grigoriev, V., Jakobsson, R., Schrire, D., Kesterson, R., Mitchell, D. and Pettersson, H., 2002. *Impact of corrosion on rapid deformation capabilities of ZIRLO cladding*, Proc. of the NEA topical meeting on RIA fuel safety criteria, May 13-15, 2002, Aix-en-Provence, France. Report NEA/CSNI/R(2003)8.

Hagman, D.L., Reymann, G.A. and Mason, R.E., 1981.

MATPRO-Version 11 (revision 2): A handbook of materials properties for use in the analysis of light water reactor fuel rod behavior, U.S. Nuclear Regulatory Commission report NUREG/CR-0497, August 1981.

In de Betou, J., Jernkvist, L.O., Massih, A.R., Rudling, P., Rönnerberg, G., Stepniewski, M. and Wiksell, G., 2004.

Assessment of burnup-dependent fuel rod failure threshold under reactivity-initiated accidents in light water reactors, Proc. ANS international meeting on light water reactor fuel performance, Orlando, Florida, September 19-22, 2004.

Ishijima, K. and Nakamura, T., 1996.

Transient elongation of a fresh fuel rod under reactivity initiated accident conditions, J. Nucl. Sci. Technology, 33(3), pp 229-238.

Ishikawa, M. and Shiozawa, S., 1980.

A study of fuel behaviour under reactivity initiated accident condition, J. Nucl. Mat. 95, pp 1-30.

Ishikawa, M., Fujishiro, T. and Kawasaki, S., 1989.

LWR fuel safety research with particular emphasis on RIA/LOCA and other conditions, J. Nucl. Sci. Engn. 26, pp 118-125.

- Jernkvist, L.O., 2003.
Prediction of failure of highly irradiated Zircaloy clad tubes under reactivity initiated accidents, Proc. 17th international conference on structural mechanics in reactor technology (SMiRT-17), August 17-22, 2003, Prague, Czech Republic.
- Jernkvist, L.O. and Massih, A.R., 2002.
Analysis of the effect of UO₂ high burnup microstructure on fission gas release, Swedish Nuclear Power Inspectorate (SKI) research report 02:56, October 2002.
- Kaplar, E., Yegorova, L., Lioutov, K., Konobeyev, A., Jouravkova, N., Smirnov, V., Goryachev, A., Prokhorov, V., Makarov, O., Yeremin, S. and Svyatkin, A., 2001.
Mechanical properties of unirradiated and irradiated Zr-1%Nb cladding: Procedures and results of low temperature biaxial burst tests and axial tensile tests, U.S. Nuclear Regulatory Commission report NUREG/IA-0199.
- Kuroda, M. and Yamanaka, S., 2002.
Assessment of the combined effects of irradiation and hydrogenation on the fracture behavior of Zircaloy fuel claddings by fracture mechanics, J. Nucl. Sci. Technology, 39(3), pp 234-240.
- Kuroda, M., Yamanaka, S., Nagase, F. and Uetsuka, H., 2001.
Analysis of the fracture behavior of hydrided fuel cladding by fracture mechanics, Nucl. Engng. Design, 203, pp 185-194.
- Lamare, F., 2001.
Personal e-mail communication, August 10, 2001.
- Lassmann, K., O'Carroll, C., van de Laar, J. and Walker, C.T., 1994.
The radial distribution of plutonium in high burnup UO₂ fuels, J. Nucl. Mat. 208, pp 223-231.
- Lemoine, F., 1997.
High burnup fuel behavior related to fission gas effects under reactivity initiated accidents (RIA) conditions, J. Nucl. Mat. 248, pp 238-248.
- Lespiaux, D., Noirot, J. and Menut, P., 1997.
Post-test examinations of high burnup PWR fuels submitted to RIA transients in the CABRI facility, Proc. ANS topical meeting on light water reactor fuel performance, Portland, Oregon, March 2-6, 1997, pp 650-658.
- Link, T.M., Koss, D.A. and Motta, A.T., 1997.
On the influence of an embrittled rim on the ductility of zircaloy cladding, Proc. ANS topical meeting on light water reactor fuel performance, Portland, Oregon, March 2-6, 1997, pp 634-642.
- Lucuta, P.G., Matzke, H.J. and Hastings, I.J., 1996.
A pragmatic approach to modelling thermal conductivity of irradiated UO₂ fuel: review and recommendations, J. Nucl. Mat. 232, pp 166-180.

MacDonald, P.E., Seiffert, S.L., Martinson, Z.R., McCardell, R.K., Owen, D.E. and Fukuda, S.K., 1980. *Assessment of light-water reactor fuel damage during a reactivity-initiated accident*, Nucl. Safety 21(5), pp 582-602.

Maki, H. and Ooyama, M., 1975.
Plastic deformation and fracture behavior of Zircaloy-2 fuel cladding tubes under biaxial stress, J. Nucl. Sci. Technology, 12(7), pp 423-435.

MATLAB, 2000.
Using MATLAB Version 6,
The MathWorks Inc. Natick, MA, USA.

Matzke, HJ., 1995.
The rim-effect in high burnup UO₂ nuclear fuel,
In P. Vincenzini (ed), *Ceramics: Charting the future*, Proc. world ceramics congress, Florence, Italy, June 28 – July 4, 1995, pp 2913-2920.

Meyer, R.O., McCardell, R.K. and Scott, H.B., 1997.
A regulatory assesement of test data for reactivity accidents,
Proc. ANS topical meeting on light water reactor fuel performance, Portland, Oregon, March 2-6, 1997, pp 729-744.

Montgomery, R., Rashid, Y., Dunham, R., Ozer, O., Yagnik, S. and Yang, R., 2004.
The mechanical response of cladding with a hydride lens under PCMI loading conditions, Proc. int. seminar on pellet-clad interaction in water reactor fuels (PCI-2004), Aix-en-Provence, France, March 9-11, 2004.

Nagase, F., Ishijima, K. and Furuta, T., 1995.
Influence of locally concentrated hydrides on ductility of Zircaloy-4,
Proc. CSNI specialist meeting on transient behaviour of high burnup fuel, Cadarache, France, September 12-14, 1995, pp 433-443.

Nakajima, T., Komatsu, I. and Yoshiki, R., 2002.
Three dimensional analysis of RIA in PWR and BWR with high burnup fuel, Proc. fuel safety research specialist's meeting, Tokai, Japan, March 4-5, 2002, pp 163-181.

Nakamura, T., 1999.
FK test series with high burnup BWR fuel and analytical test program,
Proc. of the 23rd NSRR technical review meeting, November 11-12, 1999, Tokyo, Japan.

Nakamura, T., Yoshinaga, M., Sobajima, M., Ishijima, K. and Fujishiro, T., 1994.
Boiling water reactor fuel behaviour at burnup of 26 MWd/kgU under reactivity-initiated accident conditions,
Nucl. Technology, 108, pp 45-59.

Nakamura, T., Sasajima, H., Fuketa, T. and Ishijima, K., 1996.
Fission gas induced cladding deformation of LWR fuel rods under reactivity initiated accident conditions, J. Nucl. Sci. Technology, 33(12), pp 924-935.

- Nakamura, T., Yoshinaga, M., Takahashi, M., Okonogi, K. and Isjijima, K., 2000.
Boiling water reactor fuel behavior under reactivity-initiated-accident conditions at burnup of 41 to 45 GWd/tonneU,
Nucl. Technology, 129, pp 141-151.
- Nakamura, T., Kusagaya, K. and Fuketa, T., 2002a.
High-burnup BWR fuel behavior under simulated reactivity-initiated accident conditions, Nucl. Technology, 138, pp 246-259.
- Nakamura, T., Sasajima, H., Yoshinaga, M. and Kusagaya, K., 2002b.
NSRR RIA tests on PWR, BWR and MOX fuel, Proc. fuel safety research specialist's meeting, Tokai, Japan, March 4-5, 2002, pp 71-83.
- Nam, C., Jeong, Y.H. and Jung, Y.H., 2001.
A statistical approach to predict the failure enthalpy and reliability of irradiated PWR fuel rods during reactivity-initiated accidents,
Nucl. Technology, 136, pp 158-168.
- Nogita, K. and Une, K., 1997.
Formation of pellet-cladding bonding layer in high burnup BWR fuels,
J. Nucl. Sci. Technology, 34(7), pp 679-686.
- Northwood, D.D. and Kosasih, U., 1983.
Hydrides and delayed hydrogen cracking in zirconium and its alloys,
Int. Metals Reviews, 28, pp 92-121.
- NRC, 2004.
An assessment of postulated reactivity-initiated accidents (RIAs) for operating reactors in the U.S., U.S. Nuclear Regulatory Commission report ML040920189.
- NUREG-0800, 1981.
Standard review plan for the review of safety analysis reports for nuclear power plants, LWR edition, section 4.2: Fuel system design, U.S. Nuclear Regulatory Commission report NUREG-0800, Rev. 2, Washington D.C.
- Papin, J., Rigat, H., Lamare, F. and Cazalis, B., 1997.
The SCANAIR code for the description of PWR fuel rod behaviour under RIA: Validation on experiments and extrapolation to reactor conditions,
Proc. ANS topical meeting on light water reactor fuel performance, Portland, Oregon, March 2-6, 1997, pp 659-666.
- Papin, J., Lemoine, F. and Federici, E., 2002.
Main outcomes from the CABRI test results, Proc. NEA CSNI topical meeting on RIA fuel safety criteria, Aix-en-Provence, France, May 13-15, 2002.
Report NEA/CSNI/R(2003)8/Vol 2, pp 61-81.

Pettersson, K. and Hellstrand, E., 1978.

Mechanical properties of Zircaloy-2 after a high-dose irradiation, Studsvik report MZ-78/110, Studsvik, Sweden.

Pettersson, K., Vesterlund, G. and Andersson, T., 1979.

Effect of irradiation on the strength, ductility, and defect sensitivity of fully recrystallized Zircaloy tube, In: *Zirconium in the nuclear industry; 4th international symposium*, ASTM STP-681, J.H. Schemel and T.P. Papazoglou (eds), American Society for Testing and Materials, pp 155-173.

Pierron, O.N., Koss, D.A., Motta, A.T. and Chan, K.S., 2003.

The influence of hydride blisters on the fracture of Zircaloy-4, J. Nucl. Mat. 322, pp 21-35.

Rashid, Y.R., Montgomery, R.O., Ozer, O., Yang, R., Yagnik, S. and Agee, L., 1995.

Evaluation of RIA experiments and their impact on high-burnup fuel performance, Proc. CSNI specialist meeting on transient behaviour of high burnup fuel, Cadarache, France, September 12-14, 1995, pp 471-492.

Rashid, Y.R., Montgomery, R.O., Lyon, W.F. and Yang, R., 2000.

A cladding failure model for fuel rods subjected to operational and accident transients, Proc. IAEA technical committee meeting on nuclear fuel behaviour modeling at high burnup and its experimental support, June 19-23, 2000, Windermere, UK.

RG-1.77, 1974.

Regulatory Guide 1.77 – Assumptions used for evaluating a control rod ejection accident for pressurized water reactors, US Atomic Energy Commission, 1974.

Sasajima, H., Fuketa, T., Nakamura, T., Nakamura, J. and Kikuchi, K., 2000.

Behavior of irradiated ATR/MOX fuel under reactivity initiated accidents conditions, J. Nucl. Sci. Technology, 37(5), pp 455-464.

Sawatzky, A., 1960.

Hydrogen in Zircaloy-2: Its distribution and heat of transport, J. Nucl. Mat. 2(4), pp 321-328.

Schmitz, F. and Papin, J., 1999.

High burnup effects on fuel behaviour under accident conditions: the tests CABRI REP-Na, J. Nucl. Mat. 270, pp 55-64.

SKI, 1995.

Ändrade gränser för härd- och kapslingskada vid analys av reaktivitetsolyckor, (In Swedish), SKI beslut 5.66-941618, Swedish Nuclear Power Inspectorate, Jan 18, 1995.

- Spino, J., Vennix, K. and Coquerelle, M., 1996.
Detailed characterization of the rim microstructure in PWR fuels in the burn-up range 40-67 GWd/tM, J. Nucl. Mat. 231, pp 179-190.
- Torimaru, T., Yasuda, T. and Nakatsuka, M., 1996.
Changes in mechanical properties of irradiated Zircaloy-2 fuel cladding due to short term annealing,
J. Nucl. Mat. 238(2-3), pp 169-174.
- Vitanza, C., 2002.
An analysis of the CABRI REP Na tests, Proc. NEA CSNI topical meeting on RIA fuel safety criteria, Aix-en-Provence, France, May 13-15, 2002.
Report NEA/CSNI/R(2003)8/Vol 2, pp 39-50.
- Waeckel, N., Bernaudat, C. and Salles, B., 2000.
EDF proposed safety domain for rod ejection accidents in a PWR,
Proc. ANS topical meeting on light water reactor fuel performance, Park City, Utah, April 10-13, 2000.
- Wallace, A.C., Shek, G.K. and Lepik, O.E., 1989.
Effects of hydride morphology on Zr-2.5%Nb fracture toughness, In: Zirconium in the nuclear industry; 8th international symposium, ASTM STP-1023, L.F.P. van Swam and C.M. Eucken (eds), American Society for Testing and Materials, pp 66-88.
- Wisner, S.B. and Adamson, R.B., 1998.
Combined effects of radiation damage and hydrides on the ductility of Zircaloy-2,
Nucl. Engng. Design, 185, pp 33-49.
- Yagnik, S.K., Hermann, A. and Kuo, R.C., 2004.
Ductility of Zircaloy fuel cladding at high burnup,
Proc. Zirconium in the nuclear industry, 14th international symposium, June 13-17, 2004, Stockholm, Sweden.
- Yanagisawa, K., Fujishiro, T., Negrini, A. and Franco, A., 1990.
Behavior of PCI-resistant additive fuel for BWR under reactivity initiated accident conditions,
J. Nucl. Sci. Technology, 27(1), pp 56-67.
- Yang, R., Montgomery, R.O. and Waeckel, N., 2003.
Revised reactivity initiated accident acceptance criteria for high burnup fuel,
Proc. European Nuclear Society ENS TopFuel-2003 conference, March 16-19, 2003, Wurzburg, Germany.
- Yasuda, T., Nakatsuka, M. and Yamashita, K., 1987.
Deformation and fracture properties of neutron-irradiated recrystallized Zircaloy-2 cladding under uniaxial tension, In: Zirconium in the nuclear industry; 7th international symposium, ASTM STP-939, R.B. Adamson and L.F.P. van Swam (eds), American Society for Testing and Materials, pp 737-747.

Yunchang, F. and Koss, D.A., 1985.

The influence of multiaxial states of stress on the hydrogen embrittlement of zirconium alloy sheet, Metallurgical Transactions A. 16A, pp 675-681.

Yvon, P., Catherine, C.S., Duguay, C., Hourdequin, N., Carassou, S., Cazalis, B. and Bernaudat, C., 2001.

Development of new techniques to assess the mechanical behaviour of Zircaloy-4 during an RIA, Proc. IAEA technical committee meeting on fuel behaviour under transient and LOCA conditions, September 10-14, 2001, Halden, Norway.

IAEA technical report IAEA-TECDOC-1320, 2002, pp 111-122.

Appendix A: Pulse reactor test data

A.1 SPERT-CDC tests

The total deposited energies for the pre-irradiated test rods in SPERT-CDC, along with their respective burnups, are presented in table A.1. The energy deposition was determined by measuring the activity of a cobalt wire located in the vicinity of the test capsule. The technique provides the total energy deposition during the transient and has an accuracy of $\pm 12\%$. Around 10 to 20 % of the energy deposition occurs after the power pulse, i.e. during low powers prior to reactor scram. This delayed energy deposition does not contribute to the peak fuel enthalpy. The radially averaged peak fuel enthalpy, H_p , was therefore estimated using a correction of 17% to account for the delayed energy deposition (MacDonald et al., 1980).

Several of the low-burnup rods failed during or following the power pulse. Also, both of the failed high-burnup rods (rods 756 and 859) exhibited brittle-type clad fracture. Rod 756 failed at $H_p = 599 \text{ Jg}^{-1}$, whereas rod 859 failed at $H_p = 356 \text{ Jg}^{-1}$. A large hydride blister was found in rod 859. The cause of failure for these two rods was attributed to heavy accumulations of zirconium hydride. Moreover, the non-prototypical test conditions could also have contributed to the cladding failure. The cold initial cladding temperatures in combination with the narrow power pulses, which were utilised in the SPERT-CDC tests, resulted in relatively low cladding temperatures at the time of maximum cladding stresses; see section 3.3.1.

Test ID	Fuel burnup [MWdkg ⁻¹ U ⁻¹]	Pulse width [ms]	Energy deposition [Jg ⁻¹]	Peak fuel enthalpy [Jg ⁻¹]	Failure enthalpy [Jg ⁻¹]	Fuel dispersal
571	4.55	31	674	574	Survived	-
568	3.84	24	833	674	615	Yes
567	3.10	18	1105	896	896	Yes
569	4.14	14	1457	1181	1181	Yes
703	1.14	15	804	682	Survived	-
709	0.99	13	996	846	846	Yes
685	13.1	27	779	662	Survived	-
684	12.9	20	837	712	Survived	-
756	32.7	17	737	599	599	No
859	31.8	16	795	645	356	No

Table A.1: SPERT-CDC tests on pre-irradiated fuel rods. Data compiled from MacDonald et al. (1980) and Meyer et al. (1997).

The applicability of the SPERT-CDC test results to LWR conditions must be questioned, since the conditions for the test rods before transient testing were not representative of those for LWR fuel. The rods were pre-irradiated in the ETR facility at very high linear heat generation rate, 46-67 kWm⁻¹, resulting in fuel restructuring and central hole formation. Hence, these tests are not typical of fuel rods in commercial light water reactors.

A.2 PBF tests

The main objective of the RIA 1-1 tests was to provide a comparison of irradiated and un-irradiated fuel behaviour using two pairs of Saxton (PWR) rods at the US NRC licensing fuel enthalpy limit of 280 calg⁻¹ (1172 Jg⁻¹) UO₂. Two of the rods were pre-irradiated in Saxton to a burnup of 4.6 MWdkg⁻¹U⁻¹, and these rods failed by rod fragmentation and fuel dispersal at $H_p = 1193$ Jg⁻¹ (285 calg⁻¹). See table A.2.

The RIA 1-2 tests were conducted using four individually shrouded fuel rods, which had been irradiated up to a burnup of 5.2 MWdkg⁻¹U⁻¹ in the Saxton reactor. Two of the rods were opened and back-filled to about 2.4 MPa to simulate end-of-life rod internal pressure. One rod was opened, instrumented and back-filled to a rod internal pressure of 0.105 MPa. The four fuel rods used in tests RIA 1-2 were subjected to a radially averaged peak fuel enthalpy of $H_p = 775$ Jg⁻¹ (185 calg⁻¹).

Test	Rod ID	Fuel burnup [MWdkg ⁻¹ U ⁻¹]	Pulse width [ms]	Energy deposition [Jg ⁻¹]	Peak fuel enthalpy [Jg ⁻¹]	Failure enthalpy [Jg ⁻¹]	Fuel dispersal
RIA 1-1	801-1	4.6	13	1528	1193	1193	Yes
	801-2	4.7	13	1528	1193	1193	Yes
	801-3	0.0	13	1528	1193	1193	No
	801-4	0.0	13	1528	1193	1193	No
RIA 1-2	802-1	5.2	16	1005	775	Survived	-
	802-2	5.1	16	1005	775	Survived	-
	802-3	4.4	16	1005	775	586	No
	802-4	4.5	16	1005	775	Survived	-
RIA 1-4	804-1	6.1	11	1235	1160	<<1160	No
	804-3	5.5	11	1235	1160	<<1160	No
	804-7	5.9	11	1235	1160	<<1160	No
	804-9	5.7	11	1235	1160	<<1160	No
	804-10	4.4	11	1130	1068	<<1068	No
	804-4	5.0	11	1130	1068	<<1068	No
	804-6	5.1	11	1130	1068	<<1068	No
	804-8	4.7	11	1130	1068	<<1068	No
	804-5	5.5	11	1026	980	980	No

Table A.2: Summary of PBF tests. Data compiled from MacDonald et al. (1980) and Meyer et al. (1997).

Only one rod failed in the RIA 1-2 experiment. The failure was caused by 22 small (<1 cm long) longitudinal cracks, starting at about 14.5 cm and extending to about 68.1 cm from the bottom of the 91 cm long fuel stack. The radial average fuel enthalpy at the 14.5 and 68.1 cm locations was about 586 Jg^{-1} . This failed rod had a burnup of $4.4 \text{ MWdkg}^{-1}\text{U}^{-1}$, and was not opened for re-pressurisation and instrumentation. It should also be mentioned that this rod was not pre-pressurised with helium, but was air filled at atmospheric pressure.

Significant differences were observed between the two intact rods with high internal pressure and the intact low-pressure rod. The maximum hoop plastic strain for the high-pressure rods was twice that of low-pressure rods; the maximum cladding hoop plastic strain measured in the two high-pressure rods was about 6 % whereas for the low-pressure rod, it was around 3 %. Moreover, more pronounced clad ridging was observed for the high-pressure rods, at intervals equal to the length of fuel pellets.

The nine rods in test RIA 1-4 were ramped to $H_p = 980 - 1160 \text{ Jg}^{-1}$ and all of them failed by PCMI-induced cracks.

A.3 NSRR tests

A.3.1 Tests on PWR fuel rods

A.3.1.1 MH and GK rods

The MH and GK test series consisted of altogether five PWR 14×14-test rods. They were subjected to power pulses, yielding H_p from 196 to 389 Jg^{-1} , as shown in table A.3. All the test rods survived the transients. During the power pulse, prompt cladding axial displacement was observed, indicating the occurrence of PCMI. The maximum axial displacement was reached 5 to 10 ms after the peak power and then decreased after 5 s to its equilibrium position. Cladding surface temperature was increased to saturation temperature (100 °C) and nucleate boiling condition did occur for a few seconds.

Cladding dimensional changes were measured after testing. Plastic hoop strains were found in rods where $H_p \geq 230 \text{ Jg}^{-1}$ (55 calg^{-1}), with the maximum value of 2.3 % for rod GK-1, which had experienced $H_p = 389 \text{ Jg}^{-1}$. In table A.4, we list the recorded strains for these rods.

All the test rods experienced considerable fission product gas release, which contributed to a 4 to 8 MPa pressure increase in the rods. Fission product gas release fraction determined by rod puncturing ranged between 0.04 and 0.13 during the transient, as shown in table A.4. Destructive examination of fuel pellet material revealed cracks extending through a 1 mm thick rim at the pellet surface.

A.3.1.2 OI and HBO rods

Four rods in the OI series and 7 rods in the HBO series (all of 17×17 design) were subjected to power pulses with H_p ranging from 155 to 657 Jg^{-1} , as shown in table A.3. Three of the rods, HBO-1, HBO-5 and OI-11, failed during the transient. The failure enthalpies for these rods were 251, 322 and 502 Jg^{-1} , respectively.

The tests OI-10 and OI-11 were carried out in July 2003, and these test rods had two different niobium alloy claddings: OI-10 had Mitsubishi Developed Alloy (MDA), whereas OI-11 had ZIRLO cladding. The results from these tests, survival of OI-10 and very high failure enthalpy for OI-11, reflect the better performance of these cladding materials in terms of corrosion and lower hydrogen uptake under in-reactor irradiation.

Dimensional measurements carried out after testing showed cladding plastic deformation. The residual hoop cladding strains for the OI-1 and OI-2 rods were above 1 %. For the surviving HBO rods, the strains varied from 0.2 to 2.1 %; see table A.4. Fission product gas release during the transient was determined by rod puncturing. The release fractions for the HBO rods varied from 0.08 to 0.23 during the transient. The corresponding value determined for OI-2 was 0.102, as shown in table A.4.

Test ID	Design	Fuel burnup [MWdkg ⁻¹ U ⁻¹]	Pulse width [ms]	Peak fuel enthalpy [Jg ⁻¹]	Failure enthalpy [Jg ⁻¹]	Fuel dispersal
MH-1	14×14	38.9	5.6	196	Survived	-
MH-2	14×14	38.9	5.5	230	Survived	-
MH-3	14×14	38.9	4.4	281	Survived	-
GK-1	14×14	42.1	4.6	389	Survived	-
GK-2	14×14	42.1	4.6	377	Survived	-
OI-1	17×17	39.2	4.4	444	Survived	-
OI-2	17×17	39.2	4.4	453	Survived	-
OI-10	17×17	60	5.6	435	Survived	
OI-11	17×17	58	4.4	657	502	N/A
HBO-1	17×17	50.4	4.4	306	251	Yes
HBO-2	17×17	50.4	6.9	155	Survived	-
HBO-3	17×17	50.4	4.4	310	Survived	-
HBO-4	17×17	50.4	5.3	209	Survived	-
HBO-5	17×17	44	4.4	334	322	No
HBO-6	17×17	49	4.4	356	Survived	-
HBO-7	17×17	49	4.4	368	Survived	-
TK-1	17×17	38	4.3	527	Survived	-
TK-2	17×17	48	4.3	448	251	Yes
TK-3	17×17	50	4.3	414	Survived	-
TK-4	17×17	50	4.3	410	Survived	-
TK-5	17×17	48	4.3	423	Survived	-
TK-6	17×17	38	4.3	523	Survived	-
TK-7	17×17	50	4.3	398	360	Yes
TK-8	17×17	50	7.0	272	Survived	-
TK-9	17×17	50	4.4	414	Survived	-
TK-10	17×17	46	4.4	360	Survived	-

Table A.3: Summary of NSRR tests on pre-irradiated PWR rods. N/A: Not available. Data compiled from NRC (2004), Fuketa (1999) and Fuketa et al. (1996, 1997, 2001 and 2003).

Cladding failure modes for the HBO-1 and HBO-5 rods have been discussed in some detail by Fuketa et al. (1997). In these two rods, axial cracks in the cladding were over the entire active length of the rod. The fracture is attributed to hydride-induced embrittlement. Significant hydride deposition below the oxide film on the cladding outer surface and many small cracks, perpendicular to the surface, were observed; see figure 3.4 in section 3.4.2. In HBO-5, local spallation of the clad oxide was observed. In both HBO-1 and HBO-5, the main crack emanated from one of these small cracks and then propagated through the hydride layer and the remaining part of the clad wall. According to Fuketa et al. (1997), fuel failure occurred in experiments with test fuel rodlets taken from the uppermost sections of the parent rod. Micro-crack generation in the oxide and hydride layer is more likely observed in specimens taken from the higher axial segments of the fuel rod, where the oxide layer is thickest.

Test ID	Design	Fuel burnup [MWdkg ⁻¹ U ⁻¹]	Peak fuel enthalpy [Jg ⁻¹]	Failure enthalpy [Jg ⁻¹]	Hoop strain [%]	FGR fraction [-]
MH-1	14×14	38.9	197	Survived	0.0	0.035
MH-2	14×14	38.9	230	Survived	0.2	N/A
MH-3	14×14	38.9	281	Survived	1.7	0.04
GK-1	14×14	42.1	389	Survived	2.3	0.128
GK-2	14×14	42.1	377	Survived	1.1	0.07
OI-1	17×17	39.1	444	Survived	1.3	N/A
OI-2	17×17	39.1	452	Survived	4.5	0.102
OI-10	17×17	60	435	Survived	0.7	N/A
OI-11	17×17	58	657	502	-	-
HBO-1	17×17	50.4	306	251	-	-
HBO-2	17×17	50.4	155	Survived	0.4	0.177
HBO-3	17×17	50.4	310	Survived	1.5	0.227
HBO-4	17×17	50.4	209	Survived	0.2	0.211
HBO-5	17×17	44	334	322	-	-
HBO-6	17×17	49	356	Survived	1.1	0.10
HBO-7	17×17	49	368	Survived	2.1	0.085
TK-1	17×17	38	528	Survived	25	0.2
TK-2	17×17	48	448	251	-	-
TK-3	17×17	50	414	Survived	5.6	0.109
TK-4	17×17	50	410	Survived	4.2	0.08
TK-5	17×17	48	423	Survived	4.2	0.12
TK-6	17×17	38	523	Survived	15.5	0.16
TK-7	17×17	50	398	360	-	-
TK-8	17×17	50	272	Survived	0.3	0.08
TK-9	17×17	50	414	Survived	14.6	0.062
TK-10	17×17	46	360	Survived	N/A	N/A

Table A.4: Summary of data on clad hoop plastic strain and fission gas release from NSRR tests on pre-irradiated PWR rods. Data compiled from NRC (2004), Fuketa (1999), Fuketa et al. (1996,1997, 2001 and 2003), Fujishiro et al. (1992) and Nakamura et al. (2002b).

Fuel dispersion occurred only in HBO-1, according to Fuketa et al. (1997). After testing, all the fuel pellets were found as finely fragmented fuel pieces, half of them with sizes smaller than 50 μm . In HBO-5, most of the fuel remained inside the cladding tube, and only a very small amount of fuel powder was released to the coolant water.

A.3.1.3 TK rods

Among the ten rods tested so far in the TK series, two rods, TK-2 and TK-7, failed at 251 and 360 Jg^{-1} , respectively, (Fuketa, 1999) and (Fuketa et al., 2000). Dimensional measurements of the cladding after testing showed plastic deformations. The clad plastic hoop strains for the intact rods varied from 0,3 to 25 %, as shown in table A.4.

Fission product gas release, determined by rod puncturing, showed that the release fractions for the TK rods were between 0.06 and 0.20 during the transient. The cladding cracks in the failed rods TK-2 and TK-7 started at the clad outer surface, in the oxide layer and the heavily hydrided region, and propagated through the clad wall. Axial cracking occurred over the fuel active length and had a zigzag appearance. Fuel dispersion occurred in both TK-2 and TK-7.

A.3.2 Tests on BWR fuel rods

A.3.2.1 TS rods

In the TS series, five BWR test rods were subjected to peak fuel enthalpies between 230 and 410 Jg^{-1} , as shown in table A.5. The here presented data are taken from Nakamura et al. (1994). All the rods survived the transient testing. A summary of clad strain and fission gas release data is presented in table A.6. Two of the rods, TS-4 and TS-5, experienced limited PCMI with small plastic deformation of the cladding. Finally, rod puncturing indicated that the fission gas release fraction during the transients ranged from 0.08 to 0.15.

Destructive examination of the TS-4 fuel pellets revealed the presence of numerous small radial cracks in the outer periphery, which extended inward to about 3/4 of the pellet radius. In addition to radial cracks, a thin layer ($\approx 100 \mu\text{m}$), which contained extensive grain boundary separation, was identified from a secondary electron microscopy of the surface layer (Nakamura et al., 1994). It was judged that these effects were due to a large temperature gradient, occurring during the transient.

A.3.2.2 FK rods

As shown in table A.5, a total of eleven BWR rods in the FK series have been tested in the NSRR so far. For these rods, the peak fuel enthalpies ranged from 293 to 607 Jg^{-1} and the average oxide layer thicknesses were below 40 μm , (Fuketa, 2000), (Fuketa et al., 2000), (Nakamura, 1999) and (Nakamura et al., 2002a). The clad tubes of rods FK-4 to FK-12 were equipped with zirconium liner, which was about 0.1 mm thick.

Five rods, FK-6, FK-7, FK-9, FK-10 and FK-12, failed during the power excursion at fuel enthalpies of 293, 260, 360, 335 and 301 Jg^{-1} , respectively. A summary of clad strain and fission gas release data is presented in table A.6.

Clad plastic deformation was observed in three of the rods, where the hoop plastic strain ranged from 0.85 to 1.5 %. Fission product gas release, determined by rod puncturing, showed that the release fraction during these FK tests varied between 0.03 and 0.17.

Destructive examination of the fuel pellets in rod FK-4, as in the TS series, showed the occurrence of numerous small radial cracks in the outer periphery, which extended inward to about 3/4 of pellet radius (Nakamura, 1999). Moreover, circumferential cracks were observed in the FK-4 pellet. The clad tubes of the failed test rods FK-6 and FK-7 were broken apart into three pieces and all of the fuel pellets were finely fragmented and dispersed into the capsule water. About half of the fuel pellets turned into particles smaller than 0.1 mm.

It is regarded that the wider pellet-to-cladding gap due to slow clad creep down in BWRs could lead to milder loads on the cladding during PCMI than in PWRs. Nevertheless, according to Nakamura et al. (2002a), in the test rods FK-6 through FK-9 at a burnup of $61 \text{ MWdkg}^{-1}\text{U}^{-1}$, extensive bonding between the Zr-liner and the fuel pellets had occurred, and the pellet-to-cladding gap was completely closed before the pulse irradiation. The results of these tests indicate intense PCMI loading of the cladding due to the bonding. We should also mention that the clad tubes in the failed BWR test rods had relatively low through-wall average hydrogen concentrations, <220 wppm according to Nakamura et al. (2002a). However, cracks had originated in the cladding outer region and then propagated along hydride platelets. The cracks in the inner part of the clad wall had a ductile appearance.

Test ID	Design	Fuel burnup [$\text{MWdkg}^{-1}\text{U}^{-1}$]	Pulse width [ms]	Peak fuel enthalpy [Jg^{-1}]	Failure enthalpy [Jg^{-1}]	Fuel dispersal
TS-1	7×7	26	6.7	230	Survived	-
TS-2	7×7	26	6.2	276	Survived	-
TS-3	7×7	26	5.6	368	Survived	-
TS-4	7×7	26	5.0	352	Survived	-
TS-5	7×7	26	4.5	410	Survived	-
FK-1	8×8	45	4.4	544	Survived	-
FK-2	8×8	45	5.3	293	Survived	-
FK-3	8×8	41	4.4	607	Survived	-
FK-4	8×8	56	4.4	586	Survived	-
FK-5	8×8	56	7.3	293	Survived	-
FK-6	8×8	61	4.3	548	293	Yes
FK-7	8×8	61	4.3	540	260	Yes
FK-8	8×8	61	7.3	272	Survived	-
FK-9	8×8	61	5.7	377	360	Yes
FK-10	8×8	61	5.1	431	335	No
FK-12	8×8	61	5.8	373	301	No

Table A.5: Summary of NSRR tests on pre-irradiated BWR rods. Data compiled from Nakamura (1999), Fuketa et al. (2000), NRC (2004) and Nakamura et al. (1994 and 2002a).

Test ID	Design	Fuel burnup [MWdkg ⁻¹ U ⁻¹]	Peak fuel enthalpy [Jg ⁻¹]	Failure enthalpy [Jg ⁻¹]	Axial strain [%]	Hoop strain [%]	FGR fraction [-]
TS-1	7×7	26	230	Survived	N/A	N/A	N/A
TS-2	7×7	26	276	Survived	0.2	N/A	0.12
TS-3	7×7	26	368	Survived	0.04	N/A	0.10
TS-4	7×7	26	352	Survived	0.41	N/A	0.15
TS-5	7×7	26	410	Survived	0.44	0.0	0.08
FK-1	8×8	45	544	Survived	1.1	0.85	0.082
FK-2	8×8	45	293	Survived	0.3	0.0	0.031
FK-3	8×8	41	607	Survived	0.9	1.5	0.047
FK-4	8×8	56	586	Survived	0.8	1.25	0.157
FK-5	8×8	56	293	Survived	0.36	0.0	0.096
FK-6	8×8	61	548	293	N/A	< 0.1	0.169
FK-7	8×8	61	540	260	N/A	< 0.1	0.17
FK-8	8×8	61	272	Survived	N/A	< 0.02	0.113
FK-9	8×8	61	377	360	N/A	N/A	0.166
FK-10	8×8	61	431	335	N/A	N/A	N/A
FK-12	8×8	61	373	301	N/A	N/A	N/A

Table A.6: Summary of data on clad total axial strain, clad hoop plastic strain and fission gas release from NSRR tests on pre-irradiated BWR rods. Data compiled from Nakamura (1999), Fuketa et al. (2000), NRC (2004) and Nakamura et al. (1994 and 2002a).

A.3.3 Tests on JMTR fuel rods

A total of 22 JMTR rods have been tested in the NSRR to peak fuel enthalpies ranging from 352 to 921 Jg⁻¹, as shown in table A.7. The larger fuel enthalpies in this series were achieved by increasing the ²³⁵U enrichment to 10 or 20% in the test rods. Due to the high enrichment and the fact that pre-irradiation took place in an un-pressurized, non-oxidizing helium environment, the JMTR fuel rods are not representative for LWR fuel (Fuketa et al., 1997). However, the JMTR fuel rods were better instrumented than the test rods that were pre-irradiated in commercial LWRs, and they are therefore still of interest.

The in-reactor instrumentation for the JMTR series included linear variable differential transformers (LVDTs) for recording fuel and cladding axial displacements, and thermocouples for measuring cladding surface temperature, and also a device to monitor capsule pressure. However, the axial displacements could not be determined in a majority of the tests due to malfunctions in LVDTs. Consequently, the data are limited to only one rod, JM-3, which was tested at $H_p = 553 \text{ Jg}^{-1}$. For this particular rod, the maximum fuel and cladding axial displacements were 1.14 mm and 0.36 mm, respectively.

Pressure pulses in the capsule were only observed for two failed rods, JM-14 and JMH-3. These rods had large wide-open cracks in the cladding, causing fuel dispersion. Dimensional measurements after the tests revealed significant PCMI for all the JMTR test rods. The plastic hoop strain showed a strong dependence on pulse magnitude above 628 Jg^{-1} . For $H_p < 628 \text{ Jg}^{-1}$, the cladding hoop strain remained below 1%.

Two failure modes were identified: (i) multiple through-wall cracks less than 10 mm long, which occurred in the vicinity of hydride blisters and (ii) a single long axial crack extending over the active fuel region. Destructive examinations revealed that the cracks initiated in hydride blisters on the outer surface of the cladding, and then propagated inward toward the inner surface. The cracks in the hydride blisters had morphology of brittle fracture, whereas in the metal, the fracture was ductile. Part-wall cracks, arrested in the ductile Zircaloy-4 underneath the blisters, were also observed at several of the hydride blisters.

Test ID	Design	Fuel burnup [$\text{MWdkg}^{-1}\text{U}^{-1}$]	Pulse width [ms]	Peak fuel enthalpy [Jg^{-1}]	Failure enthalpy [Jg^{-1}]	Fuel dispersal
JM-1	14×14	21.6	9.0	385	Survived	-
JM-2	14×14	26.7	9.0	352	Survived	-
JM-3	14×14	19.6	7.8	553	Survived	-
JM-4	14×14	21.2	5.5	741	741	No
JM-5	14×14	25.7	5.6	699	682	No
JM-6	14×14	14.7	7.1	653	Survived	-
JM-7	14×14	12.6	7.8	611	Survived	-
JM-8	14×14	19.5	7.2	674	Survived	-
JM-9	14×14	25	6.8	628	Survived	-
JM-10	14×14	21	5.6	837	Survived	-
JM-11	14×14	31	6.3	670	Survived	-
JM-12	14×14	38	5.3	754	653	No
JM-13	14×14	38	6.3	628	Survived	-
JM-14	14×14	38	6.0	670	515	Yes
JM-15	14×14	31	6.5	586	Survived	-
JM-16	14×14	38	6.4	544	Survived	-
JMH-1	14×14	22	8.3	628	Survived	-
JMH-2	14×14	22	6.8	795	Survived	-
JMH-3	14×14	30	6.2	921	858	Yes
JMH-5	14×14	30	6.2	921	791	Yes
JMH-4	14×14	30	7.9	628	Survived	-
JMN-1	14×14	22	7.1	628	486	No

Table A.7: Summary of NSRR tests on JMTR fuel rods. Data compiled from Fujishiro et al. (1992), NRC (2004) and Nam et al. (2001)

A.4 CABRI REP-Na tests

The REP-Na test rods in CABRI experienced peak fuel enthalpies ranging from about 400 to 950 Jg⁻¹ during the RIA simulations. Four of the rods failed the tests, among which one was a MOX fuel rod. The failure enthalpies varied between 126 and 502 Jg⁻¹. Test rod Na-1, with a burnup of 64 MWdkg⁻¹U⁻¹, failed at 126 Jg⁻¹ which is the lowest failure enthalpy ever recorded in RIA tests. This rod had also one of the highest burnups among the CABRI test rods, and also among all test rods in the various aforementioned RIA test programs. Recently, the extremely low failure enthalpy reported for rod Na-1 has been questioned (Vitanza, 2002), and the experiment is currently re-evaluated in order to confirm the correctness of the reported results. We have summarised the main result of the CABRI REP-Na tests in tables A.8 and A.9.

Dimensional measurements after testing showed clad plastic deformations by PCMI during the transient. The clad hoop plastic strain for the intact rods varied between 0.37 and 7.4 %, as shown in table A.9. Fission product gas release fractions, determined by rod puncturing, were between 0.055 and 0.34 during the transient.

Test ID	Fuel type	Fuel burnup [MWdkg ⁻¹ U ⁻¹]	Pulse width [ms]	Peak fuel enthalpy [Jg ⁻¹]	Failure enthalpy [Jg ⁻¹]	Fuel dispersal	Clad oxide thickness [μm]
Na-1	UO ₂	63.8	9.5	460	126	Yes	80, spalled
Na-2	UO ₂	33	9.1	882	Survived	-	4
Na-3	UO ₂	52.8	9.5	502	Survived	-	40
Na-4	UO ₂	62.3	75	404	Survived	-	80
Na-5	UO ₂	64.3	9.5	439	Survived	-	20
Na-6	MOX	47	35	690	Survived	-	40
Na-7	MOX	55	40	732	502	Yes	50
Na-8	UO ₂	60	75	443	343	No	130, spalled
Na-9	MOX	28	34	953	Survived	-	< 20
Na-10	UO ₂	62	31	461	331	No	80, spalled
Na-11	UO ₂	63.4	31	461	Survived	-	15
Na-12	MOX	65	63	456	Survived	-	80

Table A.8: Summary of CABRI REP-Na tests on PWR fuel rods. Data compiled from Schmitz & Papin (1999) and Papin et al. (2002).

The cladding of rod Na-1 had spalled oxide, with a strongly non-uniform hydride distribution. Cracks initiated at the cladding outer surface in the spalled oxide and heavily hydrided region, and then propagated inward through the cladding wall.

The failure at $H_p = 502$ Jg⁻¹ of the Na-7 MOX fuel rod, which was irradiated to 55 MWdkg⁻¹U⁻¹, cannot be attributed to oxide layer spallation and/or excessive hydriding. The oxide layer thickness was around 50 μm, with no sign of spallation prior to the pulse reactor test. Therefore, Schmitz and Papin (1999) concluded that the failure was due to transient gaseous swelling, which is more pronounced in MOX than in UO₂ fuel.

The Na-8 test was performed on a rod with standard Zircaloy-4 cladding, irradiated to 60 MWdkg⁻¹U⁻¹ in a PWR. The cladding was severely oxidized (locally spalled) and hydrided. The power pulse applied in the RIA test was 75 ms wide, and the cladding failed at $H_p = 343 \text{ Jg}^{-1}$ with no fuel dispersal. Post-test examination of the rod revealed long axial cracks, which initiated in the heavily hydrided region of the clad outer rim and then propagated radially through the cladding wall. According to Waeckel et al. (2000), the cracks had propagated axially and opened during the cool-down phase of the test, due to residual thermal stresses in the cladding.

Test ID	Clad material	Fuel burnup [MWdkg ⁻¹ U ⁻¹]	Peak fuel enthalpy [Jg ⁻¹]	Failure enthalpy [Jg ⁻¹]	Hoop strain [%]	FGR fraction [-]
Na-1	Standard Zr-4	63.8	460	126	-	-
Na-2	Standard Zr-4	33	882	Survived	3.5	0.055
Na-3	Low-tin Zr-4	52.8	502	Survived	2.1	0.137
Na-4	Standard Zr-4	62.3	404	Survived	0.37	0.083
Na-5	Standard Zr-4	64.3	439	Survived	1.11	0.151
Na-6	Standard Zr-4	47	690	Survived	3.2	0.216
Na-7	Standard Zr-4	55	732	502	-	-
Na-8	Standard Zr-4	60	443	343	-	-
Na-9	Low-tin Zr-4	28	953	Survived	7.4	0.34
Na-10	Standard Zr-4	62	461	331	-	-
Na-11	M5	63.4	461	Survived	N/A	N/A
Na-12	Standard Zr-4	65	456	Survived	N/A	N/A

Table A.9: Summary of data on clad hoop plastic strain and fission gas release in CABRI REP-Na tests on PWR rods. Data compiled from Schmitz & Papin (1999) and Papin et al. (2002).

Finally, test Na-10 was made on a rod irradiated to a burnup of 62 MWdkg⁻¹U⁻¹. The rod was taken from the same fuel assembly as rod Na-1, and consequently had the same pre-irradiation power history. Rod Na-10 was subjected to a 31 ms power pulse, with a deposited energy of 461 Jg⁻¹. The cladding failed at $H_p = 331 \text{ Jg}^{-1}$ with no fuel dispersal. Post-test examination of the rod showed only one small crack, about 70 mm long, located in the peak power region of the rod.

Appendix B: Mechanical property test data

B.1 Zircaloy-2 clad material

B.1.1 NFD tests

A series of 22 axial tension tests was performed on irradiated Zircaloy-2 RXA cladding at the Nippon Nuclear Fuel Development (NFD) Company in Japan (Yasuda et al., 1987). Five tests were also made on un-irradiated cladding tubes of the same material.

The material was irradiated to fast neutron fluences of $6.0 \times 10^{23} - 3.6 \times 10^{25} \text{ m}^{-2}$ ($E \geq 1 \text{ MeV}$) in two different ways:

- 12 tube samples (denoted ZS) were irradiated as usual fuel rod cladding for 5 cycles in a commercial BWR. After irradiation, the maximum clad oxide layer thickness was 20 μm , and the maximum hydrogen concentration was 50 wppm. The inner and outer diameters of these samples were 10.80 and 12.52 mm, respectively
- 10 tube samples (denoted NK) were irradiated in a He-filled capsule within a BWR, and they therefore experienced negligible oxidation and hydrogen pickup. These tube samples were not charged with fuel pellets, and their inner and outer diameters were 12.42 and 14.30 mm, respectively.

Both type of tube samples were 135 mm long, and the gage length used in axial tension tests was 50 mm. The applied strain rate was $8.33 \times 10^{-5} \text{ s}^{-1}$. The testing conditions and results for all samples are given in table B.1. The clad oxide thickness and hydrogen content for the NK samples were not explicitly given by Yasuda et al. (1987), but have been estimated from the reported maximum values, assuming proportionality with fast neutron fluence.

B.1.2 Dataset A

Dataset A contains confidential data from tests carried out within program IV of the Nuclear Fuel Industry Research Group (NFIR-IV).

B.1.3 Studsvik tests

Six burst tests on un-irradiated Zircaloy-2 tubes, performed in Studsvik, Sweden, are included in the database (Pettersson & Hellstrand, 1978) and (Pettersson et al., 1979). Tests on irradiated samples were also reported in these studies, but they were not included in the database, since the samples were irradiated to low neutron doses under non-prototypical irradiation conditions in the R2 experiment reactor in Studsvik.

Moreover, the spread in reported failure strain data for irradiated samples in these studies is striking. As reported in the original papers, the spread is probably connected with inadequate temperature control under testing.

The un-irradiated samples included in the database are standard Zircaloy-2 clad tubes in RXA condition, which were subjected to 80 % reduction in the final cold rolling, followed by a final annealing at 848 K (575 °C) under 1.5 hour. All tests were performed at 563 K, with a hoop strain rate of $2.0 \times 10^{-4} \text{ s}^{-1}$.

The test conditions and results for all samples are given in table B.2.

Test temperature [K]	Fast fluence $\times 10^{25}$ [m^{-2}]	Clad hydrogen content [wppm]	Clad oxide thickness [μm]	Axial total strain rate [s^{-1}]	Axial plastic strain to failure [%]	Equivalent hoop plastic failure strain (ϵ_f) [%]	Sample number	Comment
298	0.0	0	0	8.33E-5	35.0	7.95		Unirradiated
523	0.0	0	0	8.33E-5	38.0	8.63		Unirradiated
573	0.0	0	0	8.33E-5	44.0	9.99		Unirradiated
616	0.0	0	0	8.33E-5	46.0	10.4		Unirradiated
673	0.0	0	0	8.33E-5	49.0	11.1		Unirradiated
298	0.06	0	0	8.33E-5	15.6	0.79	ZS	Irradiated
298	0.09	0	0	8.33E-5	10.1	2.29	ZS	Irradiated
298	0.11	0	0	8.33E-5	8.0	1.82	ZS	Irradiated
298	0.14	0	0	8.33E-5	12.6	2.86	ZS	Irradiated
298	0.26	0	0	8.33E-5	8.6	1.95	ZS	Irradiated
298	1.18	18	7	8.33E-5	5.8	1.32	NK	Irradiated
298	2.90	40	16	8.33E-5	6.7	1.52	NK	Irradiated
298	3.10	43	17	8.33E-5	4.6	1.05	NK	Irradiated
573	0.08	0	0	8.33E-5	16.3	3.70	ZS	Irradiated
573	2.8	39	16	8.33E-5	5.3	1.20	NK	Irradiated
573	3.4	47	19	8.33E-5	3.0	0.68	NK	Irradiated
616	0.06	0	0	8.33E-5	21.7	4.93	ZS	Irradiated
616	0.08	0	0	8.33E-5	16.6	3.77	ZS	Irradiated
616	0.15	0	0	8.33E-5	4.2	0.95	ZS	Irradiated
616	0.16	0	0	8.33E-5	4.0	0.91	ZS	Irradiated
616	0.27	0	0	8.33E-5	4.8	1.09	ZS	Irradiated
616	1.21	17	7	8.33E-5	4.0	0.91	NK	Irradiated
623	2.9	40	16	8.33E-5	16.2	3.68	NK	Irradiated
623	3.6	50	20	8.33E-5	9.5	2.16	NK	Irradiated
623	0.2	0	0	8.33E-5	26.9	6.11	ZS	Irradiated
673	2.4	33	13	8.33E-5	20.3	4.61	NK	Irradiated
673	2.5	35	14	8.33E-5	18.8	4.27	NK	Irradiated

Table B.1: Sample conditions and measured axial plastic strain to failure for the NFD axial tension tests (Yasuda et al., 1987).

Test temperature [K]	Clad hydrogen content [wppm]	Hoop total strain rate [s ⁻¹]	Hoop plastic strain to failure [%]	Equivalent hoop plastic failure strain (ϵ_f) [%]	Sample number
563	< 15	2.00E-4	22.0	10.0	BO-1
563	< 15	2.00E-4	19.0	8.66	BO-2
563	< 15	2.00E-4	23.0	10.5	BO-3
563	< 15	2.00E-4	25.0	11.4	G3
563	< 15	2.00E-4	22.0	10.0	G4
563	< 15	2.00E-4	27.0	12.3	H3

Table B.2: Sample conditions and measured hoop plastic strain to failure for the Studsvik burst tests on un-irradiated samples. Data compiled from (Pettersson & Hellstrand, 1978) and (Pettersson et al., 1979).

B.2 Zircaloy-4 clad material

B.2.1 Dataset B

A series of burst tests was performed on Zircaloy-4 cladding tubes as part of the Nuclear Fuel Industry Research Group Program III (NFIR-III). Data from these tests are confidential, but selected parts of the results have recently been presented to the public by Yagnik et al. (2004).

B.2.2 JAERI tests

Burst tests were performed on 20 un-irradiated hydrogen charged cladding tubes at the Japan Atomic Energy Research Institute (JAERI) (Fuketa et al., 2000). The material under study was low tin (1.3wt%Sn) Zircaloy-4 cladding, which is commonly used in Japanese PWRs. The samples were hydrogen charged in a mixture of hydrogen and argon gas at about 600 K. A uniform hydrogen distribution was introduced in 12 of the samples, whereas the remaining samples were given pronounced hydride rims, 50-170 μm thick, at the clad tube outer surface.

Most of the burst tests were carried out at room temperature, but 5 of the samples with hydride rim were tested at 620 K. The strain rate ranged from 1.7×10^{-4} to $2.6 \times 10^{-1} \text{ s}^{-1}$. These strain rates are estimated from the rate of internal pressure increase under the tests, assuming elastic behaviour of the clad tube. In the plastic regime, the true strain rate is probably significantly higher. The test conditions and results for all samples are given in table B.3.

Test temperature [K]	Clad hydrogen content [wppm]	Hoop total strain rate [s ⁻¹]	Hoop plastic strain to failure [%]	Equivalent hoop plastic failure strain (ϵ_f) [%]	Comment
298	8	1.74E-4	9.3	4.24	Uniform hydrogen
298	164	1.74E-4	9.0	4.10	Uniform hydrogen
298	8	1.74E-4	6.6	3.01	Uniform hydrogen
298	351	1.74E-4	3.7	1.40	Uniform hydrogen
298	277	1.74E-4	1.6	0.73	Uniform hydrogen
298	9	1.65E-1	8.3	3.78	Uniform hydrogen
298	10	1.65E-1	8.2	3.74	Uniform hydrogen
298	171	1.65E-1	5.9	2.69	Uniform hydrogen
298	146	1.65E-1	5.3	2.42	Uniform hydrogen
298	198	1.65E-1	5.1	2.33	Uniform hydrogen
298	311	1.65E-1	1.4	0.64	Uniform hydrogen
298	461	1.65E-1	1.2	0.55	Uniform hydrogen
298	521	1.74E-4	0.39	0.18	Hydride rim
298	302	2.61E-1	0.70	0.32	Hydride rim
298	304	2.61E-1	0.48	0.22	Hydride rim
620	251	1.74E-4	11.3	5.15	Hydride rim 50 μ m
620	507	1.74E-4	0.77	0.35	Hydride rim 140 μ m
620	458	1.74E-2	2.28	1.04	Hydride rim 140 μ m
620	605	1.74E-2	0.57	0.26	Hydride rim 155 μ m
620	1036	1.74E-2	1.07	0.49	Hydride rim 170 μ m

Table B.3: Sample conditions and measured hoop plastic strain to failure for the JAERI burst tests on un-irradiated samples (Fuketa et al., 2000).

B.2.3 Tests on Fort Calhoun (FC) clad tubes

Burst- and axial tension tests were performed on altogether 16 clad tube samples, 2 of which were un-irradiated and the rest irradiated in the Fort Calhoun (FC) pressurized water reactor (Garde, 1989). The irradiated samples were taken from fuel rods reaching 53 MWdkg⁻¹U⁻¹ in burnup. The clad material was standard Zircaloy-4.

Burst tests were performed on 10 irradiated samples, which were 200 mm long and subjected to a hoop strain rate of 6.8x10⁻⁵ s⁻¹. The temperature was 588 K in all tests, and the hoop plastic strain to failure was evaluated from the increase of clad perimeter at the axial region of maximum deformation. The fast ($E \geq 1$ MeV) neutron fluence ranged from 6.1x10²⁵ to 1.03x10²⁶ m⁻² in these samples.

Axial tension tests were performed on 4 irradiated and 2 un-irradiated clad tube samples of the same material as in the burst tests. The specimen length was 125 mm, and the gage section used for evaluation of total axial elongation was 50 mm long. The tensile tests were performed at temperatures from 298 to 673 K, and the fast neutron fluence for all irradiated samples was 1.04x10²⁶ m⁻². The axial strain rate was 4.2x10⁻⁴ s⁻¹.

The test conditions and results for burst- and axial tension tests are given in tables B.4 and B.5, respectively. The clad hydrogen concentrations are estimated average values, presented in the original work by Garde (1989).

Test temperature [K]	Fast fluence $\times 10^{25}$ [m ⁻²]	Clad hydrogen content [wppm]	Hoop strain rate [s ⁻¹]	Hoop strain to failure [%]	Equivalent hoop plastic failure strain (ϵ_f) [%]	Sample number
588	10.3	300	6.77E-5	2.70	1.23	KJD075
588	10.3	300	6.77E-5	1.20	0.55	KJD075
588	10.4	300	6.77E-5	4.20	1.92	KJE051
588	10.3	300	6.77E-5	1.50	0.68	KJE089
588	10.3	400	6.77E-5	2.15	0.98	KJE089
588	10.0	300	6.77E-5	4.05	1.85	KJD008
588	6.1	100	6.77E-5	6.9	3.15	KKM098
588	6.1	100	6.77E-5	5.6	2.55	KKM098
588	8.1	175	6.77E-5	4.5	2.05	KJE076
588	8.1	175	6.77E-5	4.7	2.14	KJE076

Table B.4: Sample conditions and measured hoop plastic strain to failure in burst tests on Fort Calhoun cladding (Garde, 1989).

Test temperature [K]	Fast fluence $\times 10^{25}$ [m ⁻²]	Clad hydrogen content [wppm]	Axial total strain rate [s ⁻¹]	Axial plastic strain to failure [%]	Equivalent hoop plastic failure strain (ϵ_f) [%]	Sample number
298	0.0	< 15	4.2e-4	25.0	5.68	Unirradiated
673	0.0	< 15	4.2e-4	32.0	7.26	Unirradiated
298	10.4	350	4.2e-4	1.1	0.25	KJE089
473	10.4	350	4.2e-4	5.2	1.18	KJD008
573	10.4	350	4.2e-4	9.1	2.07	KJD015
673	10.4	350	4.2e-4	6.2	1.41	KJE051

Table B.5: Sample conditions and measured axial plastic strain to failure in axial tension tests on Fort Calhoun cladding (Garde, 1989).

B.2.4 Tests on ANO-2 and CC-1 clad tubes

Burst- and axial tension tests were performed on 42 clad tube samples, which were irradiated in the Arkansas Nuclear One – Unit 2 (ANO-2) and Calvert Cliffs – Unit 1 (CC-1) pressurized water reactors (Garde et al., 1996). The samples were taken from rods reaching 58 MWdkg⁻¹U⁻¹ in ANO-2 and 68 MWdkg⁻¹U⁻¹ in CC-1, respectively. In addition, 6 ring tensile tests were performed on the same material, but these tests are not considered here. The tested clad material was standard Zircaloy-4.

Burst tests were performed on 17 samples, which were 200 mm long and subjected to a hoop strain rate of 6.8x10⁻⁵ s⁻¹. The temperature was 588 K in all tests, and the hoop plastic strain to failure was evaluated from the increase of clad perimeter at the axial region of maximum deformation. The fast ($E \geq 1\text{MeV}$) neutron fluence was 1.1-1.2x10²⁶ m⁻² in these samples.

Axial tension tests were performed on 25 clad tube samples of the same material as in the burst tests. The specimen length was 127 mm, and the gage section used for evaluation of total axial elongation was 76 mm long. The tensile tests were performed at temperatures from 313 to 673 K, and the fast neutron fluence was 1.1-1.2x10²⁶ m⁻² also for these samples. The axial strain rate was 2.8x10⁻⁴ s⁻¹.

The test conditions and results for burst- and axial tension tests are given in tables B.6 and B.7, respectively. The presented clad hydrogen content is for the majority of the samples estimated from measured oxide layer thickness; see Garde et al. (1996).

Test temperature [K]	Fast fluence x10 ²⁵ [m ⁻²]	Clad hydrogen content [wppm]	Clad oxide thickness [μm]	Hoop total strain rate [s ⁻¹]	Hoop plastic strain to failure [%]	Equivalent hoop plastic failure strain (ε _p) [%]	Sample number	Comment
588	11.0	162	24	6.77E-5	2.28	1.04	7	ANO-2
588	11.0	178	26	6.77E-5	2.08	0.95	8	ANO-2
588	11.0	217	31	6.77E-5	2.28	1.04	9	ANO-2
588	11.0	233	33	6.77E-5	1.64	0.75	10	ANO-2
588	11.0	233	33	6.77E-5	2.58	1.18	11	ANO-2
588	11.0	273	38	6.77E-5	2.06	0.94	7	ANO-2
588	11.0	289	40	6.77E-5	1.73	0.79	10	ANO-2
588	11.0	320	44	6.77E-5	1.47	0.67	8	ANO-2
588	11.0	336	46	6.77E-5	2.45	1.12	9	ANO-2
588	12.0	207	36	6.77E-5	2.69	1.23	1	CC-1
588	11.7	229	40	6.77E-5	6.47	2.95	2	CC-1
588	11.7	322	53	6.77E-5	3.30	1.50	3	CC-1
588	11.6	387	62	6.77E-5	5.04	2.30	4	CC-1
588	12.3	423	67	6.77E-5	2.41	1.10	1	CC-1
588	12.2	573	88	6.77E-5	2.22	1.01	1	CC-1
588	11.7	595	91	6.77E-5	3.16	1.44	1	CC-1
588	12.1	731	110	6.77E-5	0.58	0.26	5	CC-1 Spalled

Table B.6: Sample conditions and measured hoop plastic strain to failure in burst tests on ANO-2 and CC-1 cladding (Garde et al., 1996).

Test temperature [K]	Fast fluence $\times 10^{25}$ [m ²]	Clad hydrogen content [wppm]	Clad oxide thickness [μm]	Axial total strain rate [s ⁻¹]	Axial plastic strain to failure [%]	Equivalent hoop plastic failure strain (ϵ_f) [%]	Sample number	Comment
313	11.7	150	29	2.8e-4	8.39	1.90	CC-1 2	
313	11.5	279	47	2.8e-4	8.61	1.95	CC-1 3	
313	11.7	430	68	2.8e-4	1.08	0.25	CC-1 3	
573	11.4	171	32	2.8e-4	4.74	1.08	CC-1 3	
573	11.5	279	47	2.8e-4	7.89	1.79	CC-1 3	
573	11.7	487	76	2.8e-4	7.89	1.79	CC-1 1	
573	11.5	459	72	2.8e-4	6.82	1.55	CC-1 3	
573	11.7	645	98	2.8e-4	1.74	0.39	CC-1 5	Spalled
573	12.1	674	102	2.8e-4	3.62	0.82	CC-1 5	Spalled
673	11.4	150	29	2.8e-4	16.0	3.63	CC-1 2	
673	11.7	293	49	2.8e-4	9.11	2.07	CC-1 3	
673	11.7	430	68	2.8e-4	4.55	1.03	CC-1 3	
313	11.5	130	20	2.8e-4	10.1	2.29	ANO-2 7	
313	11.5	217	31	2.8e-4	6.2	1.41	ANO-2 7	
313	11.5	281	39	2.8e-4	7.0	1.59	ANO-2 7	
313	11.5	289	40	2.8e-4	6.8	1.54	ANO-2 11	
313	11.5	320	44	2.8e-4	8.1	1.84	ANO-2 10	
573	11.5	305	42	2.8e-4	4.3	0.98	ANO-2 8	
573	11.5	313	43	2.8e-4	3.4	0.77	ANO-2 11	
573	11.5	352	48	2.8e-4	3.5	0.79	ANO-2 8	
673	11.5	170	25	2.8e-4	14.0	3.18	ANO-2 9	
673	11.5	233	33	2.8e-4	7.2	1.63	ANO-2 9	
673	11.5	305	42	2.8e-4	3.0	0.68	ANO-2 9	
673	11.5	344	47	2.8e-4	2.8	0.64	ANO-2 11	
673	11.5	360	49	2.8e-4	2.5	0.57	ANO-2 10	

Table B.7: Sample conditions and measured axial plastic strain to failure in axial tension tests on ANO-2 and CC-1 cladding (Garde et al., 1996).

Appendix C: Clad failure criteria based on strain energy density

Two rather similar criteria for predicting clad tube failure under RIA are available in open literature. The first was put forth by ANATECH Corporation as early as in 1995, (Rashid et al., 1995) and it has later been revised (Rashid et al., 2000). The second criterion is of later date, and follows very closely the approach laid out by Rashid and co-workers. It has been suggested by CIEMAT, under the sponsorship of the Spanish nuclear regulatory authority CSN, (del Barrio & Herranz, 2002).

In both criteria, the clad ductility is measured in terms of strain energy density (SED). Clad failure is assumed to take place when the strain energy density in the material reaches and exceeds a critical strain energy density (CSED), which is determined from mechanical property tests through

$$\text{CSED} = \int_0^{\hat{\varepsilon}_f} \sigma_{ij}(\hat{\varepsilon}') d\varepsilon'_{ij}, \quad (\text{C.1})$$

where σ_{ij} and ε_{ij} are components of the stress and strain tensors, respectively, and $\hat{\varepsilon}_f$ denotes the strain tensor at failure. Hence, the integral in eq. (C.1) is evaluated over the entire stress-strain path taken in the test, as illustrated in section C.1 below.

In the failure criteria by ANATECH and CIEMAT, correlations for the CSED are determined from results of mechanical property tests on Zircaloy-4 cladding. Hence, the criteria are intended for predictive analyses of RIA in PWRs. The main difference between the two criteria is found in the supporting experimental databases. The criterion by ANATECH is based on roughly 120 material property tests, whereas the criterion by CIEMAT is supported by only 28 tests.

The CSED has sometimes been claimed to be a material property, which is dependent on temperature, fast neutron fluence and the material's hydrogen content, but independent of stress state and loading path. However, a closer look on experimental data from burst tests and axial tensile tests on cladding tubes clearly reveals that the CSED is strongly dependent on stress state, i.e. on the stress biaxiality. Hence, just like the hoop plastic strain at failure, the CSED is not a true material property. The CSED applied in clad tube failure criteria should therefore be determined from tests performed under the same biaxial stress state as expected under RIA. In reality, the criteria by ANATECH and CIEMAT have been determined from clad tube burst tests, ring tension tests and uniaxial tensile tests, whereby the non-prototypical stress state has been compensated for in much the same way as in section 5.2.1 of the present report.

In the work presented by Rashid et al. (2000), it is claimed that failure of a clad tube with a flaw or a surface defect can be predicted by calculating the average strain energy density in an axial cross-section of the tube, without explicitly modelling the flaw or performing fracture mechanics analysis.

From fundamental principles of fracture mechanics, it is clear that this statement is true only if we assume a fixed size of the defect and a specific constitutive relation for the material. Hence, the average strain energy density in the clad tube is *not* a fracture mechanics parameter, and it does definitely not belong to the category of local crack tip properties, such as the stress intensity factor or the J -integral, which are used in failure criteria based on fracture mechanics (Anderson, 1995).

A major difficulty in determining the CSED under multiaxial loading is that the relationship between stress and strain in eq. (C.1) must be accurately known. This is not always the case: in particular for highly irradiated and hydrided material, the constitutive relation is rarely well known. Both ANATECH and CIEMAT have applied the widely used constitutive relation from MATPRO in their evaluations of CSED from experimental data (Hagrman et al., 1981). By use of this relation, it is possible to transform the CSED to plastic hoop strain at failure and *vice versa*. This is further described below.

C.1 Converting CSED to hoop failure strain

Consider an elasto-plastic material with a relation between stress and strain as shown in figure C.1. Here, σ_y is the yield stress, ϵ_e is the elastic strain limit, and ϵ_{te} is the total (plastic) elongation of the material. In the plastic region, the relation between stress and strain is assumed to follow the MATPRO model,

$$\sigma(\epsilon, \mathbb{E}) = K \left(\frac{\mathbb{E}}{\mathbb{E}_0} \right)^m \epsilon^n. \quad (C.2)$$

Here, K , \mathbb{E}_0 , m , and n are parameters in the constitutive model. They are fully defined in section C.3.

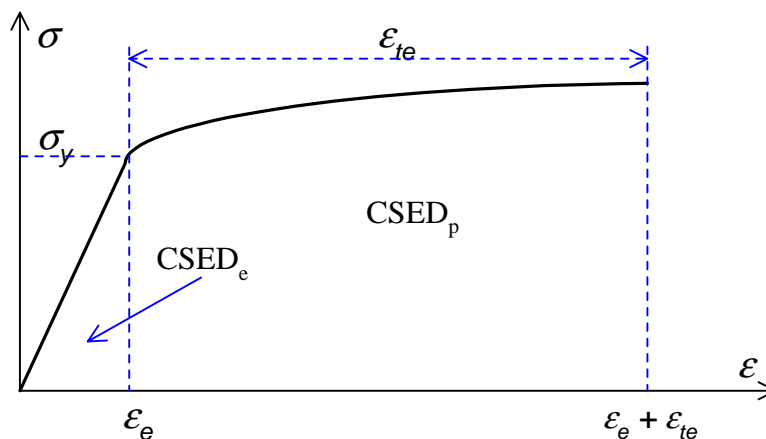


Figure C.1: The total area under the uniaxial stress-strain curve corresponds to the critical strain energy density. It can be partitioned into elastic and plastic parts, as shown by the figure.

The stress-strain relation shown in figure C.1 and partly given by eq. (C.2) represents the material behaviour under uniaxial tension. Under multiaxial loading, the stresses and strains should be interpreted as *effective* properties, i.e. σ corresponds under multiaxial loading to the effective stress, and ε corresponds to the effective strain.

Aiming at deriving a relation between CSED and the total elongation ε_{te} , we start by partitioning the CSED into elastic and plastic parts. Thus, we have

$$\text{CSED} = \text{CSED}_e + \text{CSED}_p, \quad (\text{C.3})$$

where the elastic part can be written (see figure C.1)

$$\text{CSED}_e = \frac{\sigma_y \varepsilon_e}{2} = \left[\varepsilon_e = \frac{\sigma_y}{E_Y} \right] = \frac{\sigma_y^2}{2E_Y}. \quad (\text{C.4})$$

Here, E_Y is Young's modulus. It is correlated to temperature and fast neutron fluence through a model defined in section C.3. The plastic part of the critical strain energy density follows from the MATPRO constitutive relation in eq. (C.2)

$$\text{CSED}_p = \int_{\varepsilon_e}^{\varepsilon_e + \varepsilon_{te}} \sigma(\varepsilon, \dot{\varepsilon}) d\varepsilon = \int_{\varepsilon_e}^{\varepsilon_e + \varepsilon_{te}} K \left(\frac{\dot{\varepsilon}}{\dot{\varepsilon}_o} \right)^m \varepsilon^n d\varepsilon. \quad (\text{C.5})$$

By evaluating the integral in eq. (C.5), assuming constant material properties under the loading history, and making use of eqs. (C.3) and (C.4), we find the following relation between total elongation and critical strain energy density

$$\varepsilon_{te} = \left[\left(\frac{\sigma_y}{E_Y} \right)^{n+1} + \frac{(n+1) \left(\text{CSED} - \frac{\sigma_y^2}{2E_Y} \right)}{\sigma_y^{1-n} E_Y^n} \right]^{\frac{1}{1+n}} - \frac{\sigma_y}{E_Y}. \quad (\text{C.6})$$

Moreover, since $\sigma(\varepsilon_e) = \sigma_y = E_Y \varepsilon_e$, we find the yield stress from eq. (C.2)

$$\sigma_y = \left[\frac{K}{E_Y^n} \left(\frac{\dot{\varepsilon}}{\dot{\varepsilon}_o} \right)^m \right]^{\frac{1}{1-n}}. \quad (\text{C.7})$$

Hence, by using the MATPRO material model in section C.3 for the material properties, eqs. (C.6) and (C.7) can be used to transfer critical strain energy density to total (plastic) elongation and *vice versa*. However, we recall that eqs. (C.6) and (C.7) are defined for uniaxial loading conditions, and they can therefore be applied to a biaxially loaded cladding tube only if the strain and strain rate are substituted with their effective values.

By applying the theory of isotropic plasticity to a biaxially loaded tube ($\sigma_{zz}/\sigma_{\theta\theta} = 1$), we find that the effective plastic strain, $\tilde{\varepsilon}^P$, and effective strain rate, $\dot{\varepsilon}$, are related to their counterparts in the hoop direction through

$$\tilde{\varepsilon}^P = 2\varepsilon_{\theta\theta}^P \quad (\text{C.8})$$

and

$$\dot{\varepsilon} = 2\dot{\varepsilon}_{\theta\theta}. \quad (\text{C.9})$$

Hence, for a biaxially loaded tube, the hoop plastic failure strain ε_f is calculated from the critical strain energy density through

$$\varepsilon_f = \frac{1}{2} \left[\left(\frac{\sigma_y}{E_Y} \right)^{n+1} + \frac{(n+1) \left(\text{CSED} - \frac{\sigma_y^2}{2E_Y} \right)}{\sigma_y^{1-n} E_Y^n} \right]^{\frac{1}{1+n}} - \frac{\sigma_y}{2E_Y}, \quad (\text{C.10})$$

where the yield stress is defined by

$$\sigma_y = \left[\frac{K}{E_Y^n} \left(\frac{2\dot{\varepsilon}_{\theta\theta}}{\dot{\varepsilon}_o} \right)^m \right]^{\frac{1}{1-n}}. \quad (\text{C.11})$$

These are the relations used for comparing SED-based failure criteria with the strain-based failure criterion in section 6.2. The MATPRO correlations used for material properties are defined in section C.3.

C.2 CSED correlations

C.2.1 CSED correlation by EPRI/ANATECH

The correlation for critical strain energy density (CSED) proposed by Rashid et al. (2000) is

$$\text{CSED} = C_1 e^{-C_2 x} \text{ [MPa]}, \quad (\text{C.12})$$

where x is the ratio of the clad outer oxide layer thickness to the clad wall thickness. The coefficients C_1 and C_2 are defined for two different temperature intervals, which are spanned by the experimental database upon which the correlation rests.

For $295 < T < 423$ K:

$$C_1 = 15.6, \quad C_2 = 7.17. \quad (\text{C.13})$$

For $553 < T < 673$ K:

$$C_1 = 41.5, \quad C_2 = 6.62. \quad (\text{C.14})$$

Except for the temperatures, the range of application for this correlation is not defined. It should be noticed that the correlation presented here is significantly more conservative than the one originally proposed in 1995 (Rashid et al., 1995). In the original correlation, the CSED is more than twice as large as in the current correlation. The background to this drastic revision is not known.

C.2.2 CSED correlation by CSN/CIEMAT

The correlation for critical strain energy density (CSED) proposed by del Barrio & Herranz (2002) is

$$\text{CSED} = 43.77 - 203.61 x - 1.26 \dot{\epsilon} + 1.94 \cdot 10^{-2} T \text{ [MPa]}, \quad (\text{C.15})$$

where x is the ratio of the clad outer oxide layer thickness to the clad wall thickness, T is the temperature in Kelvin and $\dot{\epsilon}$ is the strain rate in s^{-1} . It is not clear from their publication, if this strain rate is referred to the clad hoop direction, or if it is the effective value. Here, it is assumed to be the strain rate in the clad hoop direction.

The correlation in eq. (C.15) is derived from 28 tests on small-size ring samples of irradiated Zircaloy-4 cladding, performed within the PROMETRA program (Balourdet et al., 1999). The correlation has a rather limited range of application:

- Clad oxide layer thickness: 15 to 130 μm .
- Clad temperature: 553 to 753 K.
- Clad strain rate: 0.01 to 5 s^{-1} .

C.3 MATPRO constitutive relation

The MATPRO library of models for light water reactor fuel material properties is widely used, and it has been revised at several occasions. The models presented here are taken from MATPRO Version 11, revision 2 (Hagrman et al., 1981).

The strain rate dependence of the constitutive relation in eq. (C.2) is defined by two constants

$$\dot{\epsilon}_o = 1 \cdot 10^{-3} \text{ [s}^{-1}\text{]}, \quad (\text{C.16})$$

$$m = 0.02. \quad (\text{C.17})$$

The strain hardening exponent n is dependent on temperature,

$$n = -9.49 \cdot 10^{-2} + T \left[1.165 \cdot 10^{-3} + T \left(9.588 \cdot 10^{-10} T - 1.992 \cdot 10^{-6} \right) \right]. \quad (\text{C.18})$$

The strength coefficient K is dependent on temperature and fast neutron fluence ϕ ,

$$K = K_T + K_\phi , \quad (\text{C.19})$$

where the temperature dependent part is

$$K_T = 1.17628 \cdot 10^9 + T \left[4.54859 \cdot 10^5 + T \left(1.72752 T - 3.28185 \cdot 10^3 \right) \right] \quad (\text{C.20})$$

and the irradiation dependent part is

$$K_\phi = 5.54 \cdot 10^{-18} \phi . \quad (\text{C.21})$$

Here, K , K_T and K_ϕ are in Pa and ϕ is the fast ($E \geq 1\text{MeV}$) neutron fluence per m^2 . Finally, Young's modulus is calculated through

$$E_Y = \frac{1.088 \cdot 10^{11} - 5.475 \cdot 10^7 T}{0.88 + 0.12 e^{-1 \cdot 10^{-25} \phi}} , \quad (\text{C.22})$$

where E_Y is in Pa and ϕ is the fast ($E \geq 1\text{MeV}$) neutron fluence per m^2 . Throughout eqs. (C.18) to (C.22), the temperature T is in Kelvin.

www.ski.se

STATENS KÄRNKRAFTINSPEKTION
Swedish Nuclear Power Inspectorate

POST/POSTAL ADDRESS SE-106 58 Stockholm

BESÖK/OFFICE Klarabergsviadukten 90

TELEFON/TELEPHONE +46 (0)8 698 84 00

TELEFAX +46 (0)8 661 90 86

E-POST/E-MAIL ski@ski.se

WEBBPLATS/WEB SITE www.ski.se